

The Pennsylvania State University
The Graduate School
Department of Aerospace Engineering

ACOUSTICS OF DUCTED ROTORS

A Thesis in

Aerospace Engineering

by

Jacob Zentichko

Submitted in Partial Fulfillment
of the Requirements
for the Degree of

Master of Science

December 2010

The thesis of Jacob Zentichko was reviewed and approved* by the following:

Kenneth S. Brentner
Professor of Aerospace Engineering
Thesis Advisor

Dennis K. McLaughlin
Professor of Aerospace Engineering

George A. Lesieutre
Professor of Aerospace Engineering
Head of the Department of Aerospace Engineering

*Signatures are on file in the Graduate School

ABSTRACT

In recent years, ducted rotors have become increasingly important to rotor craft for performance and safety reasons. Although much is understood about the thrust performance of a ducted rotor, the acoustics is less well understood. This dissertation describes the tools and techniques to lay the ground work for an accurate acoustics analysis. Some theoretical work will be presented using the NASA Fast Scattering Code (FSC) for later comparison to noise data obtained from Computational Fluid Dynamics (CFD). The CFD work was be done using the commercial software package Fluent. Both an open rotor and a ducted rotor will be simulated for the purpose of comparison with both momentum theory and acoustics. A converter was written to link Fluent with the rotor noise prediction code PSU-WOPWOP. PSU-WOPWOP uses the Ffowcs Williams-Hawkings approach to calculate the sound field. The duct and the rotor sound fields may be calculated separately, which provides an understanding of the impact of both noise sources. Ultimately, the goal is to compare the ducted rotor acoustics to the open rotor acoustics to analyze the differences and to understand sources of those differences.

TABLE OF CONTENTS

ABSTRACT.....	iii
LIST OF FIGURES	vi
LIST OF TABLES	x
NOMENCLATURE LIST	xi
ACKNOWLEDGEMENTS.....	xiii
 Chapter 1 Introduction	 1
1.1 Background.....	1
1.2 Objectives	2
1.3 Momentum Theory of Ducted Rotors.....	3
1.4 Overview of Acoustics Problem.....	10
1.5 Ffowcs Williams-Hawkings Approach.....	14
1.6 Equivalent Source Method	16
1.7 Approach to Objectives.....	19
 Chapter 2 Aerodynamics of Ducted Tail Rotors.....	 20
2.1 Two Dimensional Axisymmetric CFD	20
2.2 Three Dimensional CFD.....	26
2.2.1 Ducted Rotor	28
2.2.2 Open Rotor.....	42

2.3 Comparison of Loading	46
2.4 Comparison with Momentum Theory	49
Chapter 3 Acoustics	52
3.1 FSC Predictions	53
3.2 Ffowcs Williams-Hawkings Approach.....	58
3.2.1 Overall Sound Pressure Level.....	59
3.2.2 Sound Harmonics.....	64
Chapter 4 Conclusions	70
4.1 Summary of Research.....	70
4.2 Summary and Conclusions of Aerodynamics.....	70
4.3 Summary and Conclusions of Acoustics	72
BIBLIOGRAPHY	75
Appendix A Aerodynamic Setup in Fluent.....	79
Appendix B Converter	90

LIST OF FIGURES

Figure 1.1 : Control Volumes of Ducted and Unducted Rotors.	3
Figure 1.2 : Power Consumption as a Function of Wake Expansion.	8
Figure 1.3 : Trend of Thrust Increase as a Function of Wake Expansion.	9
Figure 1.4 : Total Thrust Increase as a Function of Wake Expansion.....	9
Figure 1.5 : Directivity of Sound Types.	11
Figure 1.6 : Scattering Example.....	12
Figure 1.7 : Open Rotor Example.....	12
Figure 1.8 : Fenestron Ducted Rotor.....	13
Figure 1.9 : Turbofan Engine.....	13
Figure 1.10 : ESM Theoretical Formulation.....	17
Figure 1.11 : ESM Surface.....	19
Figure 2.1 : 2D Domain with Boundary Conditions.....	21
Figure 2.2 : 2D Unducted Rotor Streamlines.....	22
Figure 2.3 : 2D Zero Degree Diffuser Angle Duct Case.	23
Figure 2.4 : 2D Four Degree Diffuser Angle Duct Case	24
Figure 2.5 : 2D Results Compared to Theory.....	24
Figure 2.6 : Area Where Flow Separation is Possible.	25
Figure 2.7 : Ducted Rotor Used for Experimenting and Simulations.....	26

Figure 2.8: Simplified Computational Model.....	27
Figure 2.9: Duct and Rotor Pressure (p' , Pa).....	28
Figure 2.10: Ducted Rotor Pressure (p' , Pa).....	29
Figure 2.11: Rotor Blade Influence on Duct Wall Pressure (p' , Pa)	30
Figure 2.12: Inside Duct Wall Pressure Features (p' , Pa).....	31
Figure 2.13: Pressure on the Duct Wall in the Plane of the Rotor Blade (p' , Pa) distance is the circumferential distance around the duct wall.	32
Figure 2.14: Early Ducted Rotor Velocity (v , m/s)	33
Figure 2.15: Early Ducted Rotor Wake Profile	33
Figure 2.16: Ducted Rotor Developed Velocity Contours (v , m/s).....	34
Figure 2.17: Ducted Rotor Developed Wake Profile.....	35
Figure 2.18: Separated Duct Flow.	36
Figure 2.19: Duct Inlet and Tip Vortex.	37
Figure 2.20: Duct Outlet and Recirculation.....	38
Figure 2.21: Wake Cutting Plane.....	39
Figure 2.22: Ducted Rotor Far Wake (v , m/s)	40
Figure 2.23: Ducted Rotor Near Wake (v , m/s).....	40
Figure 2.24a: Thrust of Rotor and Duct (Time Step 0-6000).....	41
Figure 2.24b: Thrust of Rotor and Duct (Time Step 6000-12500).....	41
Figure 2.25: Open Rotor Pressure (p' , Pa).....	42

Figure 2.26: Open Rotor Wake Developed Wake Profile.	43
Figure 2.27: Open Rotor Far Wake (v , m/s).	44
Figure 2.28: Open Rotor Near Wake (v , m/s).	45
Figure 2.29: Open Rotor Thrust Over Time.	46
Figure 2.30a: Ducted Rotor Blade Pressure Distribution (p' , Pa).	47
Figure 2.30b: Open Rotor Blade Pressure Distribution (p' , Pa).	47
Figure 2.31: Spanwise Loading Comparison.	48
Figure 2.32: Pressure Along the Rotor Blade Tip (p' , Pa).	49
Figure 3.1: FSC Duct Wireframe.	53
Figure 3.2: Incident Sound Field from the Isolated Rotor.	54
Figure 3.3: Total Sound Field Using the FSC.	55
Figure 3.4: Effects of Duct Thickness on Noise Scattering.	56
Figure 3.5: Effect of Duct Length on Noise Scattering.	57
Figure 3.6: Difference in Sound Field Due to Duct Length Difference (OASPLdB)	58
Figure 3.7: OASPL Based on CFD Results.	59
Figure 3.8: OASPL Polar Plots.	60
Figure 3.9: Open Directivity vs Rotor Alone Directivity.	61
Figure 3.10: Total Directivity vs Rotor Alone Directivity.	62
Figure 3.11: FSC Rotor Placement.	63

Figure 3.12: CFD Rotor Placement.	63
Figure 3.13: Azimuthal Locations of Microphones.	64
Figure 3.14a: Experimental Directivity Results.	65
Figure 3.14b: Experimental Directivity Results.	65
Figure 3.15a: 1 st Harmonic	66
Figure 3.15b: 2 nd Harmonic.	66
Figure 3.15c: 3 rd Harmonic.	67
Figure 3.15d: 4 th Harmonic.	67
Figure 3.15e: 5 th Harmonic.	68
Figure 3.16: Frequency Spectrum Measure for Open and Ducted Rotor.	68
Figure A.1: Duct Geometry.	80
Figure A.2: Wireframe of Domain.	81
Figure A.3: Inner Region of Domain.	82
Figure A.4: Outer Region and Duct Area.	83
Figure A.5: Split Volume Window.	83
Figure A.6: Domain Mesh.	84
Figure A.7: Duct Area Mesh.	85
Figure A.8: Wall Meshing Options.	86
Figure A.9: Defining Grid Units.	87

Figure A.10: Mesh Distribution Along Rotor Blade Span.	87
Figure A.11: Hub Mesh.	88
Figure A.12: Leading Edge Mesh.	88
Figure A.13: Trailing Edge Mesh.	89
Figure A.14: Tip Mesh.	89

LIST OF TABLES

Table 2.1: Momentum Theory Parameters.	50
Table A.1: Rotor Parameters.	79
Table A.2: Mesh Details.	85

Nomenclature List

Momentum Theory

v_i	The induced velocity
w	Far-wake velocity
T	Total thrust
\dot{m}	Mass flow rate through the system

P Power consumed by the system

A_∞ Far-wake Area

A Area of the rotor

a_w Wake Contraction Parameter

ρ Flow density

p Pressure

Sub-Scripts

0 Far upstream

1 Just upstream of the rotor

2 Just downstream of the rotor

∞ Far downstream

Acoustics

p' Acoustic pressure

p'_T Thickness acoustic pressure

p'_L Loading acoustic pressure

FW-H Equation

U_n Related to the velocity $U_n = \frac{\rho}{\rho_0} (u_n - v_n) + v_n$

L_i Related to the loading $L_i = p_{ij}n_j + \rho u_i(u_n - v_n)$

r	Distance from the source to the receiver
M	Mach number of the source
M_r	Mach number of the source in the radiated direction
ESM	
v'	Acoustic Velocity
c_0	Local speed of sound
\vec{M}_0	Local Mach number vector
k_0	Local wave number w/c_0
i	Imaginary unit $\sqrt{-1}$
Z	Complex normal impedance
A	Acoustic admittance $1/Z$

ACKNOWLEDGEMENTS

I would like to take this time to acknowledge the many people that contributed to this work. Thank you to the Office of Naval Research for providing funding for this project.

Many of the CFD figures presented in this thesis were generated using FIELDVIEW, and I would like to thank Intelligent Light for providing the program.

I would also like to thank my advisor, Dr. Kenneth Brentner for the opportunity to take this project.

Thanks, also, to the experimental team under the advice of Dr. McLaughlin, especially to Leighton Myer who provided much of the data and test subject descriptions and was always willing to answer my questions about the testing.

I would also like to acknowledge the many great co-workers I have had the privilege of working with at the Penn State Rotorcraft Center of Excellence. One of the workers in specific I would like to acknowledge is Dr. Leonard Lopes for his help in programming as well as providing the blade-element code used in this research.

A very special thank you to a great co-worker, classmate, and friend James Erwin to whom I owe much of my graduate school success. Thank you for all the help with PSU-WOPWOP and showing me how to use the Fast Scattering Code and all of your assistance running those codes.

Chapter 1

Introduction

The tail rotor is a device of great importance to a single main rotor helicopter. The tail rotor has the important function of countering the main rotor's torque and providing yaw control. Yet the power required to power a tail rotor is considered lost power since it is not used to generate lift. This power can be a significant portion of the total power needed to operate a helicopter (as much as 10%) [1].

One method used to achieve the goal of reducing the power required by the tail rotor is to encase the rotor in a duct [1, 2]. Shrouding a rotor is also intended to improve safety eliminating the chance of the tail rotor striking a solid object or personnel on the ground. Since this type of tail rotor configuration is favorable in urban environments, the noise produced is of great importance [3].

Because civil helicopters must meet noise certification to enter service, the noise produced is of concern. Likewise, military rotorcraft designers are concerned with noise levels to limit the likelihood of acoustic detection. The noise itself can be difficult to predict for several reasons. The first reason is that the duct provides some noise shielding in the plane of the rotor but also scatters the noise of the rotor [4]. Predicting the scattering is a difficult problem because current duct acoustics theory is only applicable to longer ducts, in which some of the frequencies are cut off and do not propagate. Typical ducted tail rotors may only be less than one rotor radii long and the wavelength associated with the blade passage frequency may be on the same order as the duct length [5]. The second reason that ducted tail rotor noise is more difficult to predict is due to the increased complexity of the flow in the duct itself. Ducts can have guide veins, mounting struts, or other aerodynamic features that will change the loading on the rotor and therefore the noise it produces. A typical open tail rotor will only have the airframe of the aircraft obstructing the flow. Ducted rotors are important in other applications, such

as uninhabited air vehicles (UAVs), and Compound Rotorcraft, etc. Therefore the study of ducted rotor noise is quite important.

1.2 Objectives

The objective of this research is to gain an understanding of the performance improvements and acoustic changes through the application of momentum theory, CFD, and acoustic predictions. This will be done in multiple steps.

First, some basic 2D axisymmetric CFD work has been conducted to compare with momentum theory and gain an understanding of the duct aerodynamics. This provides a basic overview of thrust and aerodynamic changes (such as how the wake forms) when a duct is added to a rotor. These simulations are expanded to 3 dimensions for a full calculation of a ducted tail rotor flow field. The three dimensional calculations include ducted and unducted cases for comparison purposes. The goal of the 3D cases is to explore in more detail the changes due to the duct. Overall thrust, spanwise thrust distribution, and other aerodynamic changes are analyzed.

Understanding the acoustics changes is also of great importance to this research. There are several approaches to achieve this goal. These approaches differ by computational speed and accuracy. To understand the acoustics of the rotor, a blade element code is used for fast computation while a CFD simulation was conducted to gain a more precise sound field. To explore the impact the duct had on the sound field, there were also two methods. The Fast Scattering Code (FSC), developed by NASA, is a quick means to calculate the impact of the duct. PSU-WOPWOP is used to calculate the impact of the duct based from the CFD.

The final objective is to model the complex features inside of a duct, such as vanes and struts. This modeling will be approximate for the sake of computational speed. Ultimately, obtaining an accurate model for obstructions in a ducted tail rotor is the purpose and goal of the research.

1.3 Momentum Theory of Ducted Rotors

The fundamental theory used to analyze both ducted and unducted rotors assumes an incompressible, uniform, inviscid, steady, and quasi-one dimensional flow. Control volumes for both the unducted and ducted cases are illustrated below (figure 1.1).

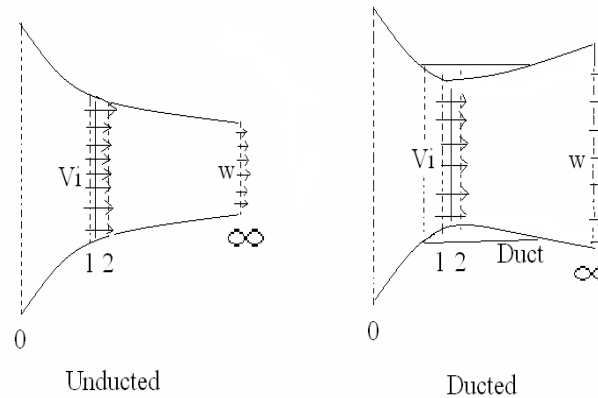


Figure 1.1: Control Volumes of Ducted and Unducted Rotors

Note that the ducted fan wake is shown to be expanded while the unducted rotor's wake contracts. This will be justified later.

Incoming flow is represented by station 0. This is placed sufficiently far enough upstream such that the pressure is equal to the ambient condition and the velocity of the flow is essentially zero (for a hover case). Station 1 and 2 are just upstream and downstream of the rotor disk, respectively. The station labeled " ∞ " represents a position far downstream from the rotor disk, such that the wake is fully contracted (unducted) or expanded (ducted). Also, the static pressure at " ∞ " is assumed to return to the ambient state. The top and bottom edges of the control volume are along streamtubes so there is no mass flow across this surface.

With the control volume boundary conditions set, conservation of mass, momentum, and energy may be applied. For an unducted rotor case, it is shown that the momentum equation reduces to;

$$T = \dot{m}w \quad (1.1)$$

here T is the total thrust, \dot{m} is the mass flow rate through the system, and w is the far-wake velocity.

Conservation of energy yields

$$P = T v_i = \frac{1}{2} \dot{m} w^2 \quad (1.2)$$

where P is the power consumed by the system, and v_i is the induced velocity. By combining these two expressions and applying continuity, the following relationships can be obtained.

$$\frac{v_i}{w} = \frac{1}{2} \quad (1.3)$$

$$\frac{A_\infty}{A} = \frac{1}{2} \quad (1.4)$$

These relationships show that for an unducted rotor (where the wake is free to contract) the wake contracts to an area half the size of the rotor. The velocity also accelerates to twice the velocity induced at the rotor [1, 2]. This is an important result which will be used for comparison with later results.

For the ducted case, the wake is not free to contract due to the presence of the duct so the approach to the problem is somewhat different but the same governing equations apply. The primary difference in the analysis of the ducted rotor is that the

total thrust can be expressed as the sum of the duct thrust and the rotor thrust. The ducted rotor momentum equations are developed slightly differently.

$$T = T_{Rotor} + T_{Duct} = \dot{m}w \quad (1.5)$$

The contribution of the thrust due to the rotor can be calculated knowing that the thrust per unit area is equal to the pressure difference above and below the rotor and by applying Bernoulli's equation between states 0 to 1, and 2 to ∞ .

$$p_0 = p_1 + \frac{1}{2}\rho v_i^2$$

$$p_2 + \frac{1}{2}\rho v_i^2 = \frac{1}{2}\rho w^2 + p_\infty \quad (1.6)$$

$$T_{Rotor} = (p_1 - p_2)A = \frac{1}{2}\rho w^2 A$$

where A is the area of the rotor disk. The duct contribution to the thrust can be obtained by using equations 1.5, 1.6.

$$T_{Duct} = \rho A w^2 \left(\frac{v_i}{w} - \frac{1}{2} \right) \quad (1.7)$$

Note that this relationship is not in the references but can be shown by subtracting the rotor thrust from the total thrust. As shown in equation 1.7, the contribution to the total thrust from the duct depends on the ratio of the far wake velocity to the induced velocity. It can be shown for an incompressible flow that;

$$\frac{A_{\infty}}{A} = \frac{v_i}{w} \quad (1.8)$$

This ratio of the far wake area to the rotor area is defined as the wake contraction parameter and denoted by “ a_w ”.

$$a_w = \frac{A_{\infty}}{A} \quad (1.9)$$

Note that it was shown in equation 1.4 that the ratio of the far wake area to the rotor area is equal to 0.5 for an open rotor. This correctly shows that for a free rotor, the duct contribution to the thrust is zero. For future results, an a_w value of 0.5 can represent an unducted rotor. Using the wake contraction parameter, equation 1.7 can be rewritten as;

$$T_{Duct} = \rho A w^2 \left(a_w - \frac{1}{2} \right) \quad (1.10)$$

One other point of interest is that for an a_w value of 1;

$$T_{Rotor} = T_{Duct} = \frac{1}{2} \rho A w^2 \quad (1.11)$$

The wake contraction parameter acts as a correction factor so many of the relationships for a ducted rotor look very similar to that of an unducted rotor. The induced velocity is shown to be:

$$v_i = \sqrt{\frac{T a_w}{A \rho}} \quad (1.12)$$

The relationship for power is derived as followed;

$$P_i = T_{rotor} v_i \quad (1.13)$$

or

$$P = \frac{T_{total}^{3/2}}{\sqrt{4 a_w \rho A}} \quad (1.14)$$

Taking the ratio of the induced power for an unducted to a ducted rotor assuming that the total thrust remains constant;

$$\frac{P_{unducted}}{P_{ducted}} = \frac{1}{\sqrt{2 a_w}} \quad (1.15)$$

From equation 1.15, it is shown that as the wake contraction parameter increases, the induced power decreases. The decreased power is due to the contribution of duct thrust to the total thrust. The following plots illustrate how the performance of a rotor may be increased.

Figure 1.2 shows that for the same total thrust, the power required to hover decreases compared to an unducted rotor [6]. Ducted rotors with large values of a_w ($a_w > 1.2$) may produce the same total thrust at only a fraction of the power. There are physical limitations to how large a_w may be that will be shown later. Examples of ducts with different a_w values will be presented in chapter 2.

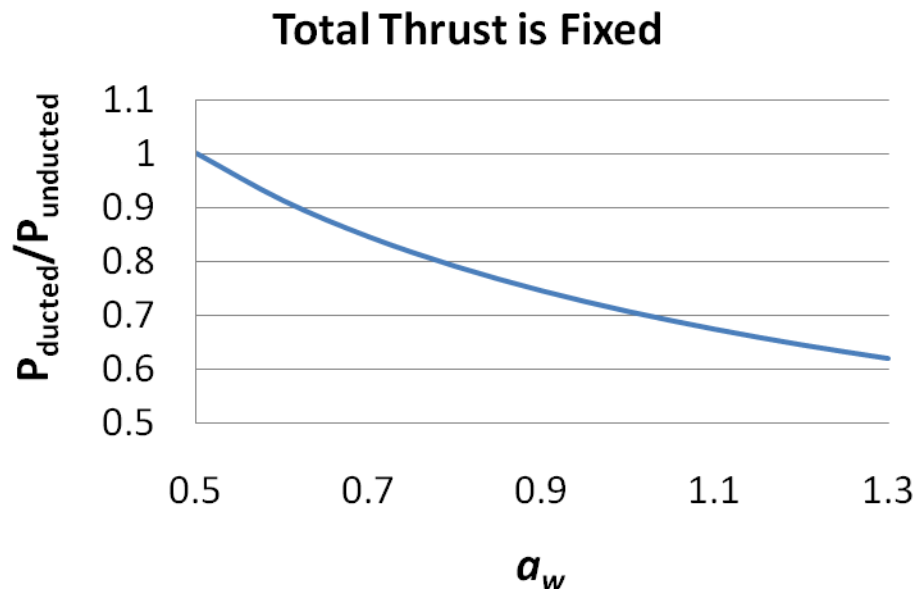


Figure 1.2: Power Consumption as a Function of Wake Expansion

If the total power consumed is the same for a ducted and unducted rotor, the total thrust produced increases for a ducted rotor as compared to an unducted rotor (figure 1.3) [1].

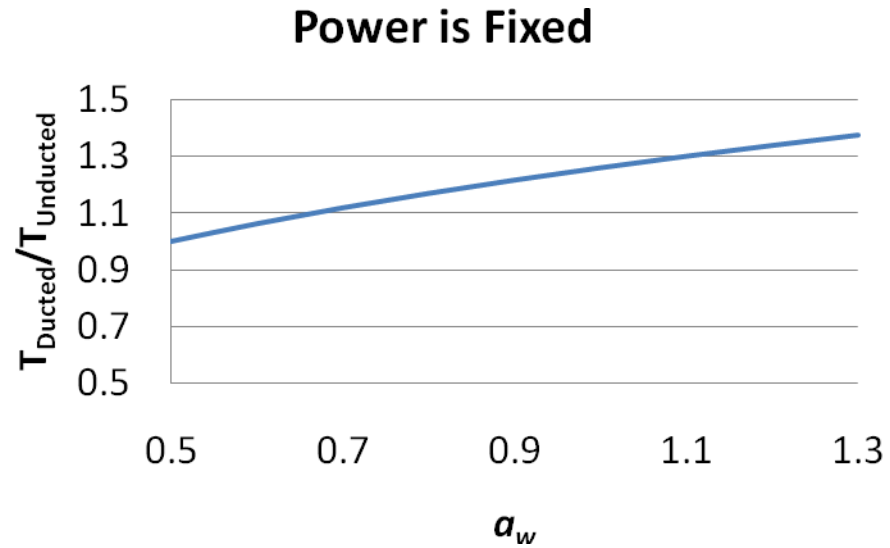


Figure 1.3: Trend of Thrust Increase as a Function of Wake Expansion

Finally, if the rotor thrust is fixed (figure 1.4), both the thrust contribution from the duct and power required increase, however, the power required is still lower than that of an unducted rotor operating at the same total thrust.

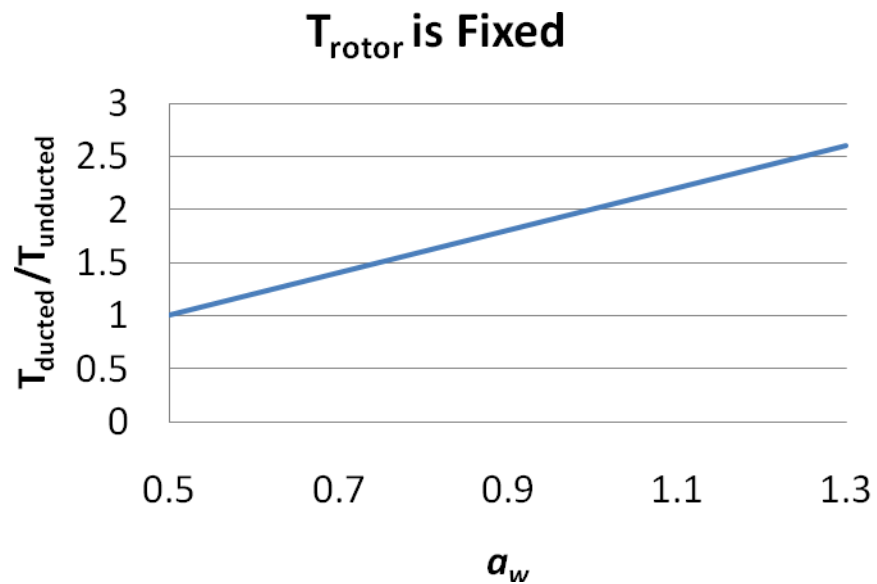


Figure 1.4: Total Thrust Increase as a Function of Wake Expansion

Figure 1.4 shows that for an a_w value of 1, the thrust has doubled over an unducted case for a fixed rotor thrust. If the power is fixed, the gain in thrust is only 26% (fig 1.3). This is because the induced velocity increases (Eqn 1.12) with the presence of a shroud so the rotor thrust must decrease to maintain the same power (Eqn 1.13). It will be shown later what an a_w value of 1 represents in terms of duct configuration.

Through a basic understanding of moment theory, ducted rotors have been shown to increase the overall performance of the rotor by increasing the parameter a_w . It will be outlined later how a_w is impacted by the duct geometry.

1.4 Overview of the Acoustic Problem

The ultimate goal of this research is to gain an understanding of the acoustics of a ducted tail rotor so that it can be predicted. There are two main parts of the sound field that will be examined individually. They are the sound produced by the rotor and the redirection of that sound due to the duct. The sound produced by the rotor is referred to as the incident field and the redirection of the incident sound is known as the scattered noise. The total sound field can be described as the sum of the incident field plus the scattered field [4].

$$p'_{total} = p'_{incident} + p'_{scattered} \quad (1.16)$$

where p' is the acoustic pressure .

The incident noise from a ducted rotor can be broken into several different parts [5]. Thickness noise and loading noise are known together as the rotational noise because they are the product of the rotation of a rotor. The thickness noise is caused by

the displacement of air and is dominant in the plane of the rotor. The loading noise, which dominates out of the plane of the rotor, is due to the acceleration of the loading force distribution over the rotor blade. A specific type of impulsive loading is associated with blade-vortex interaction (BVI). In the case of ducted rotors, a similar type of loading will be caused by the wake shed from vanes and struts then impacting the rotor. An illustration of the acoustic directivity of these noise sources is shown in figure 1.5.

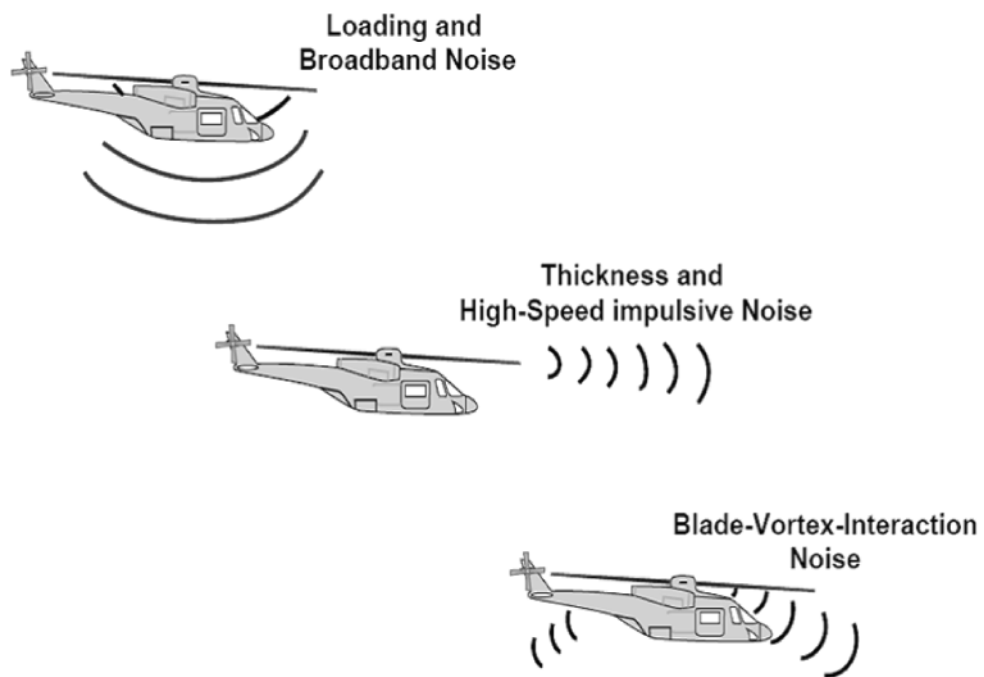


Figure 1.5: Directivity of Sound Types [5]

In the case of ducted rotors, the incident field will propagate away from the rotor to the duct where it will scatter. An obstacle or inhomogeneity in the path of a sound wave causes scattering if the secondary sound spreads out from it in a variety of directions (figure 1.6) [7].

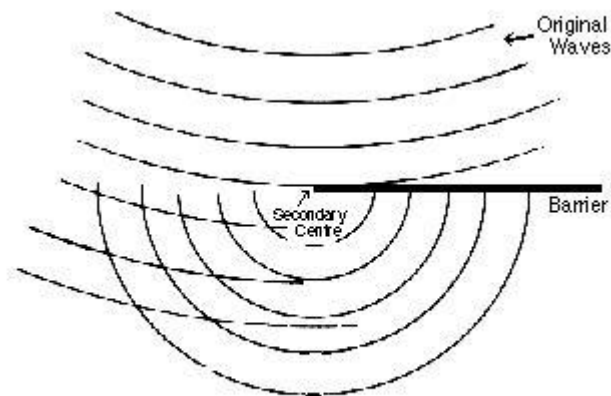


Figure 1.6: Scattering Example [8]

The scattering portion can change both the magnitude and directivity of the total sound field. This change is dependent on the wavelength of the incident sound relative to the characteristic length and position of the scattering body [9].

Because of the position differences, the sound field from a ducted rotor is scattered much differently from an open tail rotor. For a typical open tail rotor, there are little or no scattering bodies in plane of the rotor. The majority of the scattered field is from the frame of the aircraft (figure 1.7).



Figure 1.7: Open Rotor Example [8]

For a ducted tail rotor (figure 1.8), the sound field in the plane of the rotor is impacted much more significantly.

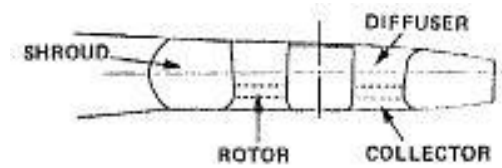


Figure 1.8: Fenestron Ducted Rotor [8]

The characteristic length of ducts also plays a large role in the scattering of the sound field. The wavelength of the blade passage frequency of a ducted rotor can be on the same order (if not equal) of the duct itself, thus various frequency components are scattered to varying degrees. These characteristics differ from the more classical case of fan noise radiating from a much longer duct in a turbofan engine (figure 1.9).

This research will examine two methods of calculating the scattering portion of the sound field. The first method is to calculate the sound in the very near field directly from CFD and applying Ffowes Williams-Hawkings equation to compute the sound radiated outside the duct. The second method is by using the equivalent source method to compute the scattered field directly.

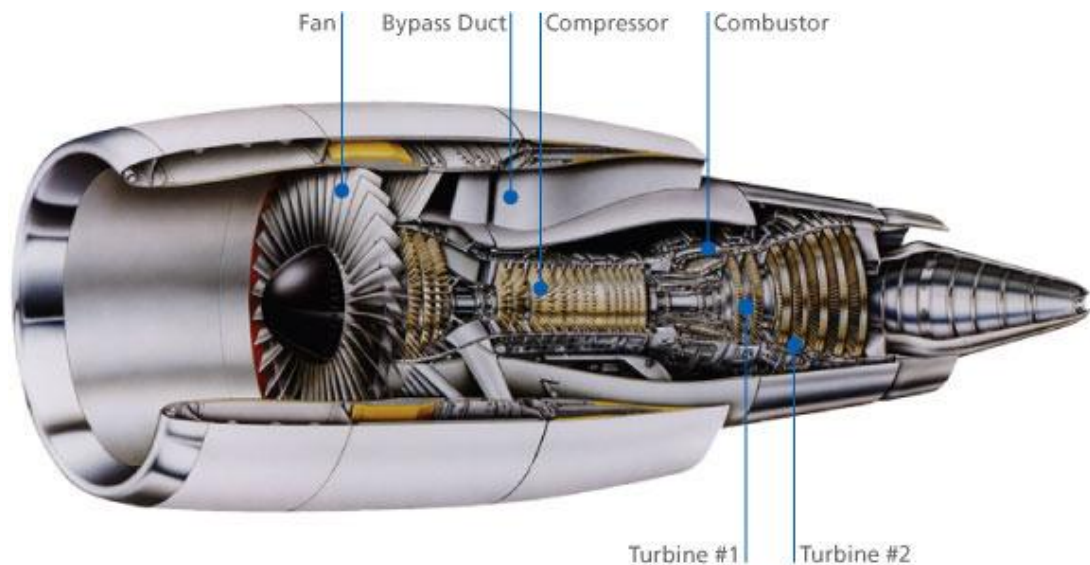


Figure 1.9: Turbofan Engine [10]

1.5 Ffowcs Williams-Hawkings Approach

One method to calculate the scattering due to the duct is directly from the CFD. A compressible flow computation in the source region (i.e. the flow around the rotor and duct) contains the acoustic field as well as the flow field. The unsteady flow information on the rotor blades and duct surfaces is used as input into the code PSU-WOPWOP which solves the Ffowcs Williams-Hawkings (FW-H) equation. The FW-H equation is an exact rearrangement of the continuity and Navier-Stokes equations into the form of an inhomogeneous wave equation [11]. To solve the FW-H equation, PSU-WOPWOP uses a time-domain integral formulation developed by Farassat [12, 13]. This formulation excludes the quadruple term of the FW-H equation and is valid for any rigid-body surface motion. Formulation 1A of Farassat which is used in this work may be written:

$$p'(x, t) = p'_T(x, t) + p'_L(x, t) \quad (1.17)$$

where p' is the acoustic pressure ($p-p_0$). The thickness contribution p'_T is calculated from

$$4\pi p'_T = \int_{f=0} \left[\frac{\rho_0(\dot{U}_n + U_{\dot{n}})}{r(1 - M_r)^2} \right]_{ret} dS + \int_{f=0} \left[\frac{\rho_0 U_n (r\dot{M}_r + c(M_r - M^2))}{r^2(1 - M_r)^3} \right]_{ret} dS \quad (1.18)$$

Where U is related to the velocity (eqn 1.17), r is the distance from the source to the receiver, M is the Mach number of the source, M_r is the Mach number of the source in the radiated direction.

The loading contribution p'_L is calculated by

$$\begin{aligned}
 p'_L &= \frac{1}{c} \int_{f=0} \left[\frac{\dot{L}_r}{r(1 - M_r)^2} \right]_{\text{ret}} dS \\
 &+ \int_{f=0} \left[\frac{L_r - L_M}{r^2(1 - M_r)^2} \right]_{\text{ret}} dS \\
 &+ \frac{1}{c} \int_{f=0} \left[\frac{r\dot{M}_r + c(M_r - M^2)}{r^2(1 - M_r)^3} \right]_{\text{ret}} dS
 \end{aligned} \tag{1.19}$$

The terms U_n and L_i are defined as

$$U_n = \frac{\rho}{\rho_0} (u_n - v_n) + v_n \tag{1.20}$$

$$L_i = p_{ij}n_j + \rho u_i(u_n - v_n) \tag{1.21}$$

where u_n is the normal velocity of the fluid and v_n is the normal velocity of the blade surface. In this work, the integrated surface is taken to be coincident with the physical surfaces of the rotor blade and the duct so $u_n = v_n$

The term $p_{ij}n_j$ in equation 1.18 is taken directly from the CFD simulations. The surface pressure was stored separately for the duct and rotor. The normal vectors come directly from the model geometry. It is important to note that the duct is being input into PSU-WOPWOP to simulate the scattering which is a new application of the code.

Ideally, the entire time history from the CFD would be input into PSU-WOPWOP to generate the noise signal of the ducted rotor. Unfortunately, the storage space needed to store all the time steps of the CFD was prohibitively large. The approach taken to calculate to noise over time was to run the CFD to a steady state solution and store the final time step. The final time step could then be input into PSU-WOPWOP and rotated at the rotational velocity of the rotor. This is valid because at steady state, the flow through the rotor is steady in the rotating frame of the rotor but it is still unsteady in the frame of the still air away from the rotor, hence it generates noise.

1.6 Equivalent Source Method

An alternative way of calculating the acoustic scattering caused by a duct is through the Equivalent Source Method (ESM). This method is used in the Fast Scattering Code (FSC) developed by NASA [9]. For this method, only the incident field (Such as the noise field of the rotor) and the geometry of the scattering body need to be known. The incident field itself comes from calculating the sound field generated by the rotor using PSU-WOPWOP. It is important to note that the ESM is only used to calculate the scattered field. The FSC has been applied to various simulations such as GE90-like engines and scale models of aircraft similar to the Boeing 777.

The theoretical formulation for the FSC was developed by considering a thin aerodynamic body through air with a sound source (figure 1.10) [9].

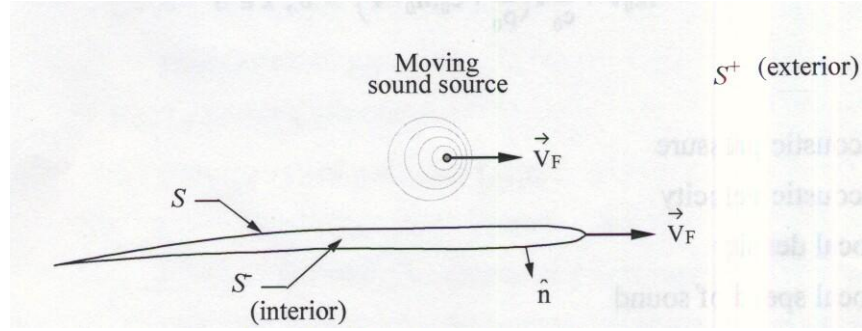


Figure 1.10: ESM Theoretical Formulation [14]

A small perturbation analysis was done on the mass and moment conservation equations to yield:

$$ik_0 p' + c_0 \nabla \cdot \left(\frac{1}{c_0} p' \vec{M}_0 + \rho_0 \vec{v}' \right) = 0 \quad (1.22)$$

$$ikv + \frac{1}{c_0} \nabla \cdot \left(\frac{p'}{\rho_0} + c_0 \vec{M}_0 \cdot \vec{v}' \right) = 0 \quad (1.23)$$

On the scattering surfaces, the acoustic pressure and velocity satisfy an impedance boundary condition given by:

$$\vec{v}' \cdot \hat{n} = Ap' \left[\frac{1}{ic_0 k_0} \hat{n} \cdot (\hat{n} \cdot \nabla c_0 \vec{M}_0) - 1 \right] - \left(\frac{1}{ik_0} \vec{M}_0 \cdot \nabla Ap' \right) \quad (1.24)$$

In the farfield, Sommerfeld's radiation condition is applied:

$$\lim_{R=|\vec{x}|\rightarrow\infty} R\left(\frac{\partial}{\partial R}p' + ikp'\right) = 0 \quad (1.25)$$

For scattering bodies without edges, these equations form a uniquely solvable boundary value problem (BVP) for scattered components of acoustic pressure and velocity with source terms provided by the incident sound field. The FSC solves the BVP assuming a uniform flow by default. For non-uniform flows, a correction factor is used but at low Mach numbers the correction is very small. The authors of the FSC are still investigating the effectiveness of the correction factor [14].

The BVP itself is solved using the ESM. The core of the ESM is to approximate the solution of the BVP by superimposing simple sources of sound [15] (monopoles, dipoles, etc.), and determine their strengths so that the acoustic boundary condition is satisfied [7].

The first step to the process is to cover the scattering surface with enough grid points (called collocation points) to capture the incident field fluctuations. Then a set of equivalent sources are constructed, which are placed on a small replica of the scattering surface (figure 1.11). The equivalent source surface is contained inside the scattering surface. The source surfaces are discretized in a similar manner as the actual scattering surface, but at a coarser spatial resolution. The strength of each source is determined using a matrix equation which is solved via LU decomposition. Once the scattering field is calculated, it can be added to the incident field to obtain the total noise field.

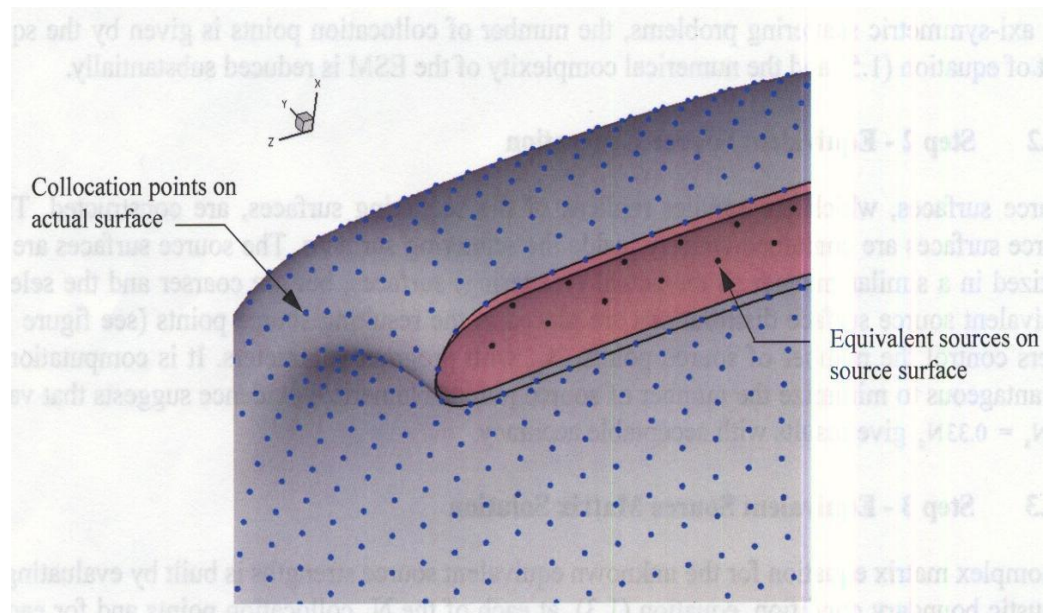


Figure 1.11: ESM Surface [14]

Overall, the ESM is less accurate than other boundary value methods but is much less computationally demanding and requires less memory and run time [14]. The run time efficiency makes it ideal for running many cases for the purpose of analysis.

1.7 Approach to Objectives

The final objective to this thesis is to gain an understanding of the sound field produced by a ducted rotor. Chapter 2 describes the manner in which the CFD data was obtained. It describes early computations with two dimensional, axisymmetric CFD predictions used to establish the expected mean flow field of a ducted rotor. The more detailed three dimensional CFD results are used to calculate the sound field are also described in chapter 2. A detailed description of how the CFD model was developed is given in appendix A. The converter which details how the CFD data was reformatted to be used in PSU-WOPWOP is contained in appendix B.

The heart of this research is described in chapter 3, which presents the acoustic field results. First, the acoustic results obtained by using the FSC will be presented and then the sound field results based on the CFD will be presented.

Chapter 2

Aerodynamics of Ducted Tail Rotors

In order to obtain an accurate sound field prediction, accurate loading on both the rotor and duct must be obtained. This must have the correct magnitude and distribution. The magnitude will impact the intensity of the noise as shown in equation 1.16, the loading noise component of the total sound field is directly dependent on the magnitude of the loading on the surface of both the rotor and duct. The loading noise is also inversely proportional to the distance from the source; hence the spatial distribution must be accurate.

All CFD work was done using the commercial CFD package, Fluent with Gambit for grid generation. The two dimensional figures that will be presented were done using Fluent version 6.2 [16] while the three dimensional cases used Fluent version 6.3 [17] that was made available later in the project.

Several steps were taken in order to gain an understanding of the duct aerodynamics. A two dimensional model of an axisymmetric duct was simulated and compared to momentum theory. This was to gain an understanding of impact the duct geometry had on the flow.

The majority of this chapter will be exploring a three dimensional rotor test subject. This test subject will be simulated with and without the duct to understand the changes in aerodynamics as well as the changes in loading on the rotor blades. Performance parameters such as thrust and power consumption will all be studied to assess the impact of the duct.

2.1 Two Dimensional Axisymmetric CFD

The first step in the CFD work was to explore predictions of momentum theory. This was achieved by simulating a rotor with a pressure jump in a two-dimensional axisymmetric case setup. The case was solved using a steady, incompressible, viscous flow solver. Viscous flow does violate an assumption of momentum theory but the

viscous solution would be more representative of the real flow solution. The viscous effects would only affect the solution near the rotor and duct surfaces; therefore, the flow should only experience minor changes. The computational domain for the two-dimensional axi-symmetric case is shown in figure 2.1. Unique to an axi-symmetric case is the axis boundary condition. This boundary condition sets the normal velocity to the axis to zero. In effect, the axis becomes a wall with a slip boundary condition. The velocity inlet condition allows the inflow velocity to be set. Ideally, the inlet is set far enough upstream that the velocity can be assumed to be zero, however, setting the velocity to exactly zero causes the flow to come from the sides or outlet to satisfy continuity. For this reason, the inlet velocity was set to a small non-zero number. The pressure outlet boundary conditions do not require any input because the conditions on those boundaries are extrapolated from the nearby flow field [16].

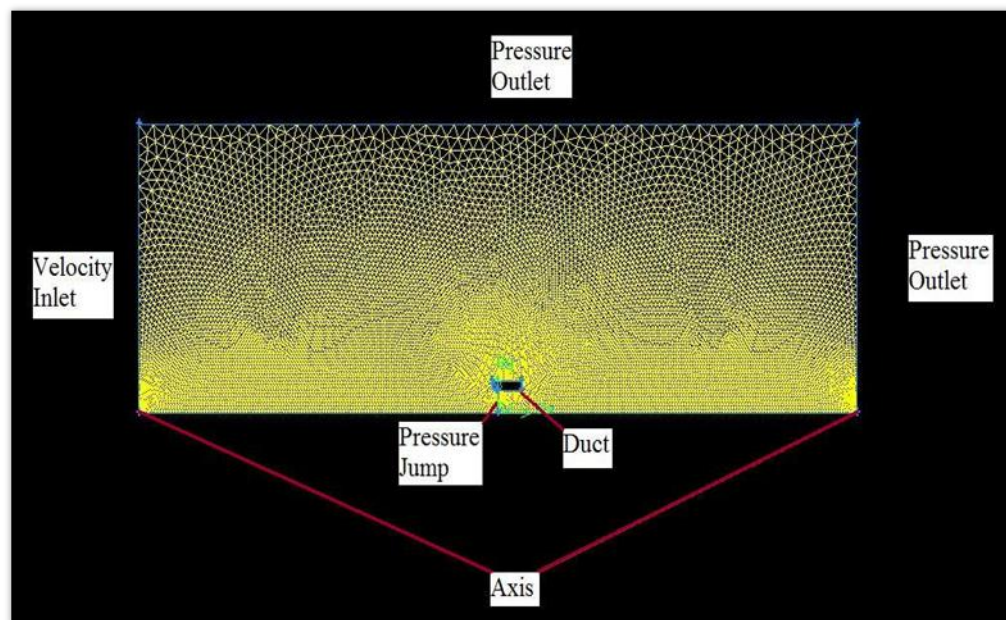


Figure 2.1: 2D Domain with Boundary Conditions

Three cases were simulated and examined: 1) a rotor without a duct; 2) a duct with 0 degrees of diffusion; and 3) a duct with 4 degrees of diffusion. The purpose of these configurations was to investigate the wake formation. The wake formation is very

important in ducted rotor calculations because it is used to calculate the parameter “ a_w ” which is a correction factor between ducted and unducted rotor equations.

The first case tested was an unducted rotor (figure 2.2). The streamlines were plotted to show the development of the wake. Also, all of the figures are zoomed into the rotor area for clarity. The actual domain used in the simulations is much larger than shown so the boundaries do not affect the results of the simulations in the region of the rotor. For the purpose of this analysis, only the flow near the rotor is of interest. The white vertical line shown at the bottom center on the figures represents where the pressure jump (representing the rotor disk) is applied.

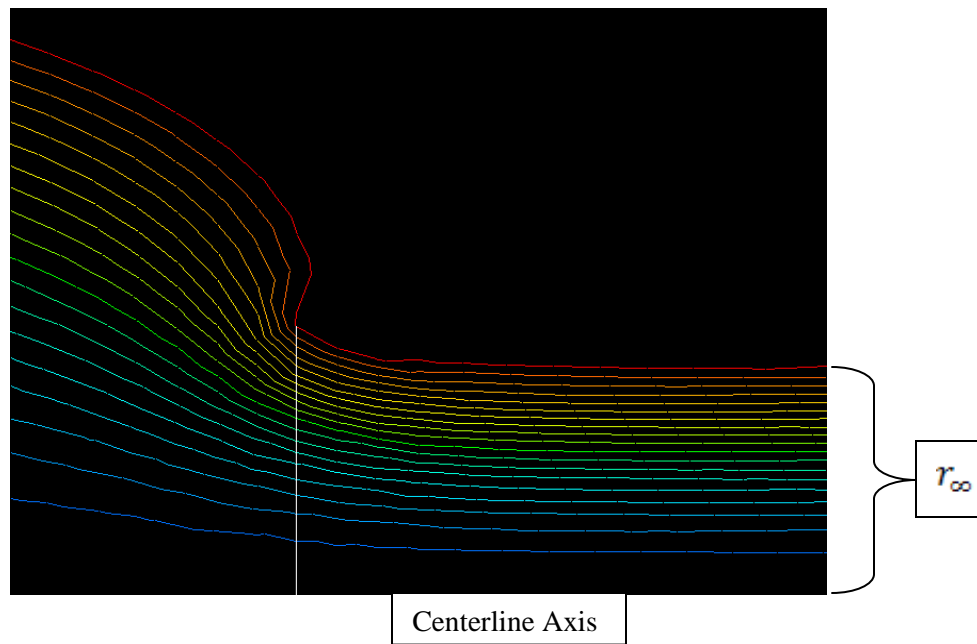


Figure 2.2: 2D Unducted Rotor Streamlines

The measured ratio of the fully contracted wake to the rotor area was about 0.6. This differs from the theoretical value 0.5 but is very close to a typical value of 0.61 [1]. This shows that the simulation can accurately predict the wake contraction for a more physical case. Note that the far field wake area was calculated by considering the streamline that passed through the very tip of the rotor disk.

The second test run was on a ducted fan with a zero degree diffuser angle (figure 2.3). As shown in figure 2.3, with the presence of the shroud, the wake did not contract. The measured value of a_w was 1.03 – a 3% expansion. A duct with a zero degree diffuser angle would be expected to have an a_w value of 1. Also the thrust contribution of the duct in this case was calculated to be 3506 N. The thrust on the duct was calculated by using FLUENT, integrating the pressure around the surface of the duct and taking the component in the flow direction. This will be compared to the other cases in figure 2.5.

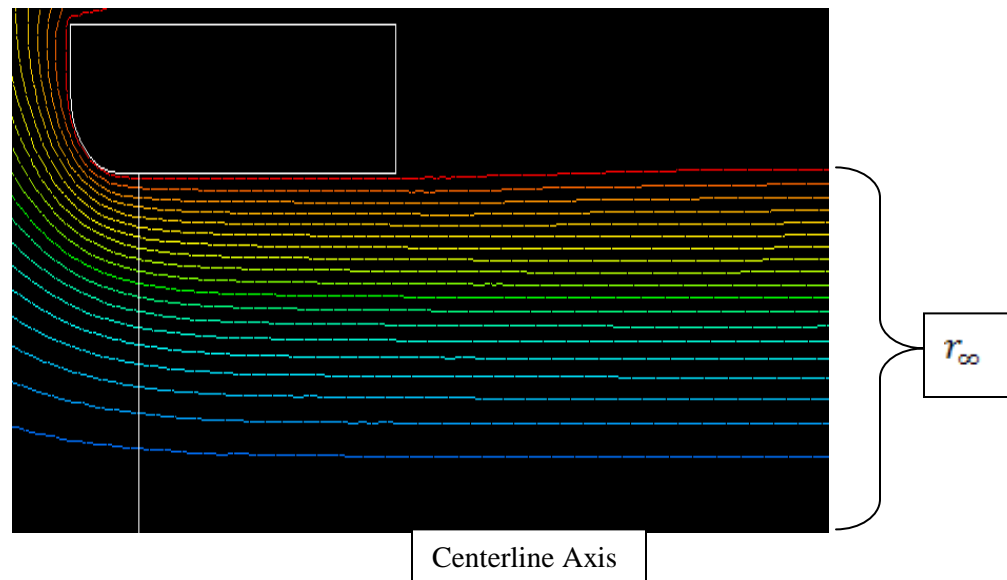


Figure 2.3: 2D Zero Degree Diffuser Angle Duct Case

Finally, a duct with a four degree diffuser angle was simulated (figure 2.4). This duct had the same length and inlet shape as the zero degree duct case. The streamlines in figure 2.4 show much expansion inside the duct and downstream of the outlet. This case shows an a_w of about 1.215. The higher duct angle translates to more wake expansion and higher thrust contributions from the duct. For this case, the duct thrust was calculated to be 4629 N.

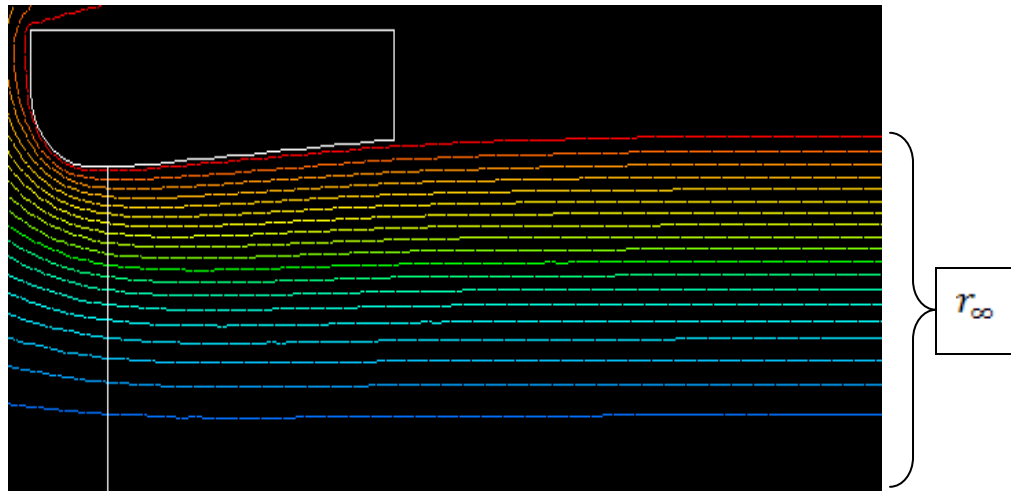


Figure 2.4: 2D Four Degree Diffuser Angle Duct Case

Figure 2.5 compares the theoretical and simulated trend of the duct thrust as a function of a_w . The theoretical values are based on the rotor thrust and area given earlier and standard sea level density. Note that there is an offset thought to be mainly due to the viscous losses that were included in the simulations and not in momentum theory.

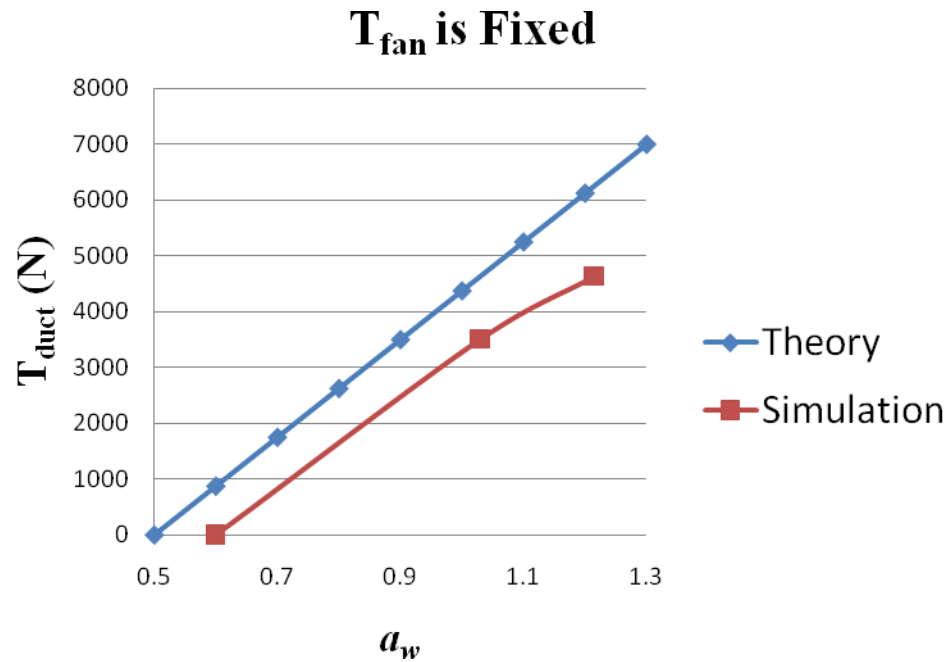


Figure 2.5: 2D Results Compared to Theory

Despite the offset, the same general trend was observed. Increased a_w and duct thrust values were measured for larger diffuser angles. Clearly expanding the flow more can lead to better tail rotor performance. Please note that the magnitude of the pressure jump is fixed for all three cases, which is the same as fixing the rotor thrust.

Although expanding the flow offers dramatic performance improvements, there is a limitation to the expansion of the flow illustrated in figure 2.6. The limitation comes from the possibility of flow separating from the duct wall [1]. This is due to the flow decelerating because of the expansion causing a rise in the static pressure. Also, ducts are typically short (no more than 1 rotor diameter long) to reduce weight [6]. Since a pressure gradient is inversely proportion to the distance which the expansion occurs over, these two factors combine to cause a significant adverse pressure gradient which puts the flow at risk of separation from the duct wall (figure 2.6), in which case the flow will not expand as expected causing a drop in a_w . As shown in the theory, the decrease in a_w will decrease the performance of the rotor.

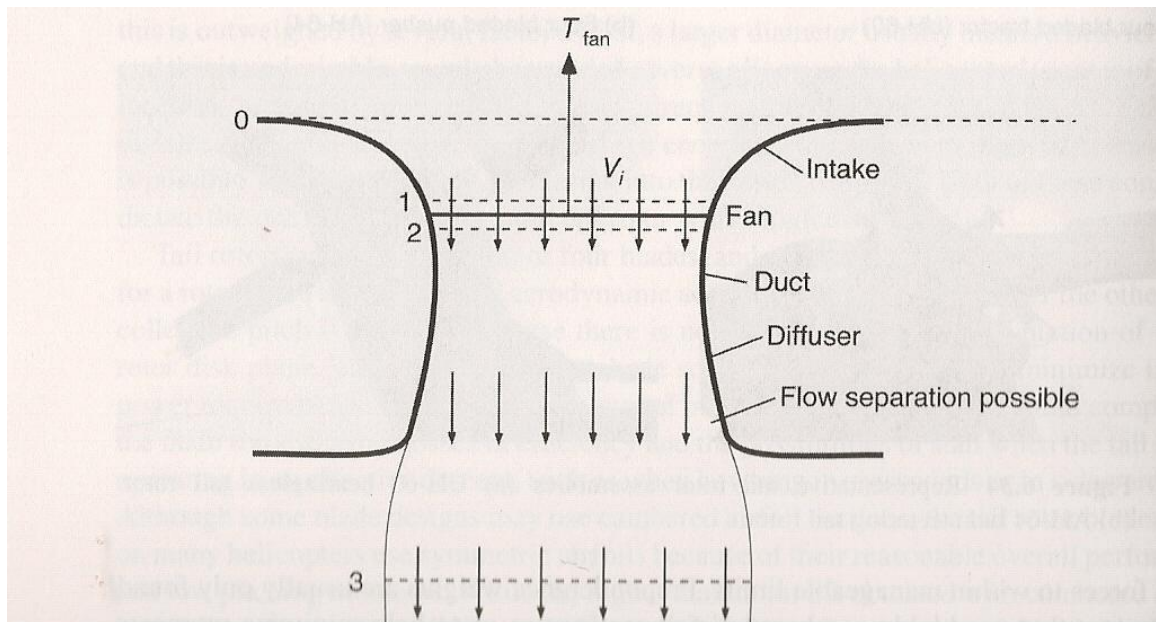


Figure 2.6: Area Where Flow Separation is Possible [1]

2.2 Three Dimensional CFD

Three dimensional, viscous, compressible flow simulations were conducted on a rotor/duct configuration, provided by an experimental team at Penn State, so the case could be compared to wind tunnel data. Figure 2.7 shows the duct studied in this research.

The key parameters of Figure 2.7 are;

- Rotor Radius = 0.1161m
- Tip Clearance = 0.005058m (4%)
- Rotor Rotation Rate = 1757.1 rad/s
- Duct Length = 0.153m

For more detailed information about the duct and rotor geometry, see appendix A.

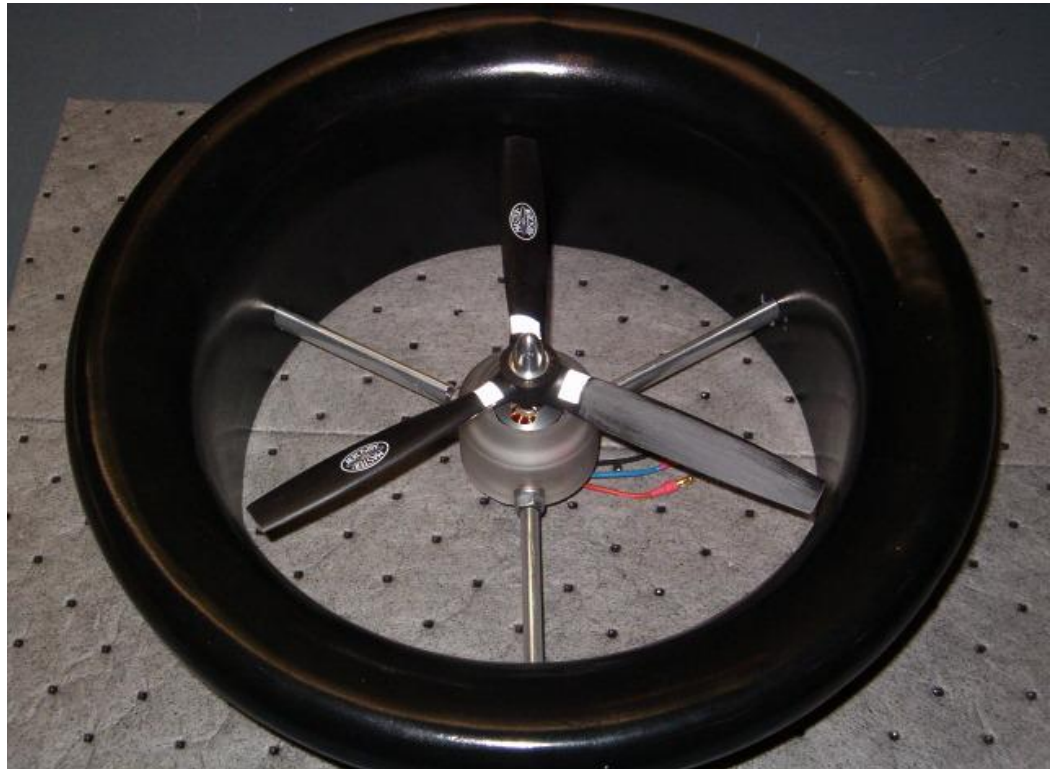


Figure 2.7: Ducted Rotor Used for Experimenting and Simulations [18]

For the initial simulations, the struts were not modeled. The center hub will also be simplified (figure 2.8). The goal of the simulations is to gain an understanding of the overall flow and noise characteristics before exploring how additional features, such as struts and vanes, will impact the flow and noise. It is also important to note that the rotor used by the experimental team was not originally designed to be used in a ducted rotor. Part of the design of a ducted rotor is to treat the tips to prevent tip leakage which is a large amount of flow passing between the duct wall and the tip of the rotor blade. With this treatment lacking, flow around the tips of the rotor blades can be expected. The rotor was also rotated at a much higher speed in the simulations than what the experimental team tested. This was done to ensure that the sound levels would be significantly high for the purpose of acoustic analysis.

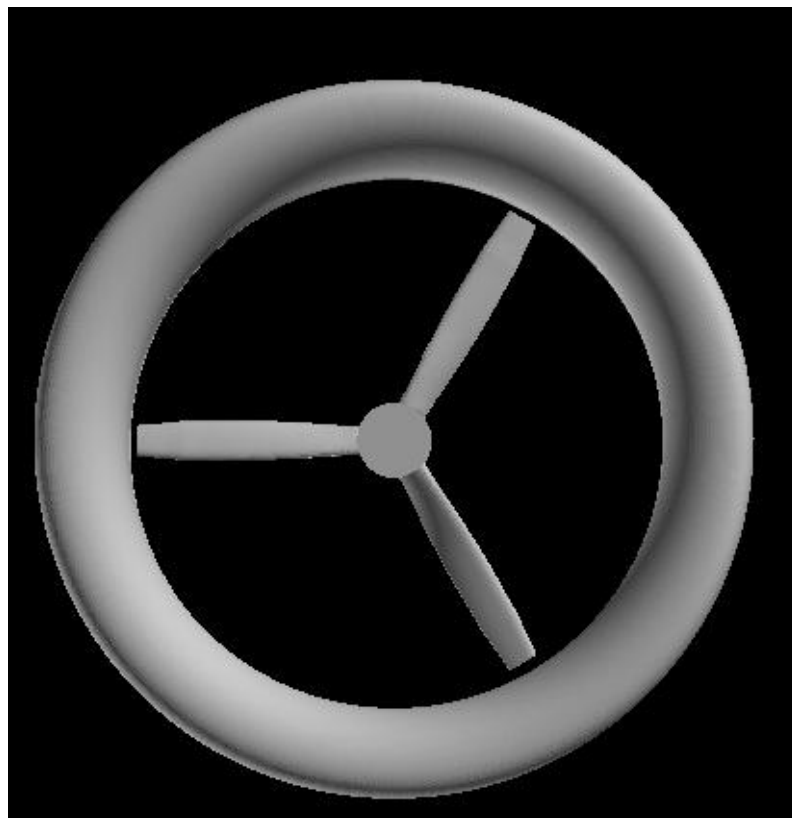


Figure 2.8: Simplified Computational Model

2.2.1 Ducted Rotor

The simulation was run until the pressure contours developed (figure 2.9-2.12), start up flow anomalies propagated away from the near field (figure 2.15-2.17), and the thrust of both the rotor and the duct no longer varied with time (figure 2.23). The pressure contours along the rotor blades and duct were also checked to ensure that the distribution was consistent with what could be expected based on published data of similar rotors. In all pressure figures, the gauge pressure in Pascals is shown. Figure 2.9 is an overview of the duct and rotor together. Each of the components will be evaluated individually in more detail.

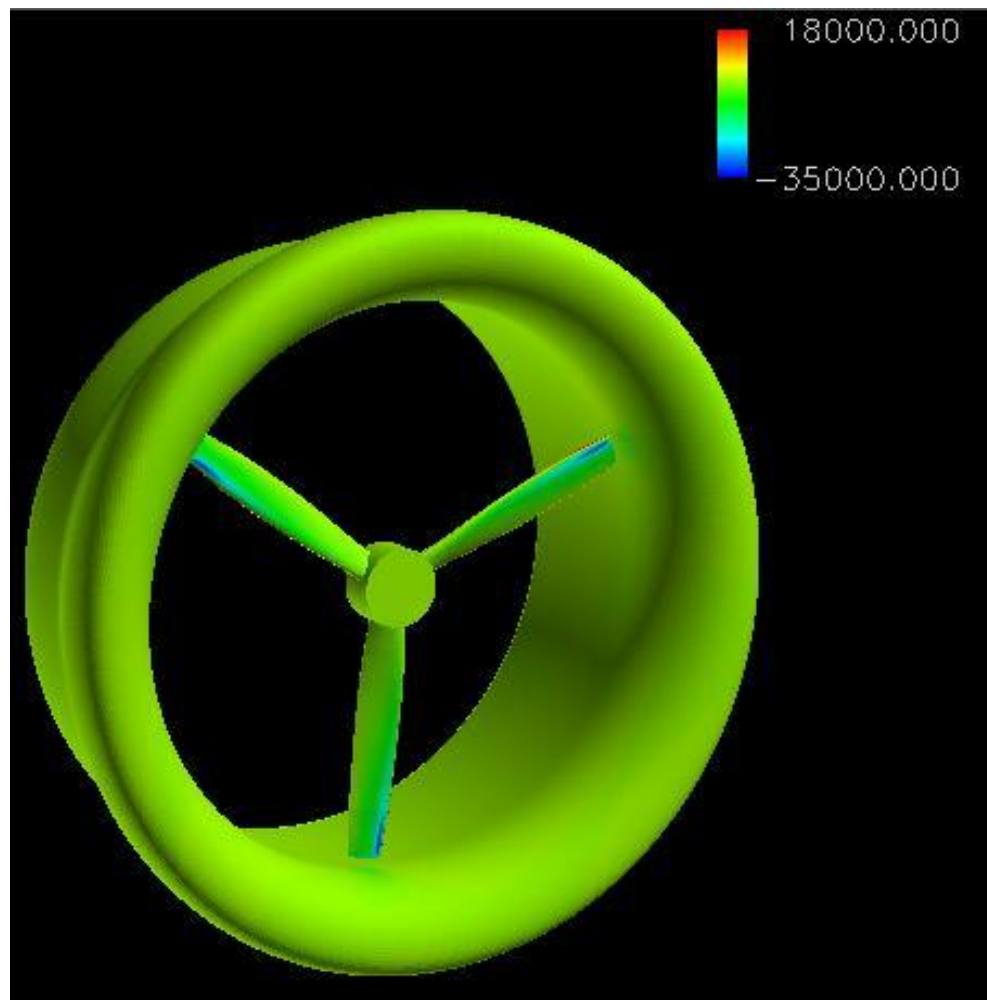


Figure 2.9: Duct and Rotor Pressure (p' , Pa)

The next examination is of the rotor itself (figure 2.10). When the rotor reaches a steady state, the pressure is expected to be low on the upper side of the rotor blades and high on the leading edge. Figure 2.10 shows an expected spanwise pressure distribution as well as the leading edge stagnation point. The spanwise pressure distribution will be examined in more detail later when compared to the open rotor (figure 2.29-2.30).

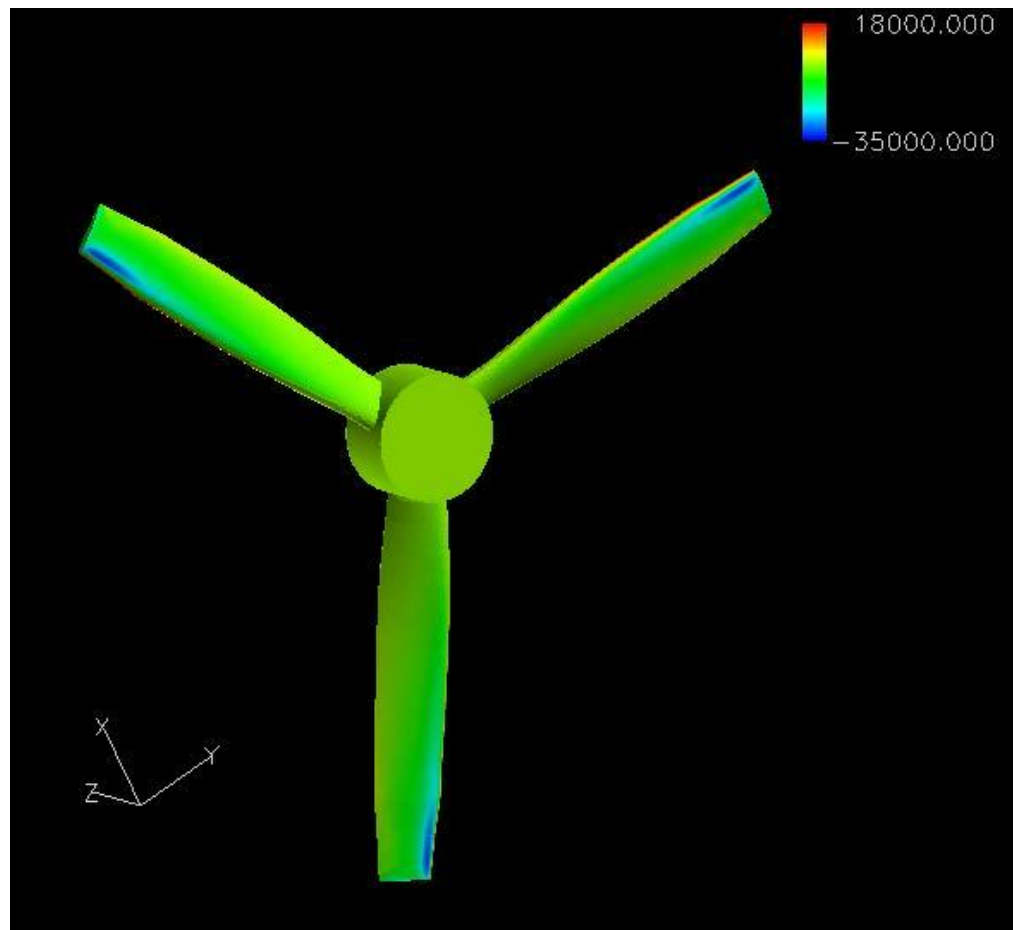


Figure 2.10: Ducted Rotor Pressure (p' , Pa)

The pressure on the duct wall is also an area of interest. Although the tip clearance of the rotor is very large (4% of rotor radius), there is still expected to be a strong influence from the rotor on the duct wall, which is what is seen when the pressure field on the duct examined in figure 2.11. Note that the scale of contours has been changed to clearly show the influence of the rotor.

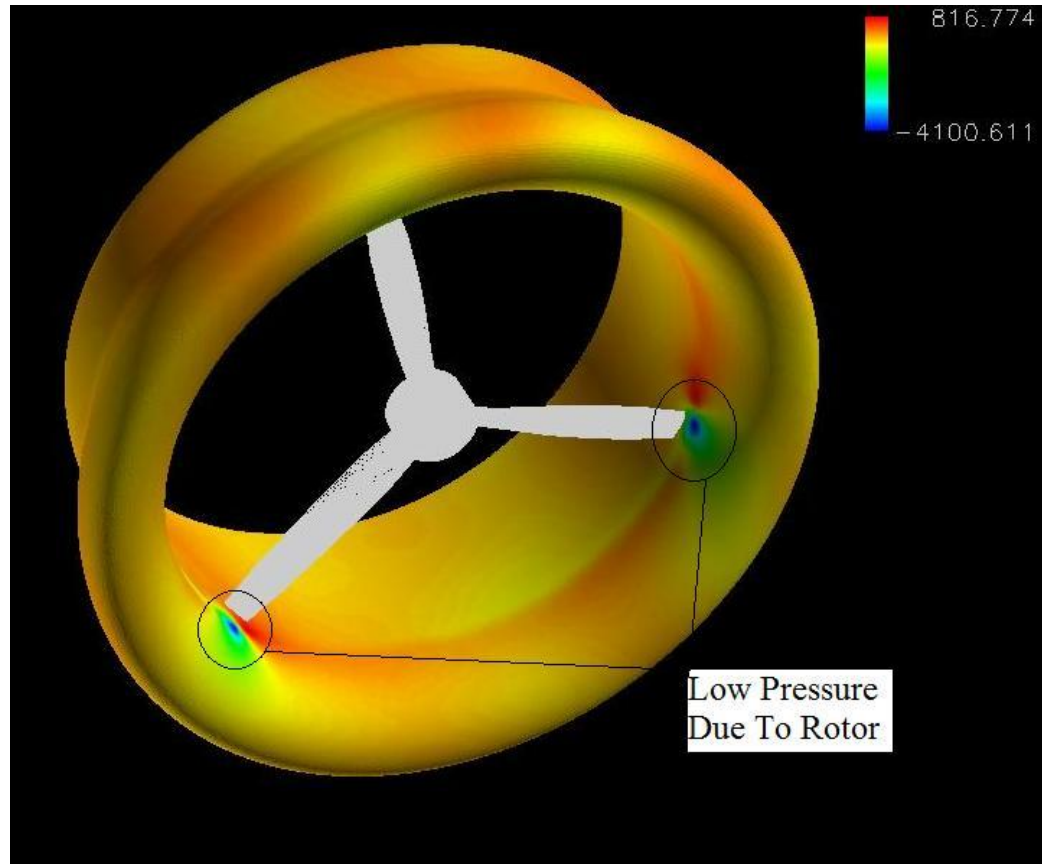


Figure 2.11: Rotor Blade Influence on Duct Wall Pressure (p' , Pa)

Low pressure areas were detected where each of the blades of the rotor were passing the duct wall. There is also a wake deficit on the wall following each of the blades. To illustrate this more clearly, the pressure contours are shown on a cross section of the duct in figure 2.12.

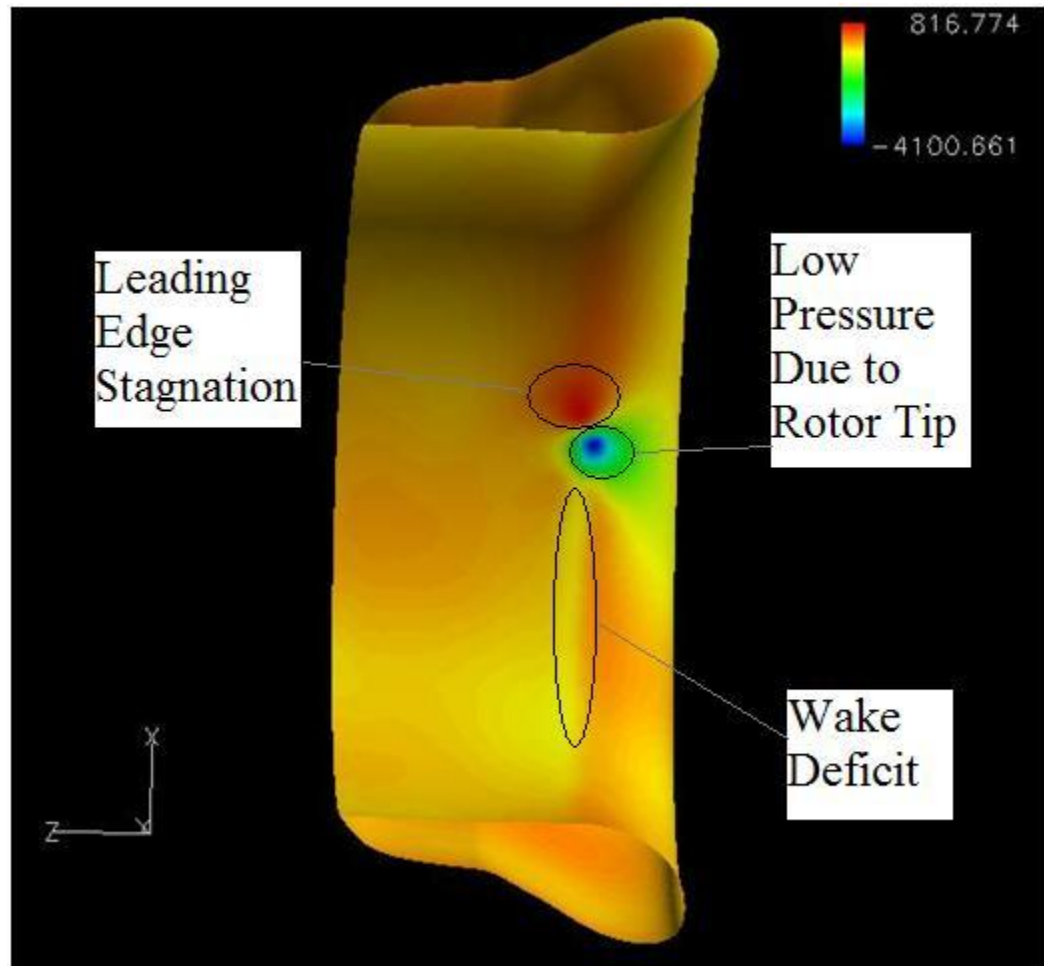


Figure 2.12: Inside Duct Wall Pressure Features (p' , Pa)

Three areas of interest are in front of the rotor path, at the rotor, and behind the rotor. A high pressure area in front of the rotor indicates the stagnation point on the rotor is having an impact on the duct. At the rotor blade, the pressure is low due to the increasing velocity from the rotor accelerating the air. This impact extends toward the lip of the duct. Downstream of the rotor, there is a section of the duct that is impacted by the wake of the rotor. This is apparent from the distinct line along the duct wall in the plane of the rotor. All of these phenomena are important for calculating the loading noise produced by the duct. The pressure around the duct wall off the tip of the rotor (figure 2.12) indicated locations of blade passage.

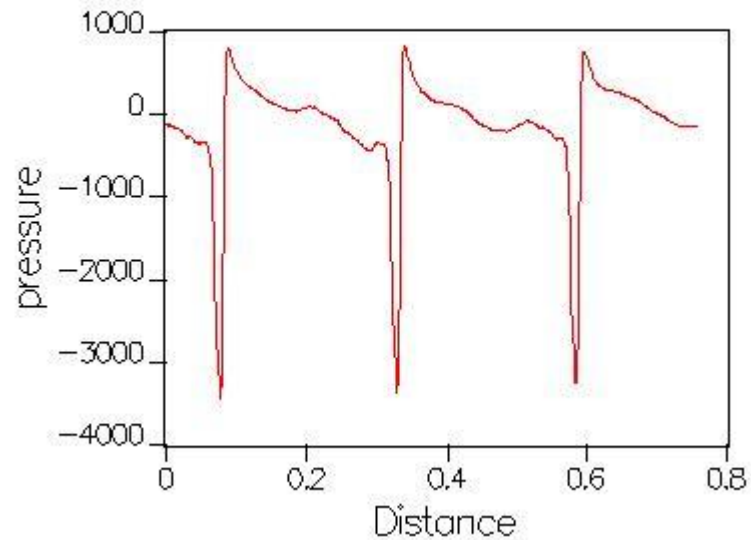


Figure 2.13: Pressure on the Duct Wall in the Plane of the Rotor Blade (p' , PA) the distance is the circumferential distance around the duct wall.

Another area of interest is the wake formation and the area of the wake far from the rotor disk. Having a well defined wake is important for momentum theory calculations in which the area of the downstream wake is very important. To illustrate the wake development, the following figures will show the wake at two instances in time. The first instance is early in the run, which is approximately two rotor revolutions from the start. The second instance in time is near the end of the simulation which is after at least 8 rotor revolutions.

For clarity, the figures show a close up of the duct area and are a two dimensional slice. The actual domain is much larger and three dimensional. Figure 2.14 shows the contours of velocity early in the simulation. As shown, the downstream wake is not very uniform. To better illustrate the flow directivity in the downstream area, the velocity vectors were plotted (figure 2.15) which shows a very obvious starting vortex. This is believed to be due to start up because it does not appear later in the simulation. The simulation was started with the fluid being at rest so rapid changes in flow velocity are the likely source of any vorticity.

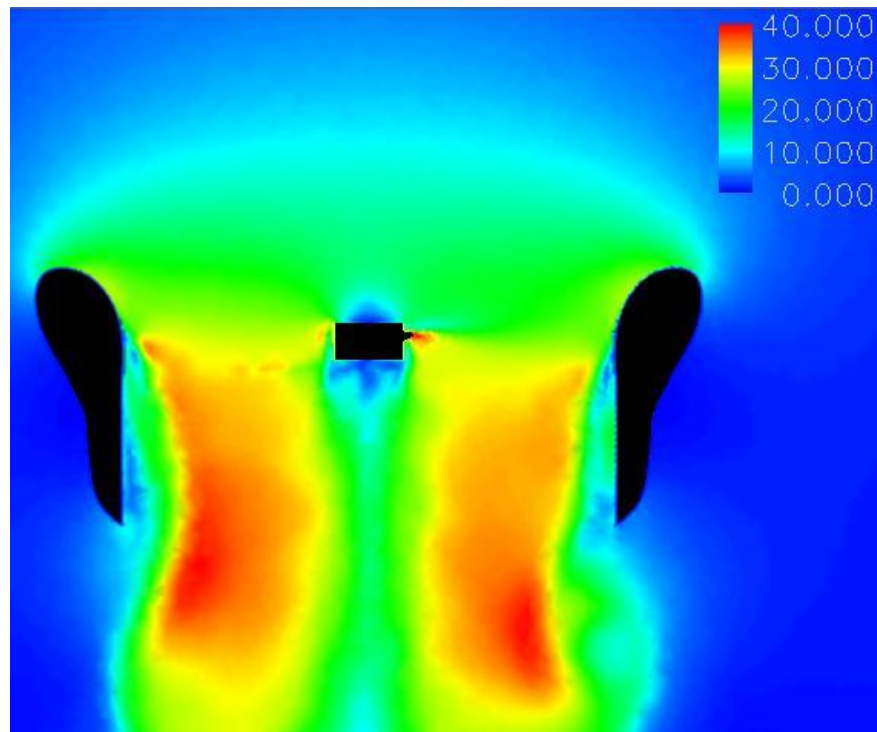


Figure 2.14 Early Ducted Rotor Velocity (v , m/s)

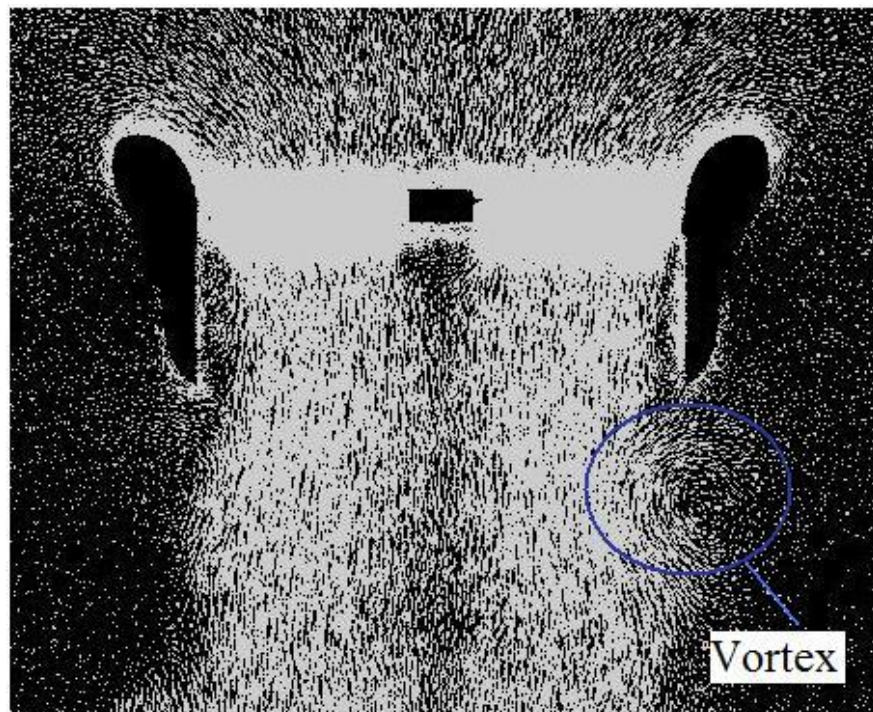


Figure 2.15: Early Ducted Rotor Wake Profile

The inflow into the duct is already well developed in the early stage of the simulation.

At a time much later in the simulation, the downstream wake becomes more uniform as shown in figure 2.16.

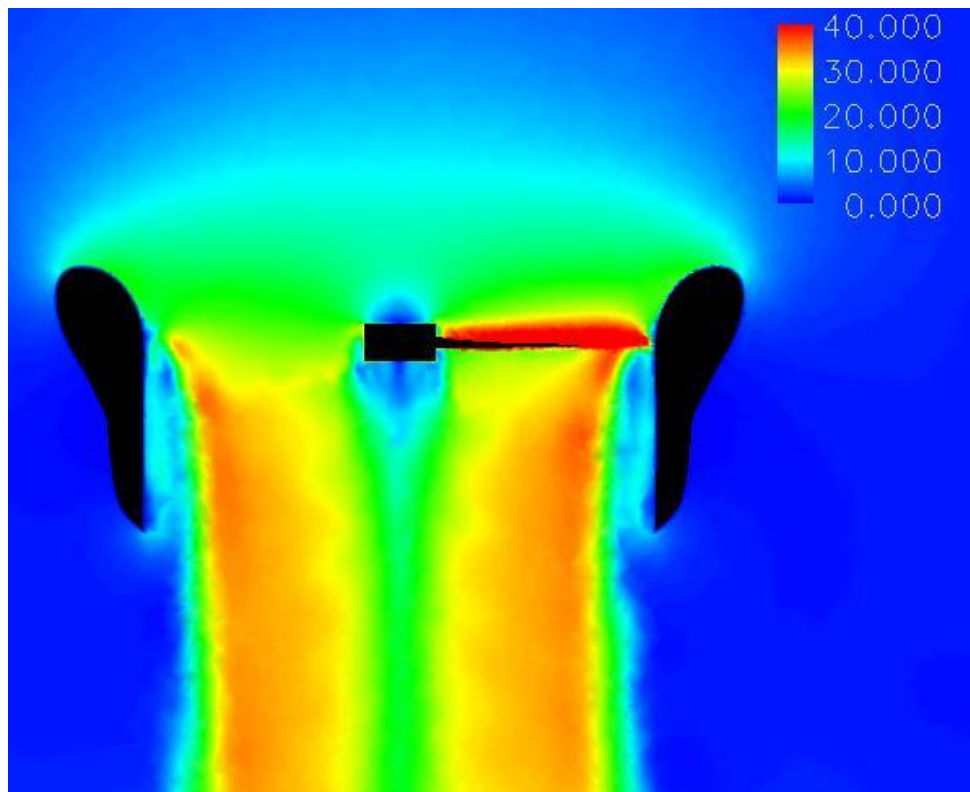


Figure 2.16: Ducted Rotor Developed Velocity Contours (v , m/s)

The slower portion in the middle of the wake is due to blockage from the rotor hub. It was expected to see higher velocity all the way out to the duct wall inside the duct but that is not the case. In order to evaluate the flow inside the duct, the velocity vectors were plotted.

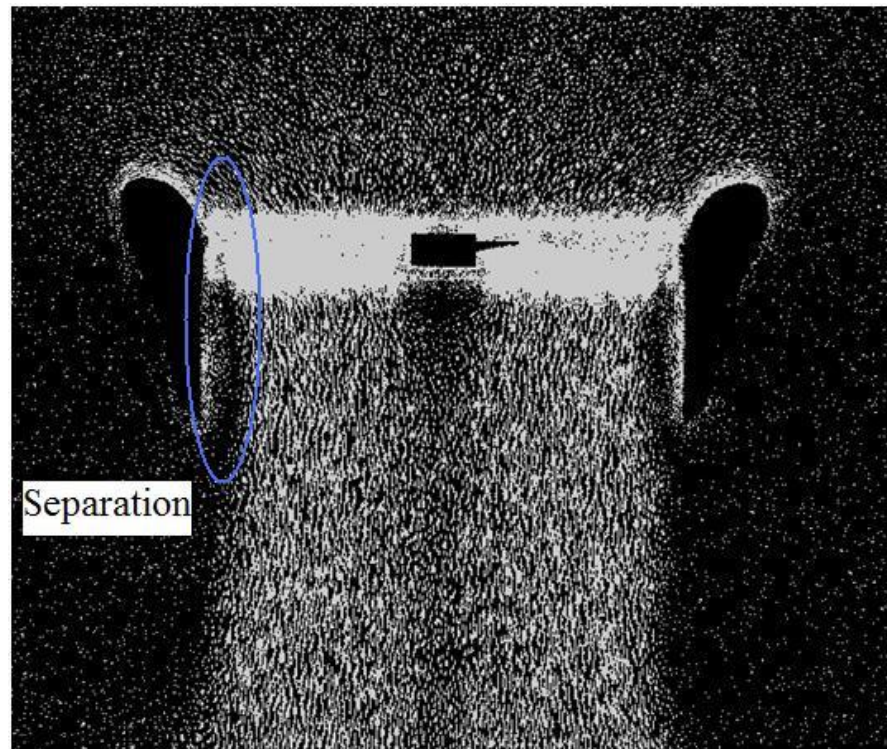


Figure 2.17: Ducted Rotor Developed Wake Profile

The area near the rotor is hard to see because of the denser meshing (Appendix A) but the downstream wake is of more interest. In earlier figures pertaining to momentum theory, the wake stayed attached to the duct wall. In figure 2.17 there are some obvious signs of separation from the duct wall. This is thought to be due to the higher tip Mach number and the rotor is not designed for use in ducts.

The separation is due to a small tip vortex developing inside the duct (Figure 2.18, 2.19) which seems to pull the flow off the duct wall. This also results in an area of recirculation in the downstream half of the duct (Figure 2.20).

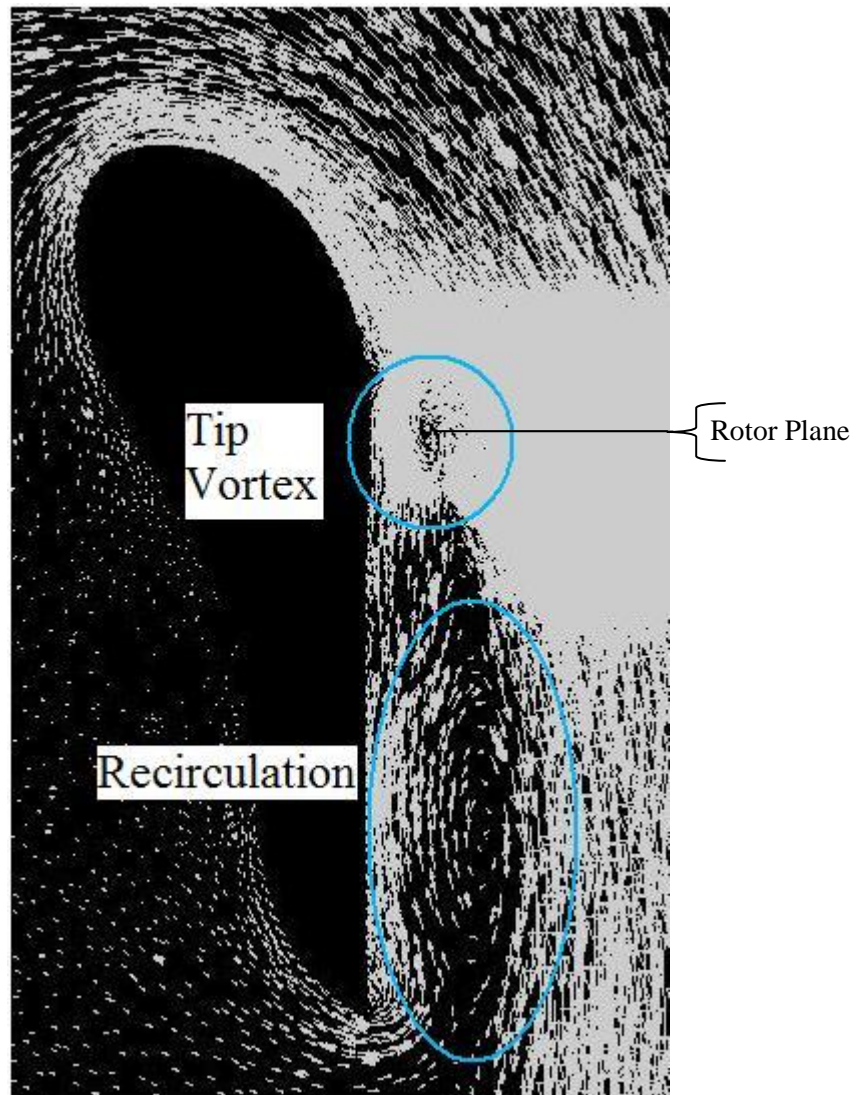


Figure 2.18: Separated Duct Flow

Figure 2.18 is meant as an overview of what is happening on the duct surface from inlet to outlet. This inlet (figure 2.19) and outlet (figure 2.20) will be examined more closely individually. As the flow comes over the lip and into the duct in figure 2.19, the vortex appears to cause flow from the duct wall into the center area of the duct. This causes the flow to separate from the duct wall and forms a deficit down stream of the rotor which causes recirculation into the duct (figure 2.20).

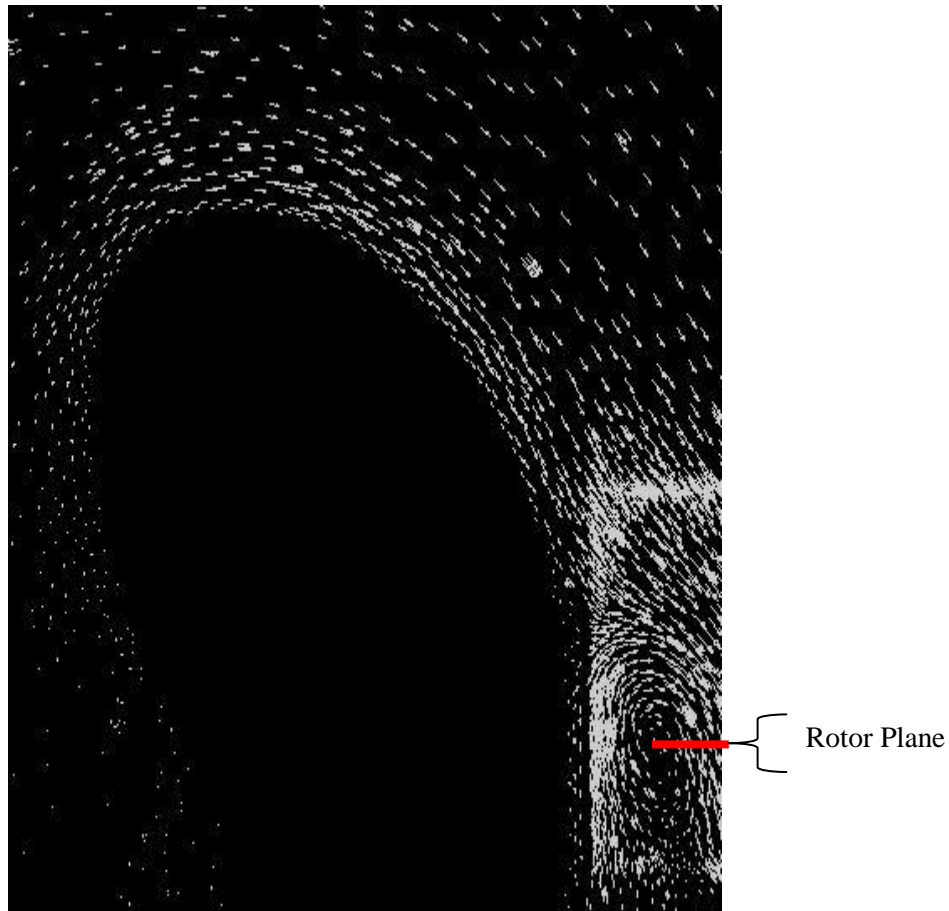


Figure 2.19: Duct Inlet and Tip Vortex

In figure 2.20, the flow clearly comes back into the duct and causing a second vortex which keeps the main flow off the duct wall. If, when, and how frequently these vortices shed could not be conclusively determined by the flow data because the amount of time steps that would need to be stored to determine specific information on the vortices required too much computer storage space. Because of the two vortices shown in figure 2.19 and 2.20, the flow inside the duct contracts which will impact the far field wake area. Because of this, it is not expected that the wake contraction parameter of the three dimensional case will behave exactly like the two dimensional cases (figure 2.2-2.4) because in those cases, the flow stayed attached to the duct wall and did not contract inside the duct.

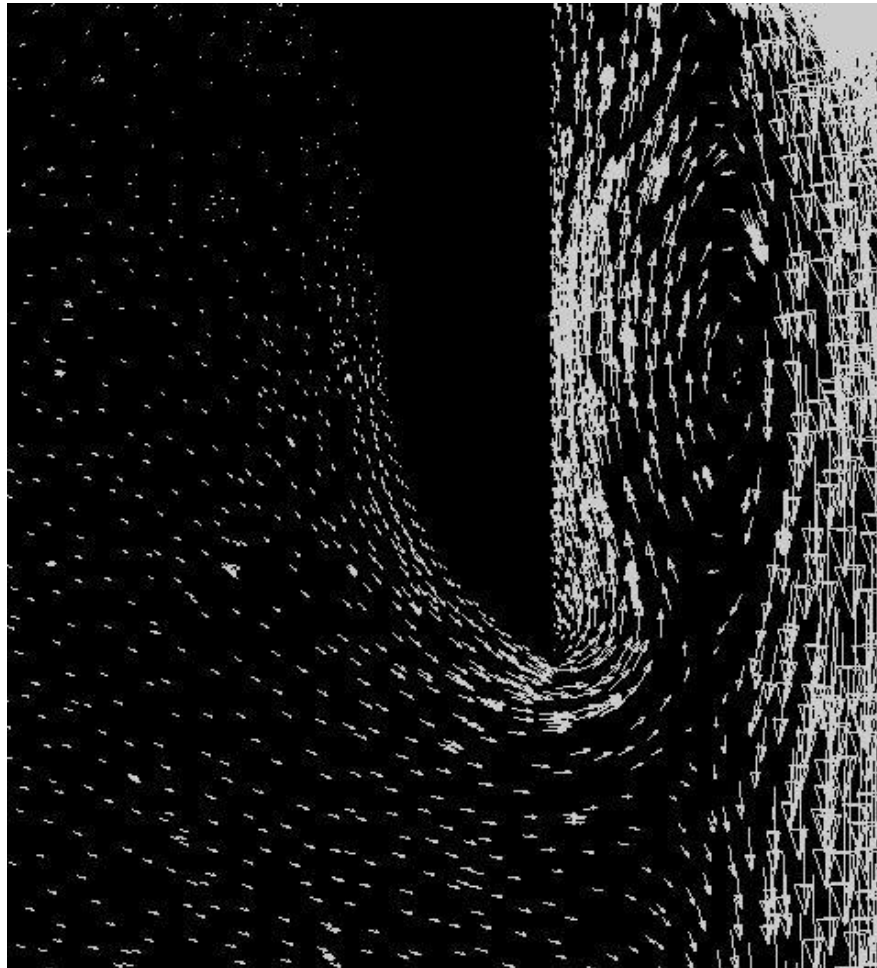


Figure 2.20: Duct Outlet and Recirculation

As a reminder, the wake contraction parameter is defined as the ratio of the area of the far field wake to the area of the rotor (equation 1.9). The area of the rotor in any analysis work is known, however, an accurate calculation of the far wake area is more challenging. The three dimensional wakes are not perfectly circular due to the separation and turbulence, so streamlines could not be used to calculate the downstream wake accurately. Instead, a cut of the downstream wake was made using an iso-surface in FIELDVIEW (figure 2.21).

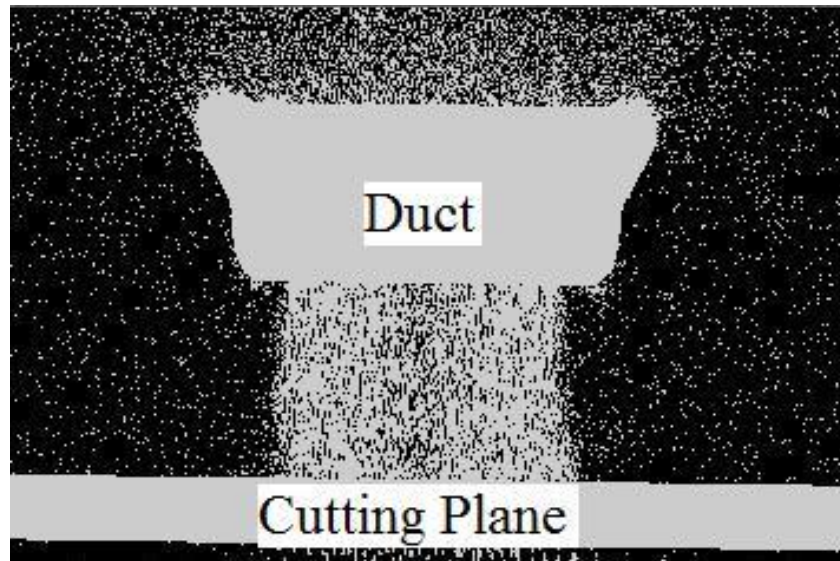


Figure 2.21: Wake Cutting Plane

On the cutting plane, a threshold velocity can be set so that anything below it is not displayed. This is useful for obtaining an image of the flow wake (figure 2.22). The image in figure 2.22 is taken from $10R$ downstream of the rotor and is determined to be converged because $0.5R$ upstream and downstream yielded the same area. The threshold velocity was taken to be the minimum velocity in the center of the flow (due to blockage by the hub). Much beyond $10R$, the flow velocity became too small to determine the core flow. By calculating the area of this cross section, a_w was determined to be 0.8 which is lower than the expected value of 1. This result, however, is not unreasonable considering the flow separation causing the wake to contract inside the duct. It is also important to note the sensitivity to this calculation. Decreasing the threshold velocity by just 1 m/s ($\sim 5\%$) can cause a change of up to 10% in a_w . The cross section of the wake downstream show quite a bit of deviation from the uniform profile seen just downstream of the rotor (Figure 2.23, note that the black ring indicates the duct).

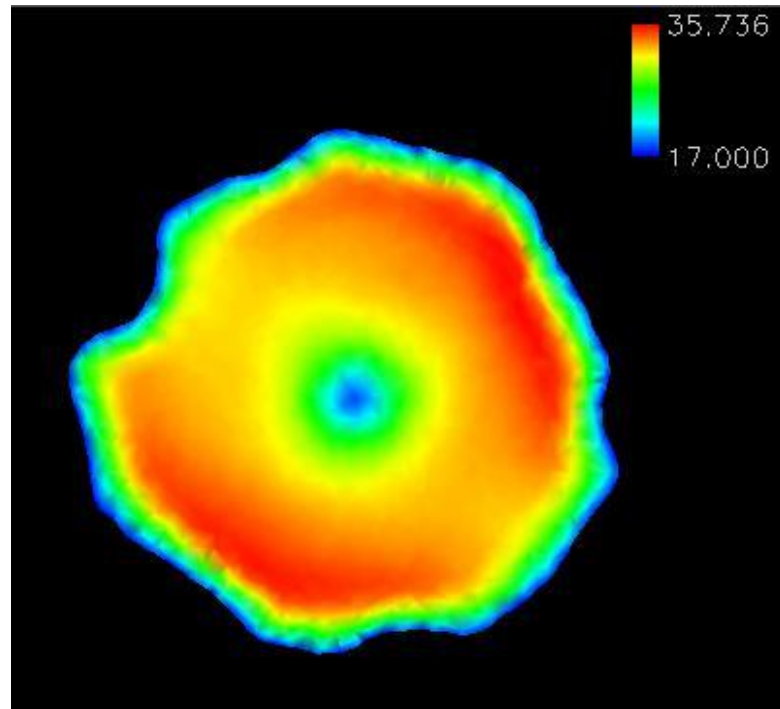


Figure 2.22: Ducted Rotor Far Wake (v, m/s)

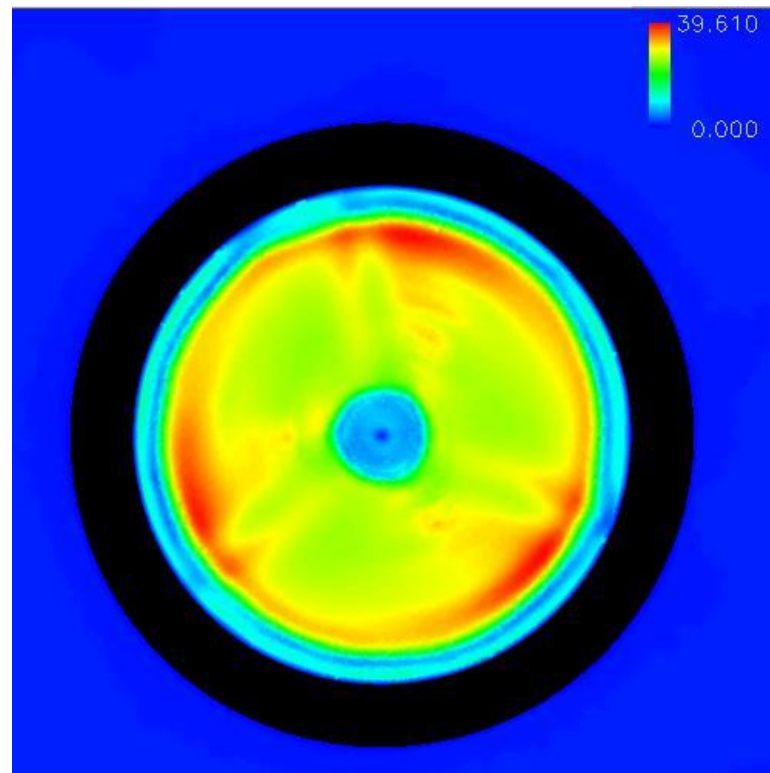


Figure 2.23: Ducted Rotor Near Wake (v, m/s)

Despite flow separation and recirculation, the thrust level of the rotor did converge, however, the thrust level of the duct continued to show a few fluctuations over time. Each component of the thrust was plotted vs. time (Figure 2.24). Every ~500 time steps represents 1 rotor revolution.

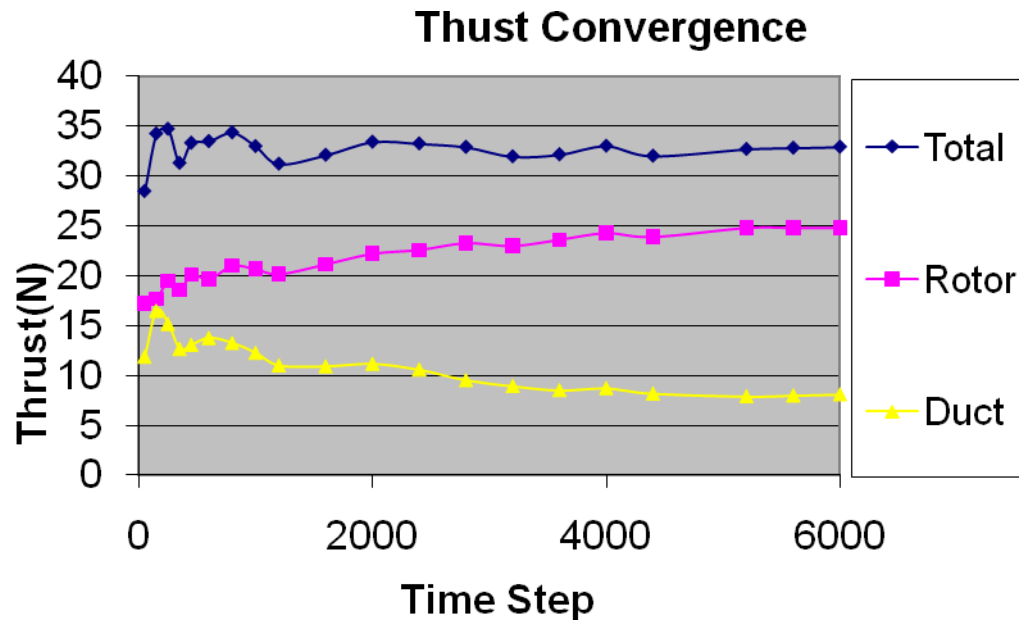


Figure 2.24a: Thrust of Rotor and Duct (Time Step 0-6000)

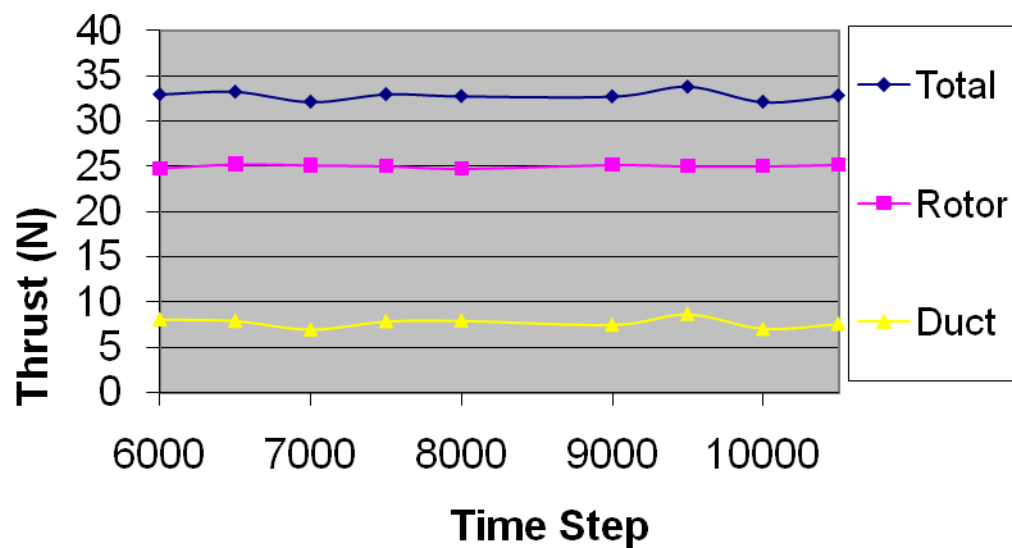


Figure 2.24b: Thrust of Rotor and Duct (Time Step 6000-10500)

The start up transients in figure 2.24a were very strong but dissipated by approximately the 10th Revolution. Although the duct thrust was not constant, it was determined that the 10500th time step was a fair representation of the average thrust and was used for loading and acoustic calculations.

The thrust coefficient was calculated to be 0.32. Again, the rotor was rotated faster than design for the purpose of acoustics analysis but the experimental team did not test at this speed. Using the experimental data from lower tip speeds, it was determined that the experimental value of the thrust coefficient converged to approximately 0.35 [18]. Note that the thrust coefficient was calculated using the total thrust (duct thrust + rotor thrust).

2.2.2 Open Rotor

A case without the duct (figure 2.25) was run to compare both the aerodynamics and acoustics to a ducted case. The geometry of the rotor and domain and domain subdivision were exactly the same as the ducted case to ensure numerical consistency. Again, the simulation was run until the wake developed and the rotor thrust no longer varied with time.

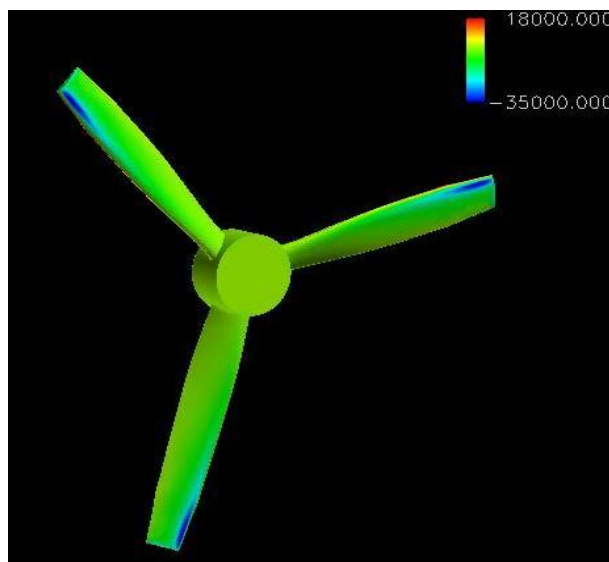


Figure 2.25: Isolated Rotor Pressure (p' , Pa)

The overall contour patterns are similar for the ducted rotor. The exact pressure distribution will be examined more closely in section 2.2.3.

The startup wake for the open rotor case was similar to figure 2.13 and developed (figure 2.26) to a well formed wake such as in figure 2.15.

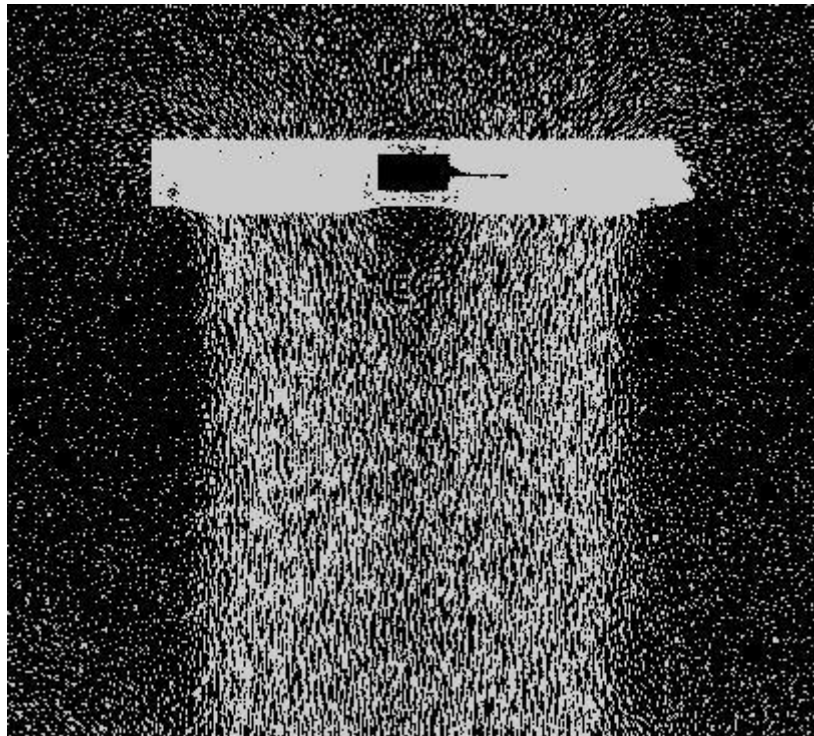


Figure 2.26: Open Rotor Developed Wake Profile

Air flowing through the open rotor in figure 2.26 contracted fairly well into a well formed slipstream. The white box where the rotor passes through is due to the denser mesh used around the rotor. It is merely many vectors in a small area that all blend together in figure 2.26. The wake contraction parameter was calculated in the same manner as the ducted rotor (figure 2.22). A cut in the far wake was made and the area was calculated at several locations to ensure that the wake was not contracting anymore (figure 2.27).

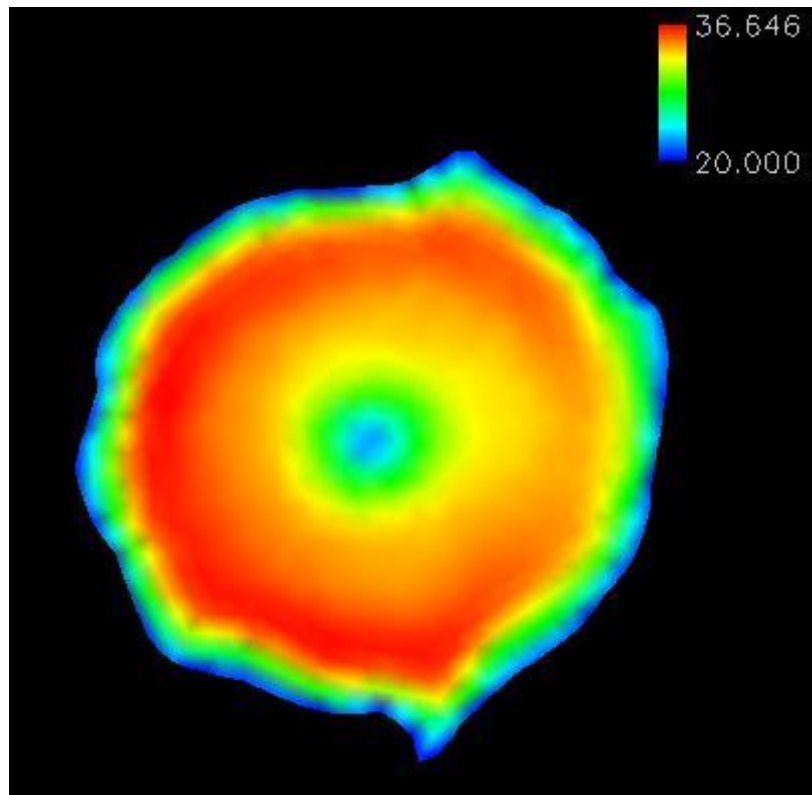


Figure 2.27: Open Rotor Far Wake (v, m/s)

The wake contraction parameter for the open rotor was calculated to be 0.59 which is very close to the typical value of 0.61[1] for a compressible turbulent case. Note that the velocity ranges will be different from the ducted rotor case. This is due to the higher induced velocity for the ducted rotor. The induced velocity for the ducted rotor (shown in figure 2.23) was averaged to determine an average induced velocity of 25.34 m/s. This is somewhat higher than the theoretical value of 22.5 m/s which was calculated using the total thrust and a_w value calculated for the ducted rotor and equation 1.12. Figure 2.28 represents the near field velocity of the open rotor and the average induced velocity was calculated to be 23.16 m/s which is also higher than predictions based on the calculated parameters (18.31 m/s). This indicates a higher induced velocity by the ducted rotor which is consistent with momentum theory. From equation 1.12, the induced velocity is directly dependent on the total thrust and the wake contraction parameter. The results indicate that the total thrust (figure 2.24, 2.29) and wake contraction parameter

(figure 2.22, 2.27) are both smaller for the open rotor which leads to a lower induced velocity. Note that the near field cutting plan was located 0.01m (0.1R) downstream of the rotor for both the ducted and open rotor case.

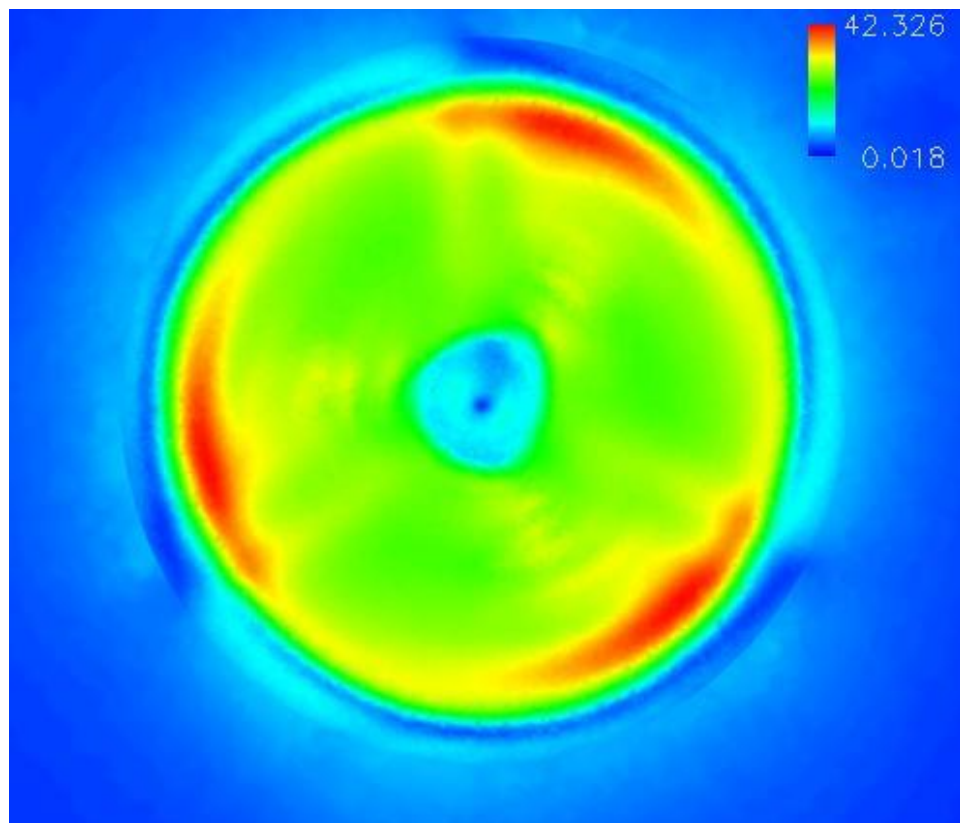


Figure 2.28: Open Rotor Near Wake (v, m/s)

A converged thrust was reached more quickly for the open rotor (figure 2.29) because of the absence of the duct which caused instability in the thrust (figure 2.24b). The instability was caused by flow separation from the duct wall (figure 2.19) and recirculation in the downstream half of the duct (figure 2.20). The duct thrust could vary by as much as 10% from the mean in the final two revolutions.

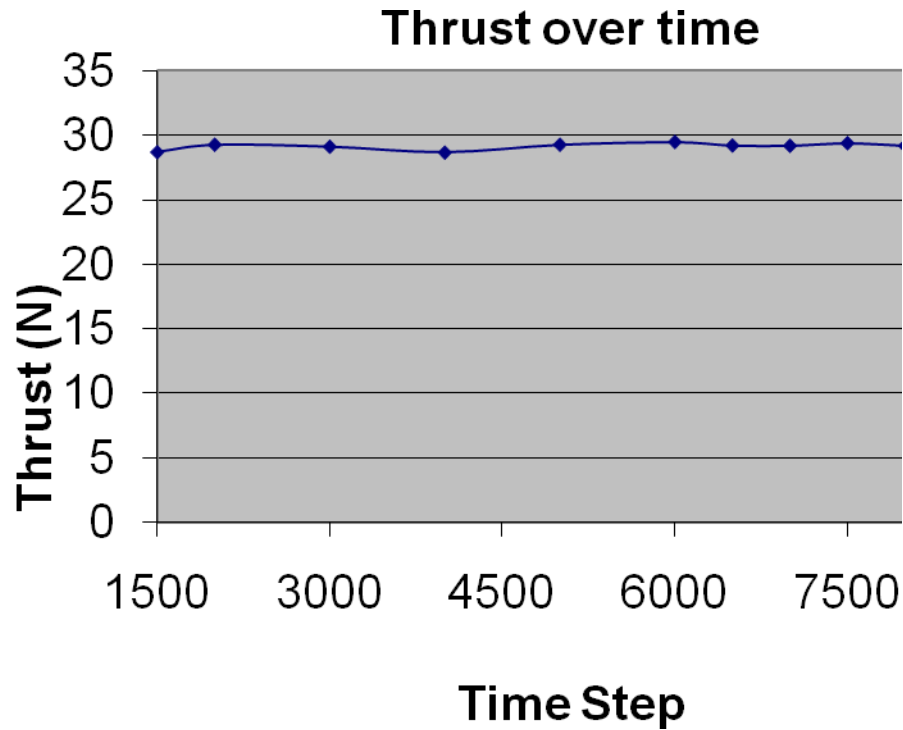


Figure 2.29: Open Rotor Thrust Over Time

Any fluctuations late in the simulation were by less than 1% of the average thrust of 29.49N. Overall, the rotor thrust converged very well. The rotor thrust of the ducted rotor also varied by less than 1% of the average (25.19N) (figure 2.24b).

2.3 Comparison of loading

One influence that a duct has on a rotor is shifting the load balance from the rotor and the rotor and duct together [1, 2]. It is expected that there will be less loading near the tip of the unducted rotor and less tip loss for the ducted rotor case. This can be shown qualitatively in figure 2.30.

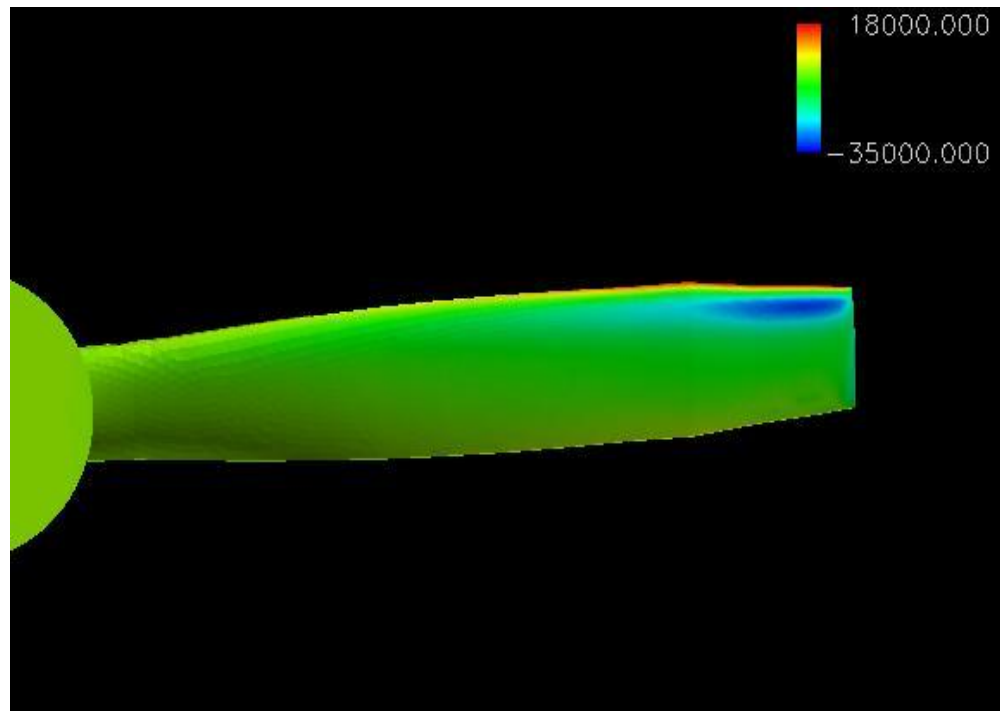


Figure 2.30a: Ducted Rotor Blade Pressure Distribution (p' , Pa)

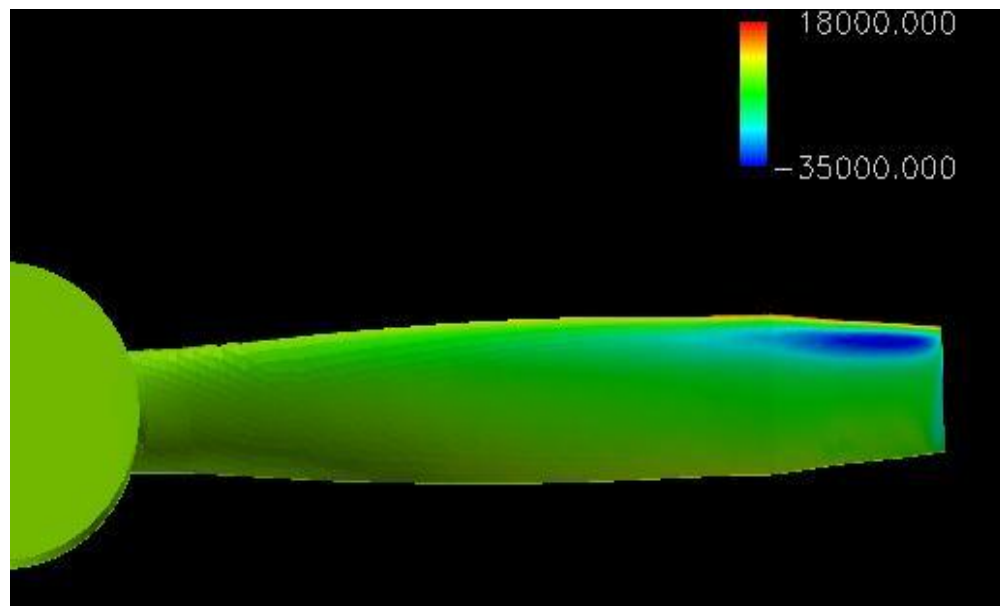


Figure 2.30b: Open Rotor Blade Pressure Distribution (p' , Pa)

The low pressure region is much larger for the open rotor. To be more quantitative, the spanwise loading was calculated by integrating thin sections of the rotor along the span (figure 2.31).

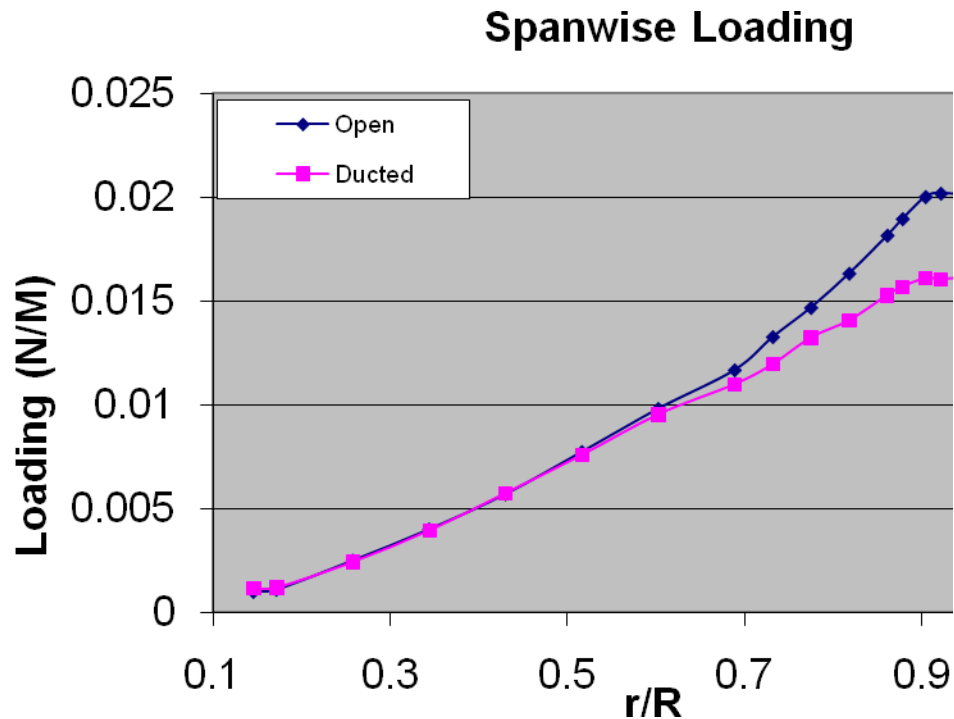


Figure 2.31: Spanwise Loading Comparison

The loading is nearly identical near the root in figure 2.31 but the total loading (area under the curves) is less than the ducted rotor. This is related to the fact that the duct is also producing thrust. There is less reduction in the spanwise loading near the tip in the ducted rotor case. There is a spike near the tip that seems to be due to a low pressure area forming along the tip (figure 2.32). The low pressure area is along the tip just after the main low pressure area begins to decline. Despite the low pressure area not being as intense as the main area, it covers a much larger area of the chord which would explain the thrust jump. The cause of the low pressure area is due to the tip vortex shown in figure 2.19 and figure 2.26.

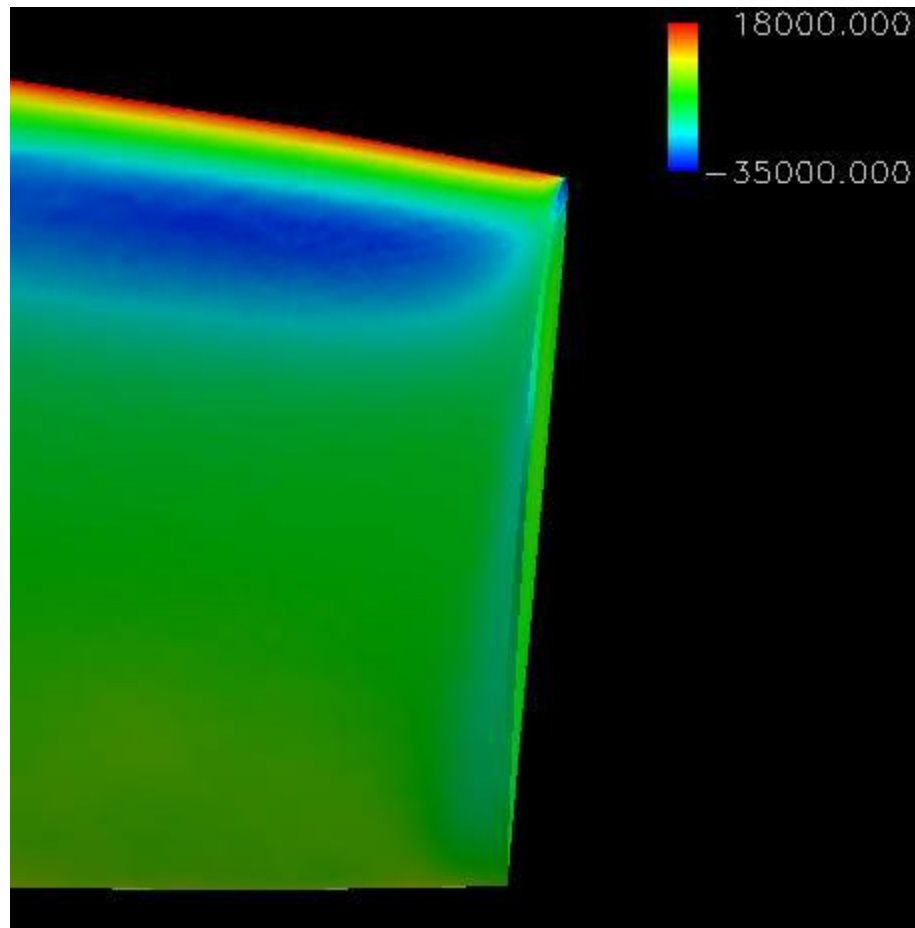


Figure 2.32: Pressure Along the Rotor Blade Tip (p' , Pa)

2.4 Comparison with Momentum Theory

The ducted rotor is expected to perform better in terms of thrust and/or power [1, 6]. Which performance parameter(s) increase is dependent on the variables that are held constant. Figure 1.2 – 1.4 examine performance increases if the total thrust (figure 1.2), power (figure 1.3), or thrust of the rotor (figure 1.4) is constant. In the case presented, it is the RPM of the rotor that is fixed because it could be directly controlled. Table 2.1 is a summary of the recorded data used to assess the performance increase of the ducted rotor over the open rotor.

	Thrust (N)	Torque (N*M)	a_w
Ducted	32.77	0.502	0.8
Open Rotor	29.49	0.517	0.59

Table 2.1: Momentum Theory Parameters

The open rotor thrust converged to 29.49N which is somewhat higher than the rotor thrust of the ducted rotor (25.19N) but less than the total ducted rotor thrust (32.77N). Momentum theory predicts that the thrust of an open rotor should be somewhere between the rotor thrust of a ducted rotor and the total thrust of a ducted rotor assuming the same or at least nearly same power input. The difference in torque of the open rotor is about 3% higher than the ducted case and since the rotation rates are the same, the power difference will also be 3%. This means that it is reasonable that the open rotor falls within the range of the ducted rotor total thrust and the thrust of the rotor itself.

The power, thrust, and wake contraction of each case can be related by the following.

$$\frac{P_{ducted}}{P_{open}} = \left(\frac{T_{ducted}}{T_{open}} \right)^{3/2} \sqrt{\frac{a_{wopen}}{a_{wducted}}} \quad (2.1)$$

The ratio of the power is directly related to the torque caused by the drag on the rotors. The parameters for this equation are in the following table. Solving this equation for $a_{wducted}$, it is predicted to be 0.9 which is between the measured and expected values. As a reminder, it is expected that the wake contraction parameter of a ducted tail rotor should be at least 1. It is not unexpected that the measured parameters cannot satisfy momentum theory perfectly because of the vortices, viscous, and compressible flow but it still provides insight into the ranges of wake contraction, thrust, and power which can be expected.

Overall, the duct provided better performance than the open rotor. A total thrust increase of 10% was measured with a 3% decrease in power. It is also interesting to note that the thrust contributed by the rotor alone was nearly 15% less in the ducted rotor case. It is important to note that the ducted rotor was very inefficient in this simulation so the performance increase is not optimal. As a reminder, the rotor was not designed to be in a ducted rotor and was rotated with a higher tip Mach number than design, which is why inefficiencies (such as duct flow separation) occurred.

Chapter 3

Acoustics

This chapter will highlight the approaches taken to understand the acoustics of ducted rotors. First, the methods that required less computation time will be explored. These methods use an incident field based on blade loading calculated by a blade element theory (BET) code. The scattered part of the total sound field will be calculated using the FSC. Since the BET and FSC codes ran very quickly, many different duct configuration could be examined. The BET code generated the geometry which PSU-WOPWOP used to predict the incident thickness field. Note that only the thickness noise was used for the FSC results because changing the duct geometry would also change the loading on the rotor as seen in chapter 2. Since the thickness noise will not change due to the presence of a duct, the scattering of thickness noise was examined as a first step in the analysis of the scattered acoustic field. The incident field was in turn used by the FSC to compute the scattered field. The scattering due to the duct will be examined for different duct thicknesses and lengths. It is important to note that the geometry used for the FSC results differs from the geometry seen in chapter 2. The results of FSC were computed before the test subject became available and were meant to represent a generic ducted rotor.

Later in the chapter, the noise will be calculated using the three dimensional CFD computations from chapter 2 as input to PSU-WOPWOP. Both the incident noise produced by the rotor, and the scattering from the duct will be calculated by PSU-WOPWOP in those cases. Because of the computation time and resources required to run a ducted CFD case to convergence was substantial, only one rotor and test condition was examined. Since the CFD takes into account the loading changes on the rotor surface, the loading noise is included for these noise calculations.

The data for the duct and the rotor can be stored separately; hence, the noise contribution to the total acoustic field from each source can be examined independently. Throughout this chapter, there will be 4 common configurations to be examined in the acoustic calculations: 1) rotor and duct together (usually referred to as the “Total”); 2) the rotor alone (but using the rotor loading data from the CFD computations that includes the

duct); 3) duct alone; 4) the open rotor (using the rotor CFD computation without the duct).

3.1 FSC Predictions

In order gain an understanding of scattering and the impact that duct geometry has on noise magnitude and directivity, several test cases were run. The rotor used in the following test cases was a 6 bladed 0.55m radius rotor whose blade cross sections were an NACA 2412 airfoil with a chord length of 0.078m. The rotor rotation rate was 491.44 rad/s with standard sea level environmental conditions. Several different duct configurations were used. The duct was generated using a symmetric airfoil offset by the rotor radius and sweeping it around the duct axis. The cross section of the duct is either a NACA 0024 or NACA 0048 airfoil. These two airfoils were used to examine the impact of duct thickness on the total sound field. Different lengths for the duct were also used to examine the effect of the duct length on the sound field. The baseline duct (figure 3.1) used the NACA 0024 cross-section and was 1.1m long (one rotor diameter). The wireframe plot of the duct was stored in plot3D format and was used to generate the collocation points need by the FSC.

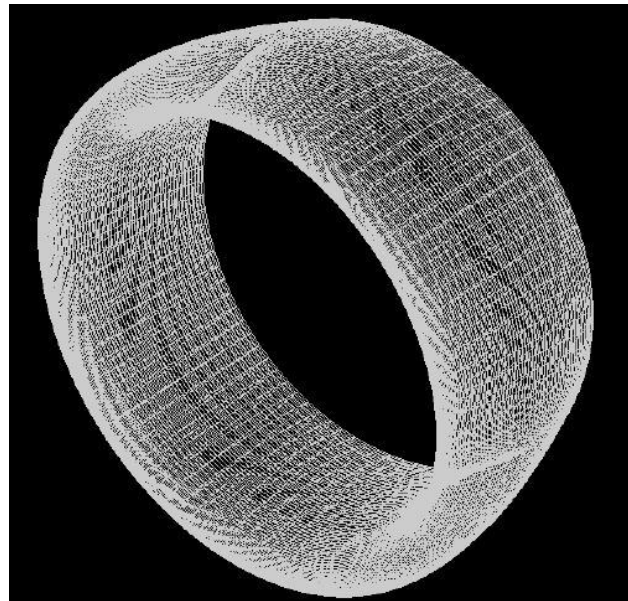


Figure 3.1: FSC Duct Wireframe

The geometry of the rotor and duct were produced using a code written by Dr. Leonard Lopes. The code did not take into account the changes to the lift distribution on the rotor due to the presence of a duct (figure 2.30) so it was decided to only examine the thickness noise of the rotor for the incident field.

The first step required to use the FSC was to obtain the incident field. As a reminder, for the FSC, only the incident field and the geometry of the scattering body is required to be known. The incident field was calculated by inputting the rotor geometry into PSU-WOPWOP and calculating the thickness noise (figure 3.2). The Rotor is centered at $X = 0$ and the flow direction is from left to right (although the FSC does not account for the flow).

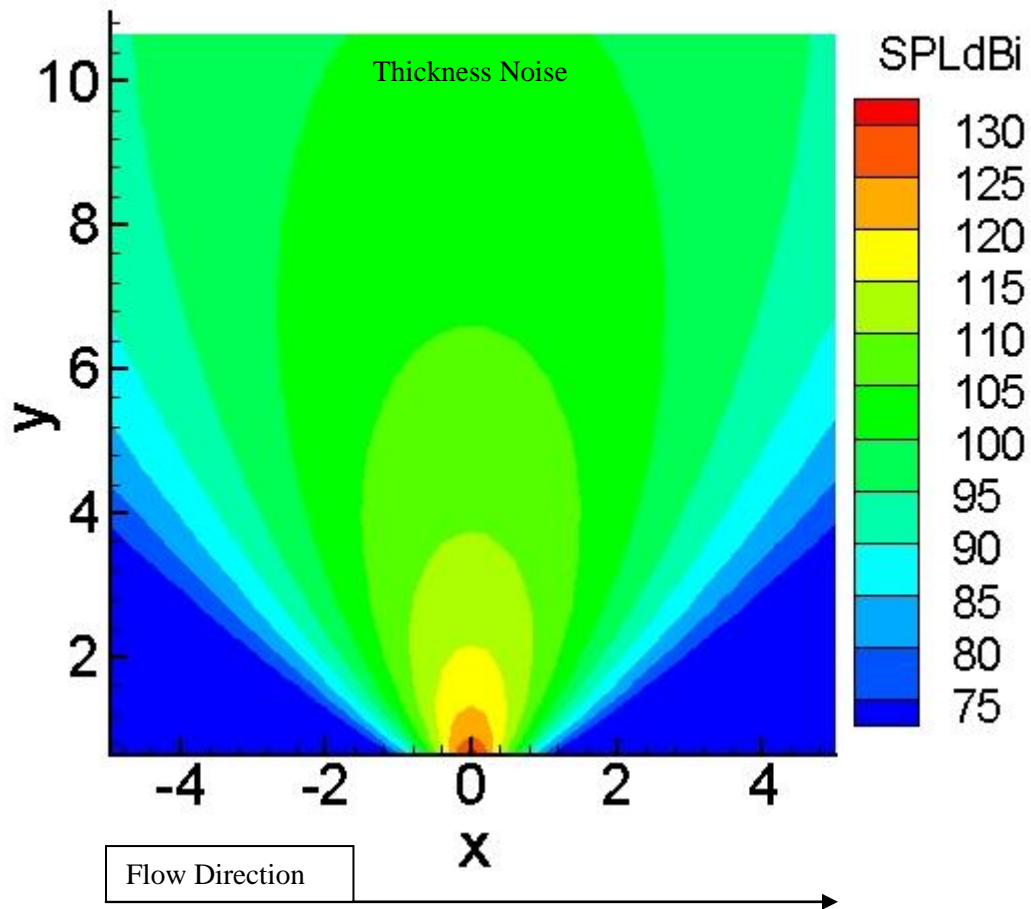


Figure 3.2: Incident Sound Field from the Isolated Rotor

This incident field was then input into the FSC to determine the scattered and total acoustic fields (figure 3.3). Again, the flow is from left to right. The duct is centered at $X = 0$ and the observer grid is placed just above the duct.

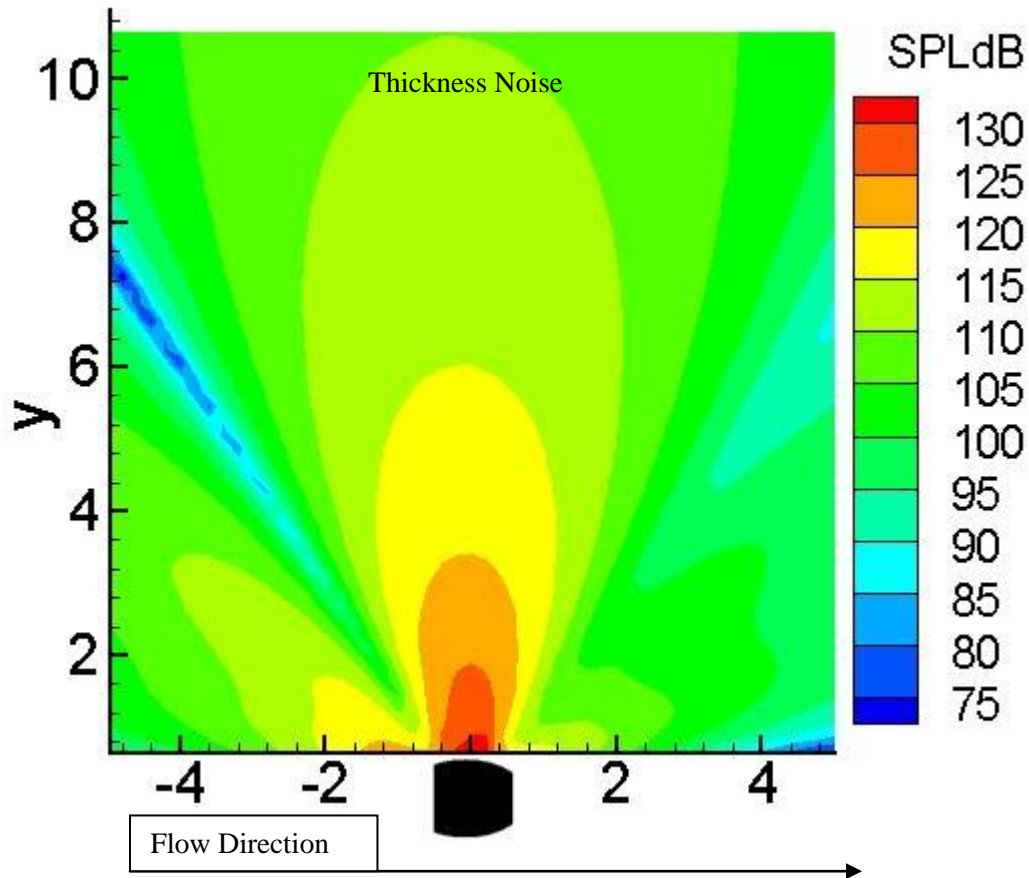


Figure 3.3: Total Sound Field Using the FSC

The directivity of the total acoustic field changed significantly in 5 key locations, which will be compared to the later direct PSU-WOPWOP calculations. These locations are the centerline, the rotor plane, and the regions both upstream and downstream of the rotor. Along the centerline, the total acoustic field is significantly louder than the incident field, particularly upstream. It appears that the duct has a strong influence in redirecting noise along the centerline. It is also significantly louder in the rotor plane, but the results seem suspect. The expectation was that in rotor plane, the noise should be significantly less

due to the shielding effect of the duct. This will be explored deeper in later calculations. Finally, the region that showed significant noise reduction was in between the axis of the duct and to the left of the rotor plane. The incident and scattered signal seem to be out of phase at about 45 degrees from the axis or the rotor and nearly complete cancellation seems to occur.

Duct thickness might be expected to have an important role in the sound field scattering [9]. Furthermore, it is expected that the FSC code should provide more reliable results for a thicker duct. Therefore, the thickness was increased by changing the cross-section of the duct from a NACA 0024 airfoil to an NACA 0048 airfoil. Collocation points were then generated for the thicker duct and its scattered sound field was then calculated using the FSC (figure 3.4). The baseline duct is on the left while the thicker duct is on the right.

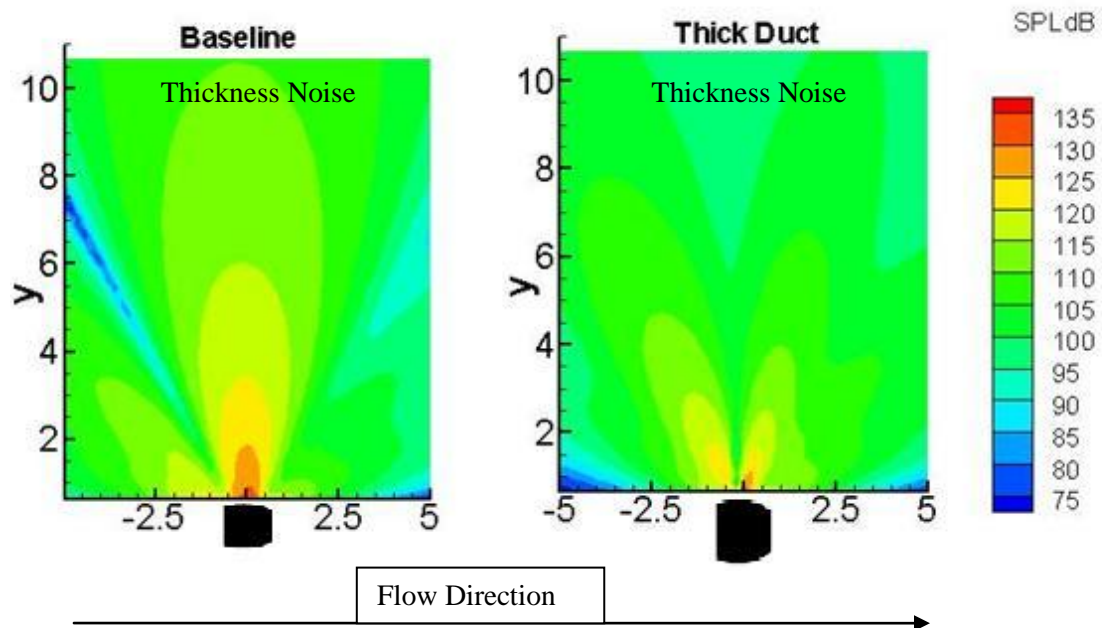


Figure 3.4: Effects of Duct Thickness on Noise Scattering

It appears that the thicker duct blocks more noise in the plane of the rotor. The noise appears to be redirected more out of plane. It is not clear if this is a real effect or a

numerical error in the FSC approach. In fact, this result leads to further suspicion that the baseline FSC result may be incorrect in the plane of the rotor outside the duct.

The effect of the duct length was also examined. The two lengths examined were 1.1m (baseline – one rotor diameter) and 4m (figure 3.5).

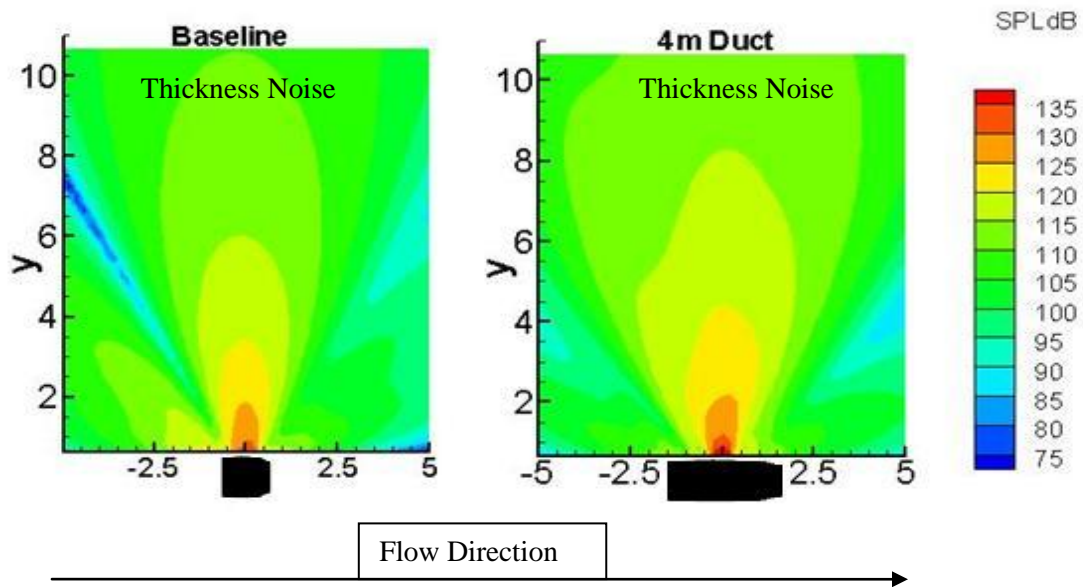


Figure 3.5: Effect of Duct Length on Noise Scattering

To make the changes in the sound field more visible, the difference between the two sound fields was taken (figure 3.6). Positive values indicate the regions where the longer duct is louder.

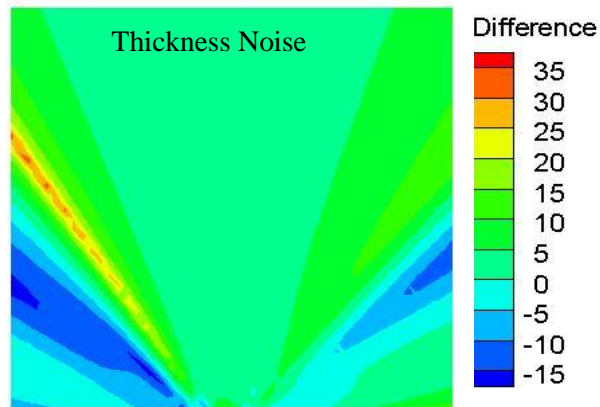


Figure 3.6: Difference in Sound Fields Due to Duct Length Difference (OASPLdB)

Figure 3.6 shows very little change directly in plane of the rotor while out plane is very different. The 4m duct directs more noise at approximately a 45 degree angle upstream and downstream of the rotor. The results of the FSC code seem to be somewhat questionable at times, so their primary use will be to see if the CFD/FW-H approach gives the same general trend. Overall, the FSC results were not trusted and therefore, the method was abandoned in favor of the FW-H approach once the experimental test case became available. Most published ducted rotor scattering data using the FSC used point sources to simulate the rotor. It is possible that the presence of an actual rotor has caused numerical issues in the code.

3.2 Ffowcs Williams-Hawkings Approach

The PSU-WOPWOP code was used to calculate the acoustic field using the steady CFD described in chapter 2. A single time step was chosen to provide the steady surface pressure data on both the rotor blades and the duct. A converter was written (described in Appendix B) to generate separate PSU-WOPWOP input files for both the duct and rotor so that the components of the noise could be examined individually as well as together.

3.2.1 Overall Sound Pressure Level

The first area of interest is the overall sound pressure levels (OASPL) of each case, which is examined in Figure 3.7. Some general trends were observed. First, the total sound field differs from the rotor alone indicating an influence from the duct. Also, the rotor alone (ducted CFD) is nearly identical to the open rotor. This is reasonable since the geometries are exactly the same (Same thickness noise). The loading on both rotors does differ so a magnitude change in the loading noise is expected. While the difference is not large, the open rotor loading noise is slightly higher than the rotor alone (i.e. the rotor noise based on the rotor loading with the duct in place). To illustrate directivity changes, a polar plot of the OASPL was made at a distance of ten times the rotor radius away from the center of the duct (figure 3.8). Similar to the FSC results presented, the flow direction in all figures is left to right.

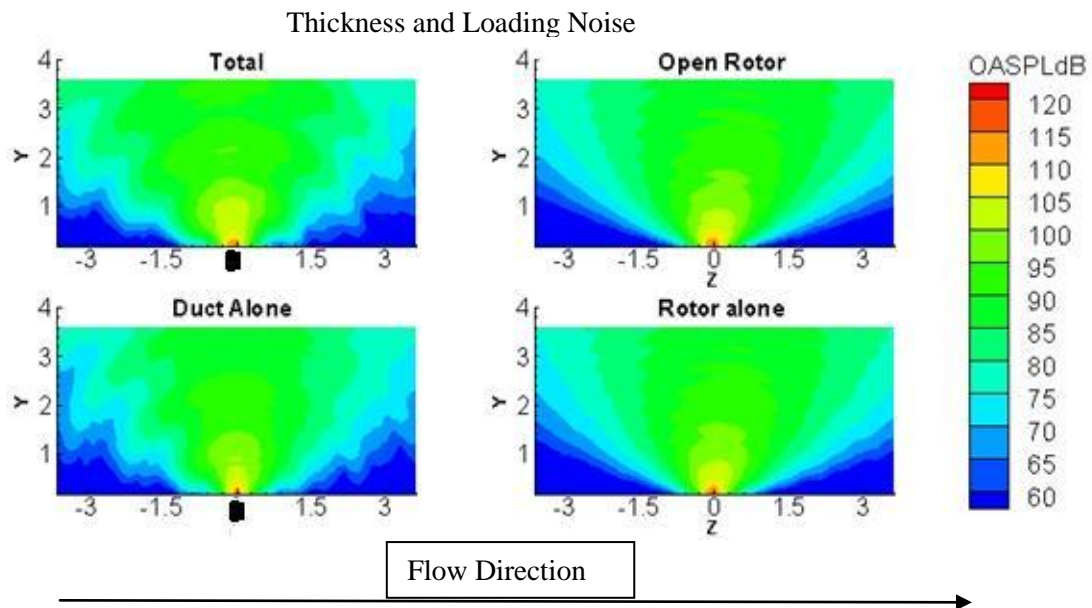


Figure 3.7: OASPL Based on CFD Results

Thickness and Loading Noise

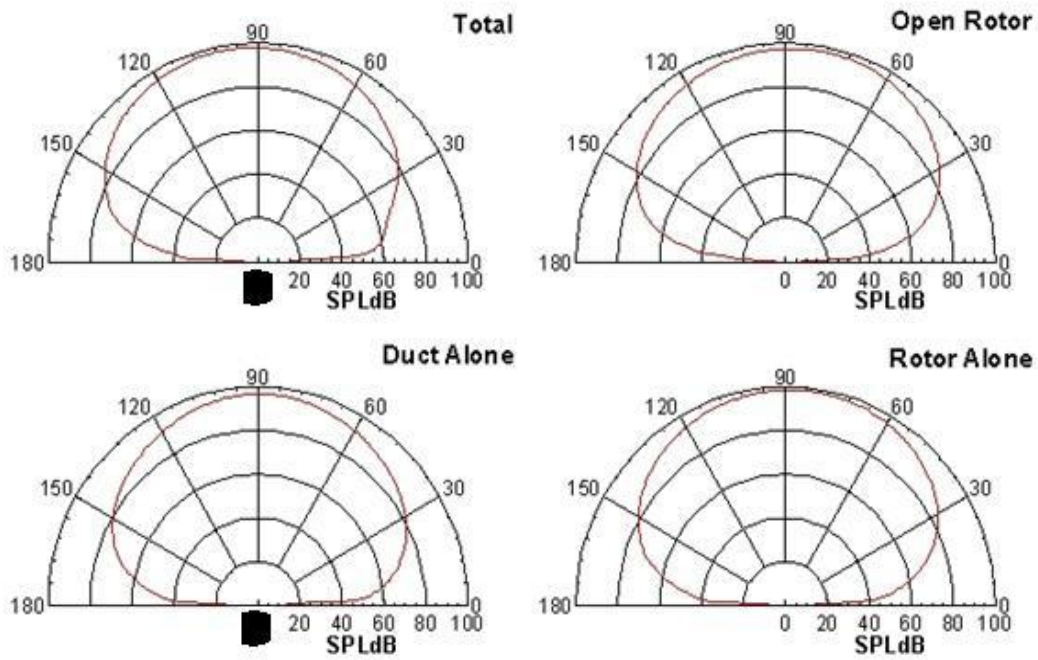


Figure 3.8. OASPL Polar Plots

For clarity, the open rotor and rotor alone plot were overlaid, and the rotor alone plot was overlaid onto the total plot (figure 3.9).

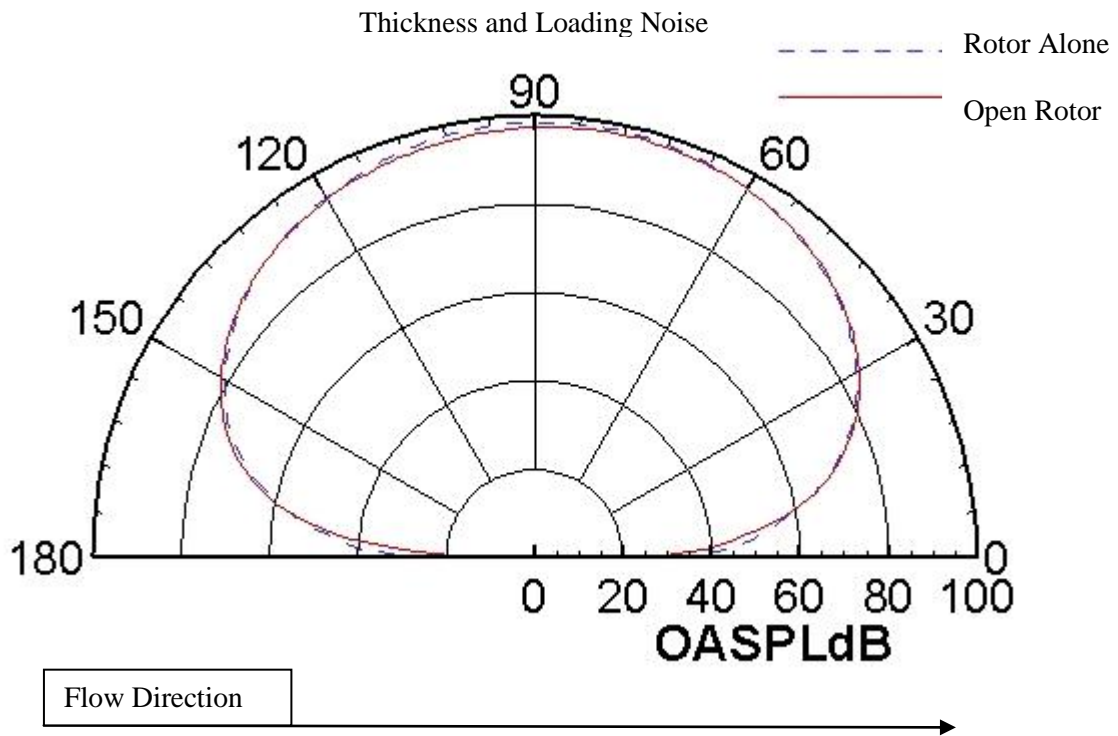


Figure 3.9: Open Directivity vs Rotor Alone Directivity

The rotor alone is nearly identical to the open rotor. The directivity changes are expected because of the differences in loading distributions along the span of the rotor.

The more interesting result is the comparison of the total field and the rotor alone. This provides information about the scattering effect of the duct.

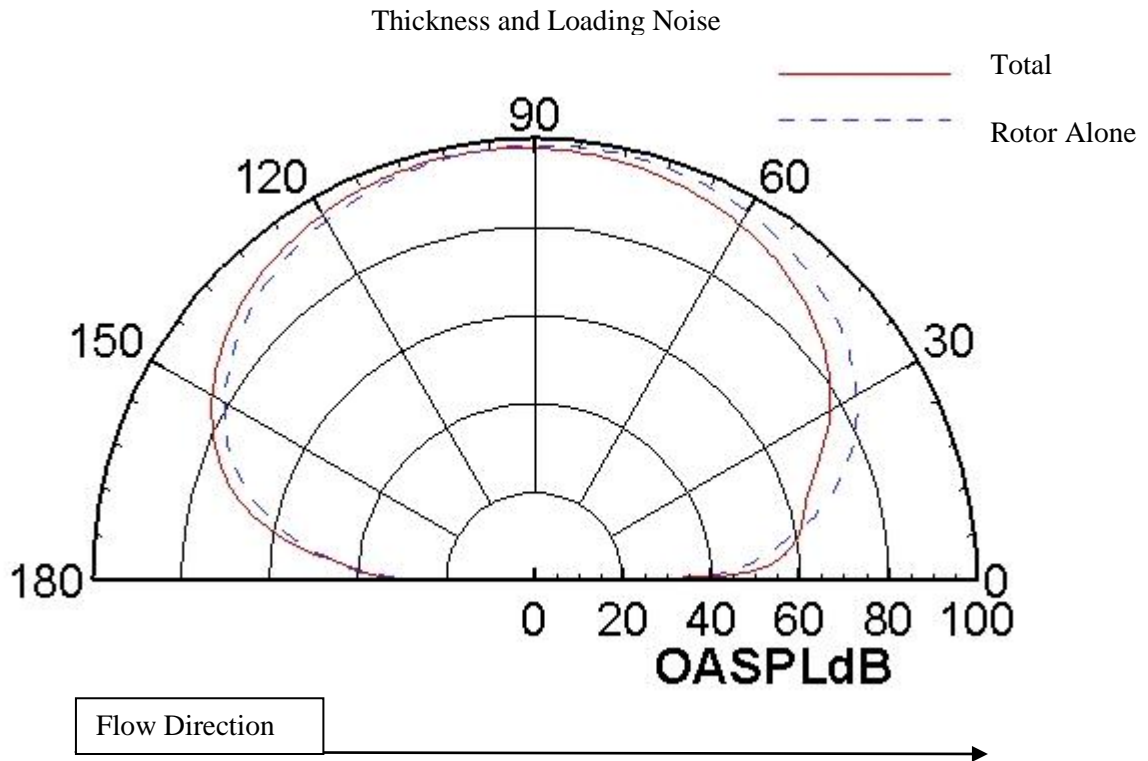


Figure 3.10: Total Directivity vs Rotor Alone Directivity

Much like the FSC results, upstream of the rotor (90 to 180 degrees) is slightly louder due to scattering where at an angle downstream (~10 to 90 degrees), it is much quieter. The total field is also louder along the centerline downstream of the rotor (0 to ~10 degrees). Two features of the FSC results that are not seen is the increase in noise in the rotor plane, and the decrease at an angle upstream. Although the FSC result is suspect, it is also true that the rotor and duct geometries, as well as operating conditions are all different here. Furthermore, the FSC computations only used the thickness noise which is dominant in the plane of the rotor (for an open rotor).

The reason for the sound not decreasing at an angle upstream is likely due to the position of the rotor inside the duct (figure: 3.11, 3.12 white line indicates where the rotor is placed). In the FSC cases, the rotor was centered in the duct (figure 3.11) whereas in the CFD cases; the rotor was closer to the front of the duct (figure 3.12). With the rotor in the center of the duct, two distinct quieter zones were observed. In the results obtained from CFD, upstream is generally louder while downstream was mostly quieter except

along the duct centerline. This may indicate that the downstream is being shielded much more with the rotor closer to the front of the duct.

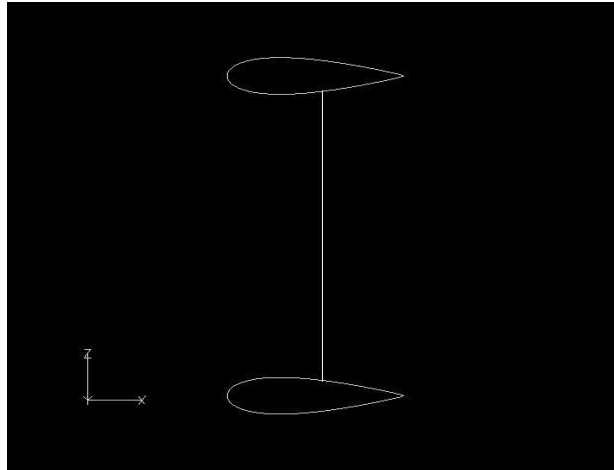


Figure: 3.11: FSC Rotor Placement

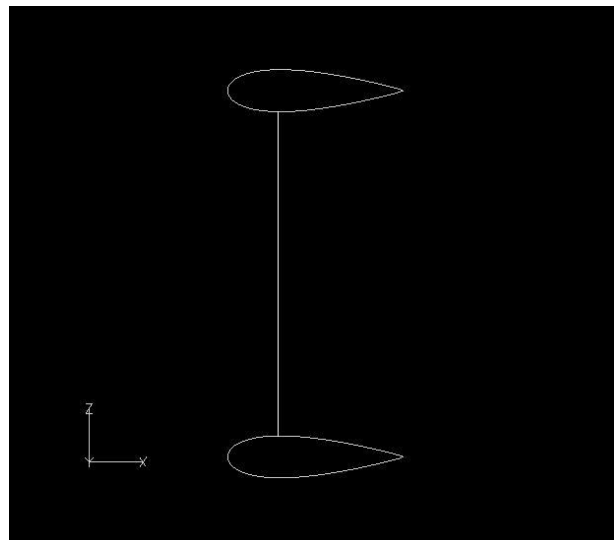


Figure 3.12: CFD Rotor Placement

It is interesting to note that there are local sound reductions and the sound increases are not significantly higher despite the 10% increase in total thrust. It is also important to note that the ducted noise may be locally higher in the cases presented because the overall thrust is higher, indicating that there will be more overall loading. As

a reminder, the increase of thrust is due to the presence of the duct, which has a significant amount of loading on it. It was shown that duct geometry has a large impact on the scattered field, but it is also important to remember the duct's impact on the incident field as well. Recall that the presence of a shroud decreased the loading on the rotor blades by 15% (figure 2.31) in the computation. This drop decreases the levels in the incident field.

The experimental team also measured the directivity difference between the open rotor and ducted rotor using microphones placed in several different azimuthal locations (figure 3.13)

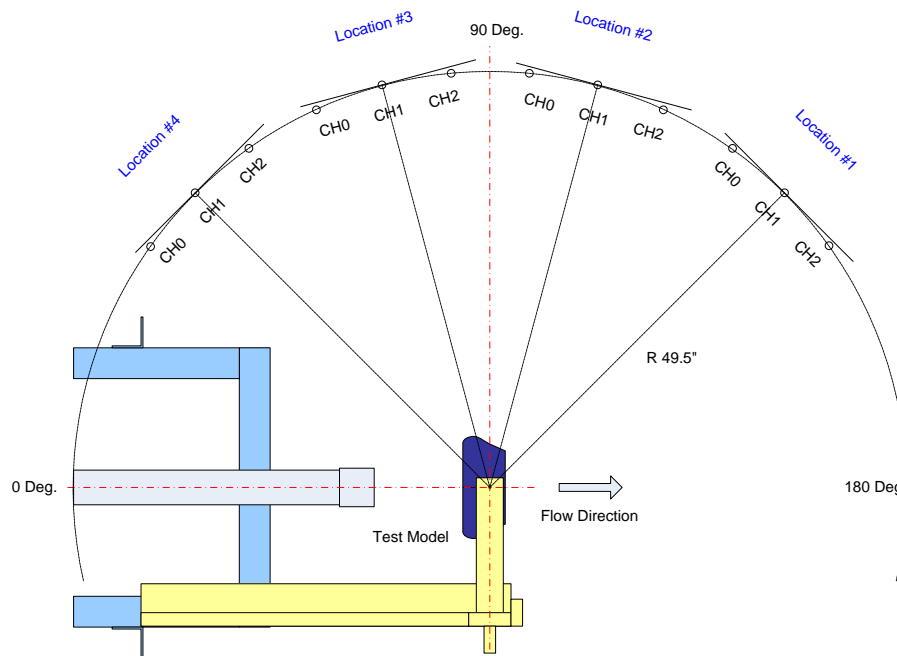


Figure 3.13: Azimuthal Locations of Microphones [19]

The experimental team tested at several different rpms (figure 3.14). The duct had a significant impact on the scattering of the sound. Although a higher sound level was measured at each location, it was found that the least amount of increase is observed downstream out of plane. Clearly, this region is being shielded the most by the duct. The higher levels in most regions are likely caused by the increased total thrust of the system due to the presence of the duct. Note that some of the comparison between the

experimental data and simulations is complicated because the rotor is rotating much faster in the simulations causing a much higher thrust.

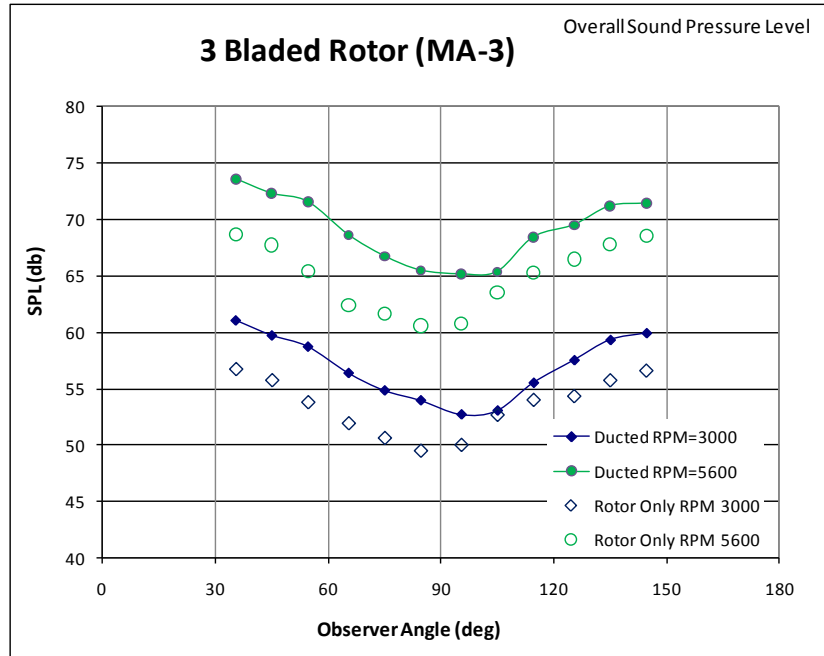


Figure 3.14a: Experimental Directivity Results [19]

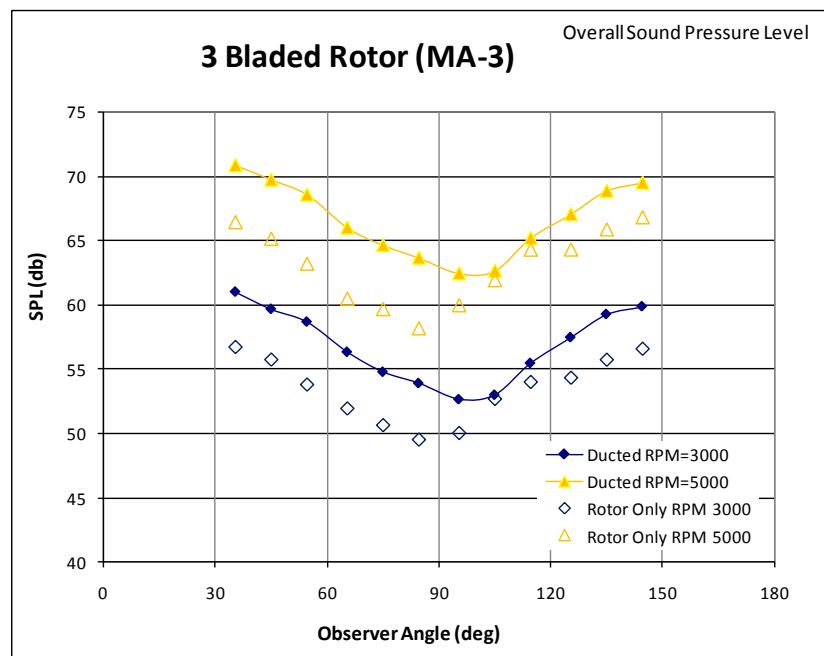


Figure 3.14b: Experimental Directivity Results [19]

3.2.2 Sound Harmonics

Equally as important as how the sound field behaves in an overall sense is how each harmonic behaves with and without the presence of a duct. It is expected that the duct will not have much impact at lower harmonics because at lower frequencies, the wavelength is on the order of the length of the duct. The first 5 harmonics were calculated. Note that the following sound fields were calculated using the loading data from the CFD.

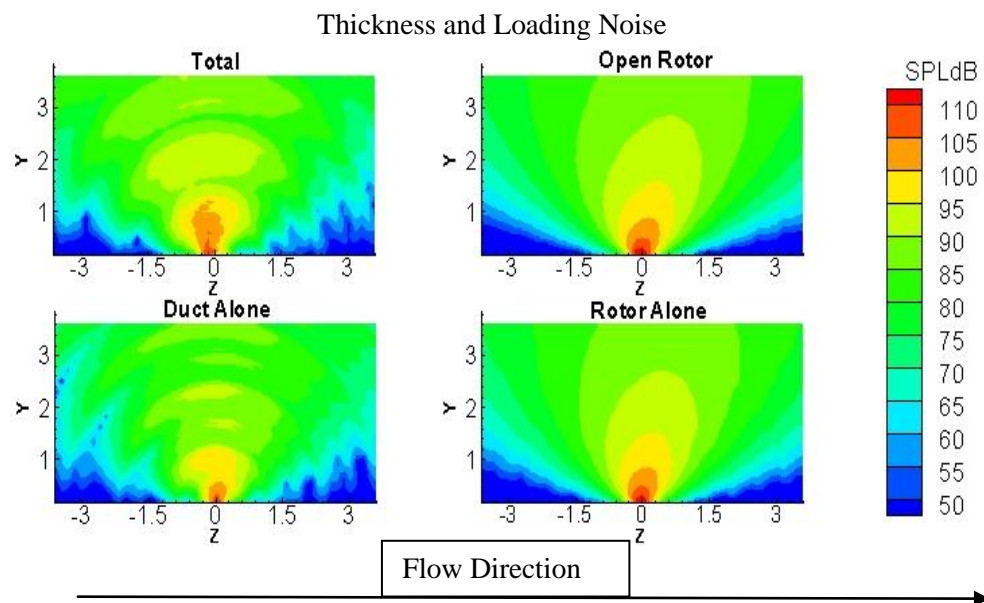


Figure 3.15a: 1st Harmonic

Despite the wavelength being several times the duct length ($\lambda/L = 3.78$), some scattering was still observed although the noise level is dominated by the incident field. A similar trend is observed through the first few harmonics.

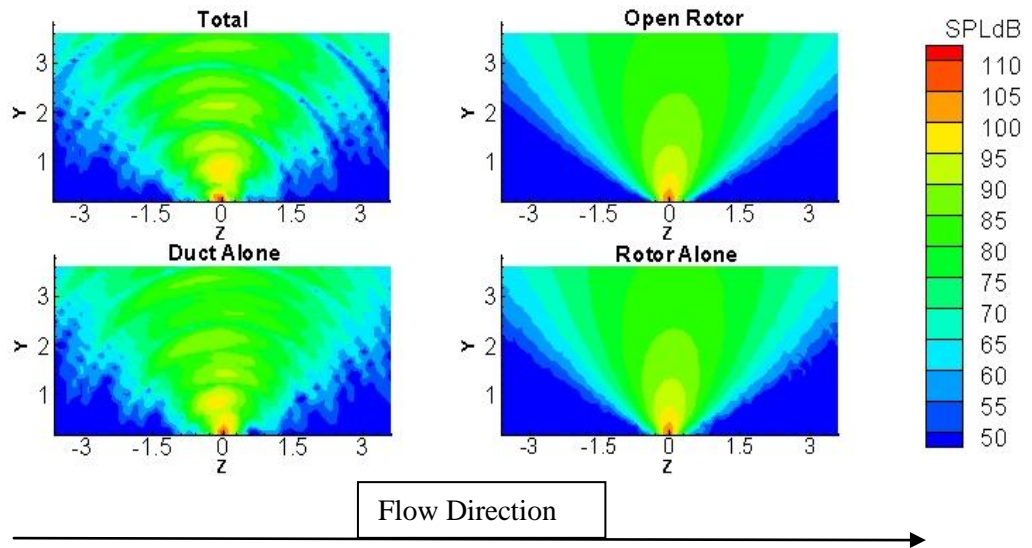


Figure 3.15b: 2nd Harmonic

Similar to the 1st harmonic, the total field behaves much like the duct in terms of directivity. The open rotor remains very similar the rotor alone. Here, $\lambda/L = 1.9$,

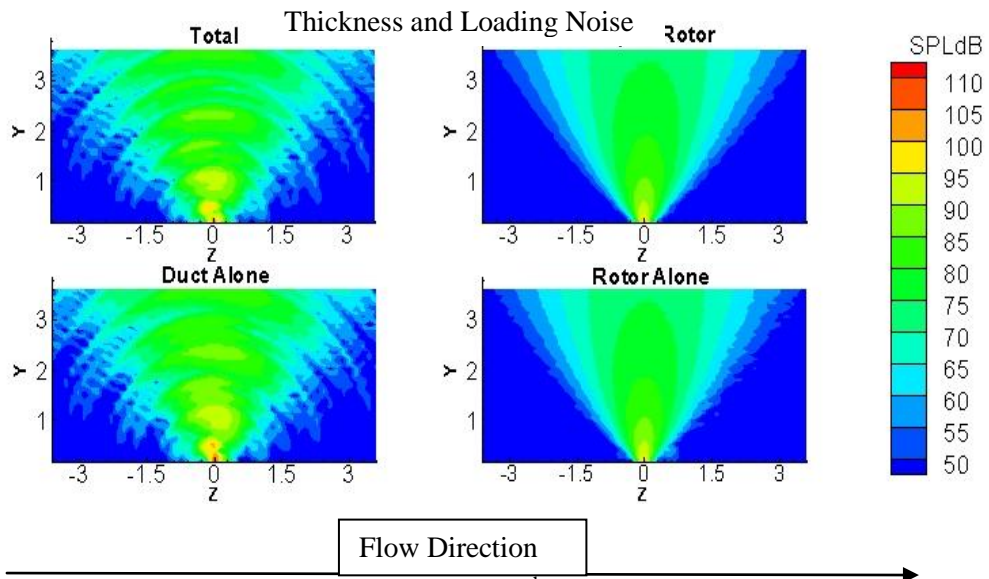


Figure 3.15c: 3rd Harmonic

By the 3rd harmonic, the magnitude of the noise from the duct begins to gain strength. In this cases $\lambda/L = 1.26$

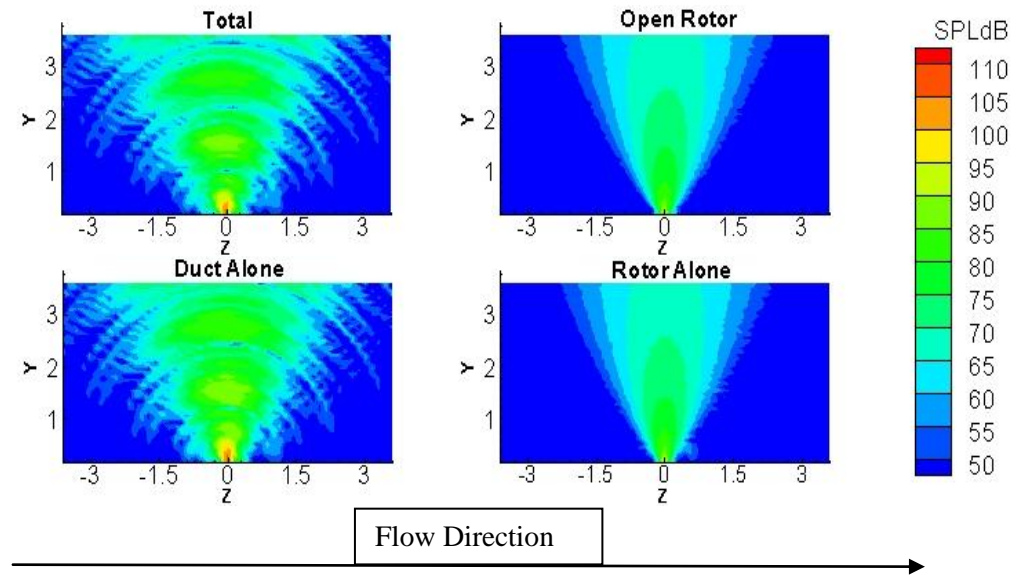


Figure 3.15d: 4th Harmonic

At the 4th harmonic, the noise level due to the duct begins to surpass the rotor noise levels. $\lambda/L = 0.945$ for the 4th harmonic. This change is thought to be due to the fact that the wavelength of the 4th harmonic is now less than the duct length.

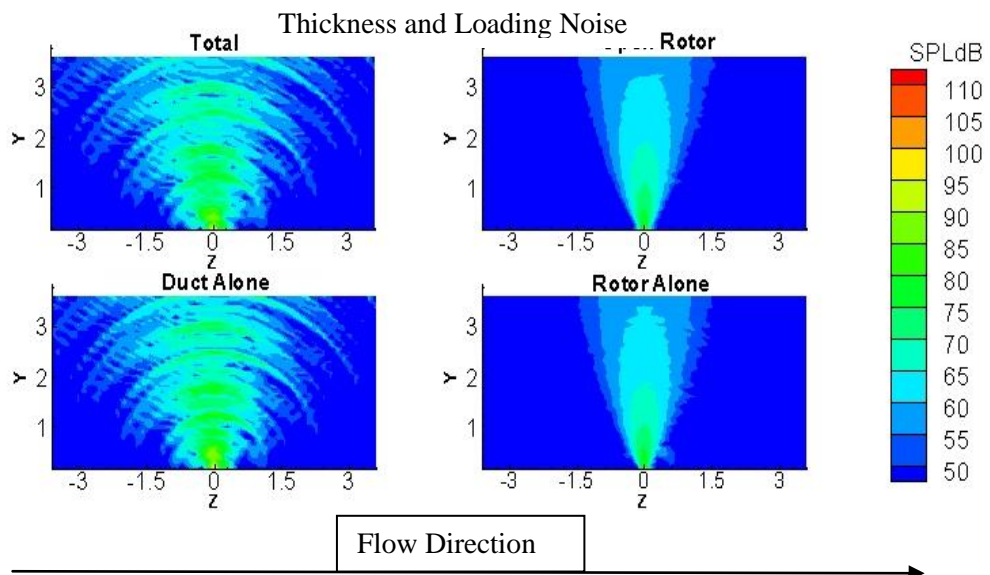


Figure 3.15e: 5th Harmonic

By the 5th harmonic, the noise in both directivity and magnitude begins to be dominated by the duct. This is due to the shorter wavelength ($\lambda/L = 0.756$) and highly unsteady loading on the duct surface.

The experimental team also measured the noise of both the open rotor and ducted rotor over a frequency spectrum (figure 3.16). It is important to remember that the loading on the rotor will be different for the isolated rotor and ducted case. This will cause some difference in the loading noise.

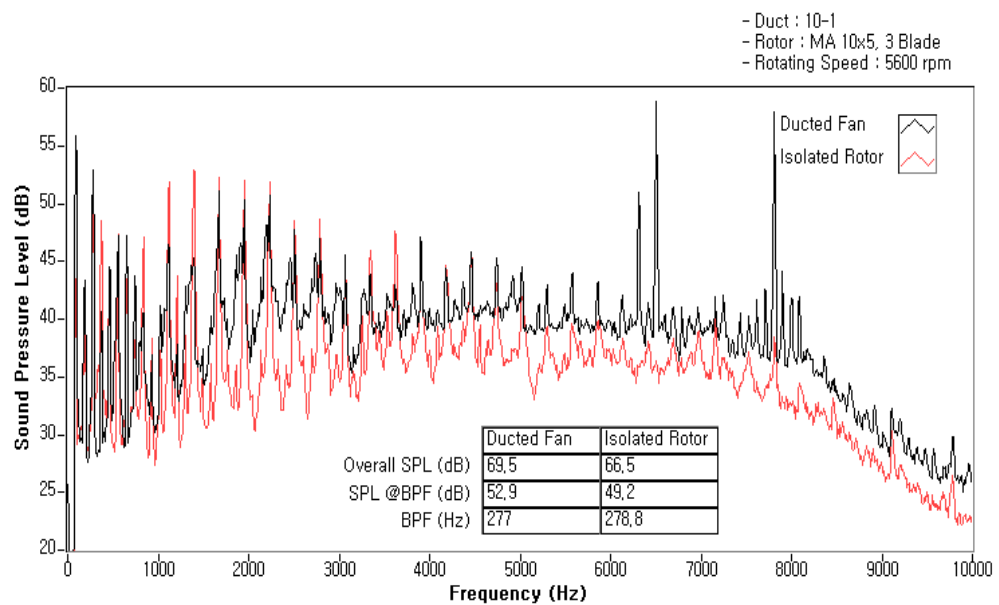


Figure 3.16: Frequency Spectrum Measure for Open and Ducted Rotor [19]

Similar to the calculated results of figure 3.15, the ducted rotor is much louder at higher harmonics due to the duct. It was shown in figure 3.15d that the duct dominated the sound field at the 4th harmonic which was 3357hz. The experimental results also show the ducted rotor noise exceeding the open rotor at approximately that same frequency. The frequency is significant because it is where the wavelength of the sound falls below the length of the duct. Note that the experimental rotor will have many more harmonics than the results shown in figure 3.15. This is because the calculated results used a rotor spun at a higher rotation rate as stated previously.

Chapter 4

Conclusions

4.1 Summary of Research

This dissertation describes two approaches attempted to calculating the total noise field from a ducted rotor. Both the incident and scattered portion of the total field were approached in more than one way. The incident field was calculated using both a blade-element code and directly from CFD. Some two dimensional, axisymmetric CFD work was conducted in order to gain an understanding of the expected flow characteristics of a ducted rotor. The blade-element-theory code, despite being much faster, was unable to replicate the differences in loading distribution along the blade due to the duct (figure 2.30). The loading distribution was much better when simulated using CFD although it came at the cost of significantly more computational time. The scattered portion of the sound field was also calculated using two different methods. The first method was the equivalent source method, where the incident field was computed on the duct wall, and then from this, the strength of the equivalent sources along the duct was determined so that the scattered field could be determined. NASA's FSC was used to calculate the scattering using the ESM. This code was relatively fast; however, the accuracy of the results remains uncertain. The second method was to calculate the scattered field by using the FW-H approach. This was carried out by directly inputting the CFD data into PSU-WOPWOP which is a new application of the code.

4.2 Summary and Conclusions of Aerodynamics

Although this dissertation was intended to be primarily about different approaches to the acoustics prediction of ducted tail rotor noise, obtaining accurate CFD was critical in obtaining accurate noise results. Two-dimensional, axisymmetric CFD was computed to gain an understanding of the effects of the duct on the overall aerodynamics of the ducted rotor. The expansion of the wake was compared to momentum theory and had the same general trend (figure 2.5). It was shown that expanding the diffuser angle on the

duct increased the downstream wake area as well as the thrust of the duct. It is important to note that for the two dimensional cases that the thrust of the rotor is fixed because only the pressure change over the rotor could be directly controlled. For the 3-D cases, the RPM of the rotor is fixed because the rotor blades are modeled directly rather than by a pressure jump.

Three-dimensional cases consisted of a ducted and open rotor with an identical rotors. The rotor wake, thrust, and spanwise loading were all recorded for analysis. The rotor wake is important to compare with the momentum theory analysis. The open rotor was found to have an a_w value of 0.59 which is very close to the typical value of 0.61. This does differ from the momentum theory predictions of 0.5 but that is expected because viscosity and turbulence are accounted for in the simulation.

The ducted rotor was expected to have an a_w value of 1 based on the 2D simulations (figure 2.3) and a value of 0.9 based on the thrust and momentum theory (equation 1.3). The recorded value was 0.8 which was lower than expected. It is believed this is due to flow separation from the duct wall causing the flow to contract more (Figure 2.18-2.20).

The ducted rotor is also expected to produce a higher induced velocity. This was shown in figure 2.23 (Ducted Rotor) and 2.28 (Open Rotor). The induced velocity of the ducted rotor was calculated to be 25.34 m/s which is higher than the induced velocity of the open rotor which was determined to be 23.32 m/s. Both the induced velocity of the ducted rotor and open rotor were higher than predicted by theory.

Thrust produced by both cases is a great area of importance for analyzing the performance increase of ducted tail rotors. From table 2.1, the thrust of the ducted rotor is 32.77N which is higher than the open rotor thrust of 29.49N. Another key factor is the torque on the ducted rotor is about 3% lower than the open rotor leading to a much better thrust to power ratio for the ducted rotor over the open rotor.

The last major change expected for a ducted rotor is that the loading distribution along the span of the rotor will change. This is due to the inflow change near the tip of the rotor, which results in a different thrust distribution near the tip. This is shown in figure 3.28. The thrust is the same near the root where the flow is least affected. Out

toward the tip, the thrust is reduced for the ducted case. This is a direct result of the close proximity of the duct wall to the tip of the rotor. Not only was the distribution different, the total thrust produced by the rotor was lower than the open rotor (table 2.1).

Overall, the aerodynamic results were consistent with momentum theory. The expected differences between the ducted rotor's and open rotor's wake area, induced velocity, thrust, and loading distribution compared well with the expectations from momentum theory in a general sense. The values themselves did deviate from momentum theory predictions because of the losses from compressibility, viscosity, and vorticity.

4.3 Summary and Conclusions of Acoustics

The first approach to calculating the scattered sound field was using the FSC, which is based on the Equivalent Source Method (ESM). The advantage to the FSC was speed of execution and only the incident sound field needed to be known. For that reason, ducts of different geometries could be analyzed without recalculating the incident sound field. It was shown that the duct can influence the loading on the rotor blades and, therefore, the loading noise of the incident field so only the thickness noise was considered for the first set of analysis. Ducts of different lengths and thicknesses were examined using an incident field based on a rotor calculated using a BET code. It is important to note that the rotor geometry used in the FSC differs from the experimental test case in chapter 2 which was made available later in the project.

The acoustic scattering calculated using the FSC was shown to be louder in plane and upstream of the rotor along the centerline (figure 3.3). The region upstream of the rotor between the centerline and the plane of the rotor was significantly quieter than the incident acoustic field. The baseline duct, modeled after a NACA 0024 airfoil, was then made thicker to a NACA 0048 airfoil (figure 3.5). The acoustic field became much quieter in plane but significantly louder out of plane. The baseline duct was then stretched to 4 times its original length (figure 3.6). The longer duct shows very little change directly in plane of the rotor while out plane is very different. The 4m duct

directs more noise at approximately a 45 degree angle upstream and downstream of the rotor. The results of the FSC code seem to be somewhat questionable at times, so their primary use was to compare general trends with the CFD/FW-H approach. The FSC results are not trusted and the method and geometry were abandoned once the experimental test case became available.

The second approach to calculating the scattered sound field was predicting the scattered field directly using PSU-WOPWOP and the CFD data on the duct rather than using equivalent sources. The geometry of the experimental test case was different from that used in the FSC results. The loading noise was also included in these acoustic calculations.

The OASPL for the rotor alone, duct alone, rotor and duct together (total), as well as the open rotor (CFD without a duct) was calculated using PSU-WOPWOP and compared. An important comparison was between the acoustic field of the rotor alone and the total acoustic field to compare to the trends shown in the FSC results (figure 3.10). Much like the FSC results, upstream of the rotor (90 to 180 degrees) is slightly louder due to scattering where at an angle downstream (~10 to 90 degrees), it is much quieter. The total field is also louder along the centerline downstream of the rotor (0 to ~10 degrees). Two features of the FSC results that are not seen is the increase in noise in the rotor plane, and the decrease at an angle upstream. The trend of the FSC compared fairly well to the trend of the acoustic fields obtained from the CFD data. The experimental team measured higher noise in each direction; however, the smallest increase was measured downstream out of plane which indicates that this location is being shielded the most by the duct.

The SPL at different harmonics was also analyzed. It was expected that the duct would not impact the incident field much at lower harmonics due to the long wavelength of the sound at that frequency. What was determined was the duct had an impact on the directivity of the sound field at lower harmonics but not the magnitude. At higher harmonics, the duct dominated both the directivity and magnitude of the sound field. This showed good agreement with the experimental data which also observed higher

noise from the ducted rotor than the open rotor when the wavelength became shorter than the length of the duct.

BIBLIOGRAPHY

- [1] Leishman, J. Gordon “Principles of Helicopter Aerodynamics” Cambridge University Press, NY, 2000. Editors Shyy, Wei and Rycroft, Michael. Pp.60-65, 320-324
- [2] Vuillet, A. ; Morelli, F., “New aerodynamic design of the fenestron for improved performance,” Rotorcraft design for operations, Flight Mechanics Panel Symposium held in Amsterdam, Netherlands, October 1986.
- [3] Breul and Kjaer, Environmental Noise Handbook, Denmark, 2000.
- [4] Dunn, M.H., and Tinetti, A.F., “Aeroacoustics Scattering Via Equivalent Source Method,” AIAA 2004-2937, May 2004
- [5] Brentner, K. S. and Farassat, F., “Modeling aerodynamically generated sound of helicopter rotors,” Progress in Aerospace Sciences, Vol. 39, 2003, pp. 83C120.
- [6] Ahn, Jon., and Lee, KyungTae. “Performance Prediction and Design of a Ducted Fan System” AIAA Paper 2004-4196, Jul. 2004
- [7] Tinetti, A.F., and Dunn, M.H., “Aeroacoustics Noise Predictions Using the Fast Scattering Code,” AIAA 2005-3061, May 2005.
- [8] Vuillet, A. and Morelli, F. “New Aerodynamic Design of the Fenestron for Improved Performance.” Rotorcraft Design for Operations, October 1986.
- [9] Pierce, Allen D. “Acoustics, An Introduction to Its Physical Principles and Applications.” Acoustical Society of America, New York, 1989
- [10] Regional Airline Association, “Aircraft Engines” Washington D.C. Regional Airline Association, 2009

- [11] JE, F. W. and DL., H., "Sound generated by turbulence and surfaces in arbitrary motion," *Philos Trans R Soc A*, Vol. 264, 1969, pp. 321C42.
- [12] M.H.Dunn, J. and F.Farassat, "The prediction of ducted fan engine noise via a boundary integral equation method," AIAA 96-1770, 2nd AIAA/CEAS aeroacoustic conference, May 6-8, 1996.
- [13] Tinetti, Ana F., Dunn, M.H, and Pope, D. Stuart, "Fast Scattering Code (FSC) User's Manual Version 2.0" NCI Information Systems Inc., March 10, 2006
- [14] C.A.Brebbia and J.Dominguez, "Boundary Element, An Introductory Course", McGraw-Hill Book Company, New York, 1990.
- [15] Ansys inc. "Fluent Documentation 6.2" Fluent Inc. 2005
- [16] Ansys inc. "Fluent Documentation 6.3" Fluent Inc. 2006
- [17] Kruger W. "On wind Tunnel Test and Computation Concerning the Problem of Shrouded Rotors" NACA Memorandum No. 1202 Feb 1949
- [18] Leighton, Myers, Hook, Ryan F., McLaughlin, Dennis K., "Experiments of Ducted Lift Fans in Hover and Edgewise Flight." AHS 66th Annual Forum, Phoenix, AZ, May 11-13 2010. American Helicopter Society International Inc. 2010
- [19] Leighton, Myers, Rhee, Wook, McLaughlin, Dennis K., "Aeroacoustics of Ducted Lift Rotors" AIAA 2009-3333 15th AIAA/CEAS Aeroacoustic Conference May 11th-13th 2009. American Institute for Aeronautics and Astronautics 2009.

- [20] Alpman, Emre, Long, Lyle, and Kothman, Bruce. "Toward a Better Understanding of Ducted Rotor Antitorque and Directional Control in Forward Flight" A.H.S 59th annual forum Phoenix Arizona, May 2003.
- [21] H. H Hubbard, D. L. L. and Runyan, H. L., "A review of rotating blade noise technology," Journal of Sound and Vibration, Vol. Volume 19, Issue 3, Dec,1971, pp. 227–241.
- [22] Margetts, E. J., "A demonstration that an axial fan in a ducted inlet ducted outlet configuration generates predominantly dipole noise," Journal of Sound Vibration, Vol. 117, 1987,sep, pp. 399–406.
- [23] M.Roger, Ecole Centrale de Lyon, F., "Applied aeroacoustic methods for the acoustic design of a shrouded tail rotor," 16th AIAA Aeroacoustics Conference, June 12-15, 1995, pp. 963–971.
- [24] LANSING, D. L., "Exact solution for radiation of sound from a semi-infinite circular duct with application to fan and compressor noise. Analytic methods in aircraft aerodynamics." Symposium held at Ames Research Center, Moffett Field, California, Vol. SP-228, October, 1969, pp. 323–334.
- [25] Homicz, G. F. and Lordi, J. A., "A note on the radiative directivity patterns of duct acoustic modes," Journal of Sound Vibration, Vol. 41, Aug 1975, pp. 283–290.
- [26] Stephane Lidoine, Herve Batard, S. T. A. D. and Roger, M., "Acoustic Radiation Modeling Of Aeroengine Intake Comparison Between Analytical And Numerical Methods," 7th AIAA/CEAS Aeroacoustics Conference and Exhibit, Vol. 1, May 28-30, 2001, pp. 2001–2140.

[27] ABOM, M. and Boden, H., "A note on the aero acoustic source character of in-duct axis fans," *Journal of sound and vibration*, Vol. 186(4), 1995, pp. 589–598.

[28] Peter Moore, H. S. and Boersma, B. J., "Simulation and measurement of flow generated noise." *Journal of Computational Physics*, Vol. 224, Issue 1, 20 May 2007, pp. 449–463.

[29] A.Powell, "Theory of vortex sound," *Journal of the Acoustical Society of America*, Vol. 36, 1964, pp. 177–195.

29

[30] P.E.Doak, "Acoustic radiation from a turbulent fluid containing foreign bodies," *Proceedings of the Royal Society of London*, Vol. 254, 1960, pp. 129–145.

[31] Crighton, D. G. and Leppington, F. G., "On the scattering of aerodynamic noise," *Journal of Fluid Mechanics*, Vol. 46, 1971, pp. 577–597.

[32] M.S.Howe, *Sound generation in a fluid with rigid boundaries, Acoustics of Fluid-Structures Interactions*, Cambridge University Press, 1998.

[33] X. Gloerfelt, F. Prot, C. B. and Juv, D., "Flow-induced cylinder noise formulated as a diffraction problem for low Mach numbers," *Journal of Sound Vibration*, Vol. 287, 2005, pp. 129C151.

[34] Farassat F, M. M., "Extension of Kirchhoffs formula to radiation from moving surfaces," *Journal of Sound and Vibration*, Vol. 123, 1988, pp. 451–461.

Appendix A

Aerodynamic Setup in Fluent

The following (table A1) is the information provided by the experimental team on the Duct/Rotor Configuration used for experimentation.

Hub Diameter	22.2	mm	Rad.	11.1	mm			
Msr. Radius	118.1	mm						
solidity	0.1							
Airfoil	NACA 4412							
Averaged Values								
Radius, R	Thickness	H_LE	H_TE	Pitch	Chord, c	r/R	t/c	c/R
mm	mm	mm	mm	Degree	mm	-	-	-
15.1	6.3	12.5	5.5	26.84721	15.5	0.127858	0.406452	0.120999
23.1	4.875	13.25	4.75	31.70207	16.175	0.195597	0.301391	0.126269
31.1	4.625	13.5	4.5	30.99889	17.475	0.263336	0.264664	0.136417
39.1	4.35	13.25	4.75	27.59478	18.35	0.331075	0.237057	0.143247
47.1	4.1	13	5.5	23.61157	18.725	0.398815	0.218959	0.146175
55.1	3.875	12	6	18.48407	18.925	0.466554	0.204756	0.147736
63.1	3.65	11.5	6.5	15.23699	19.025	0.534293	0.191853	0.148517
71.1	3.35			13.07014	19.025	0.602032	0.176084	0.148517
79.1	3.1			11.23613	18.725	0.669771	0.165554	0.146175
87.1	2.9			9.975279	18.3	0.737511	0.15847	0.142857
95.1	2.6			9.150015	17.45	0.80525	0.148997	0.136222
103.1	2.375			8.622759	16.45	0.872989	0.144377	0.128415
111.1	2.2			8.255932	15.25	0.940728	0.144262	0.119048
116.1	2.025			8.047003	14.225	0.983065	0.142355	0.111046

Table A.1: Rotor Parameters

A Solidworks diagram of the duct was also provided (figure A.1).

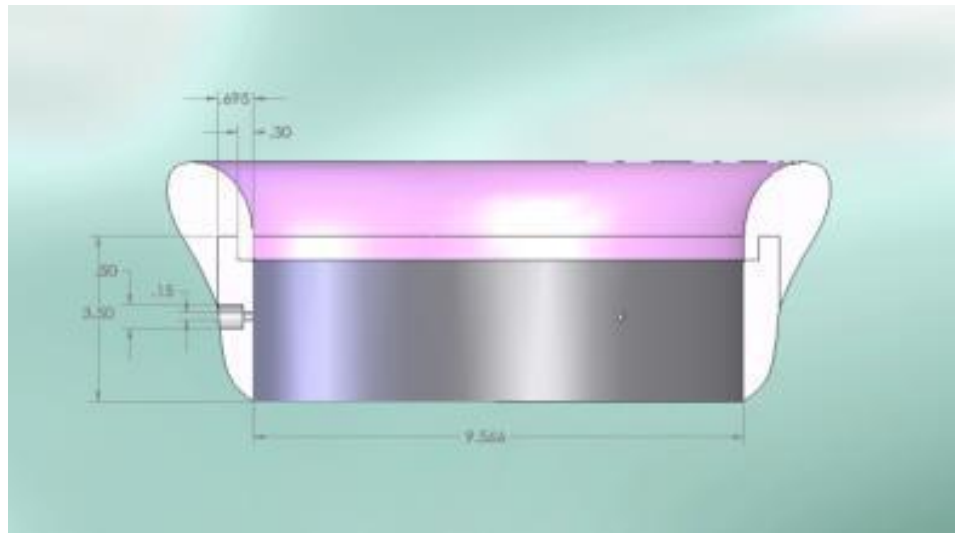


Figure A1: Duct Geometry [18]

The CFD simulation was setup following along with Fluent Documentation 6.3 tutorial 11 [16] “Using sliding meshes.” The tutorial itself shows how to set up one stage of turbomachine. The process of creating an interface between a rotor and a stator section was duplicated to create the needed interface between where to moving rotor and the stationary duct.

The domain was divided into 3 sections, freestream, duct area, and blade area (figure A.2).

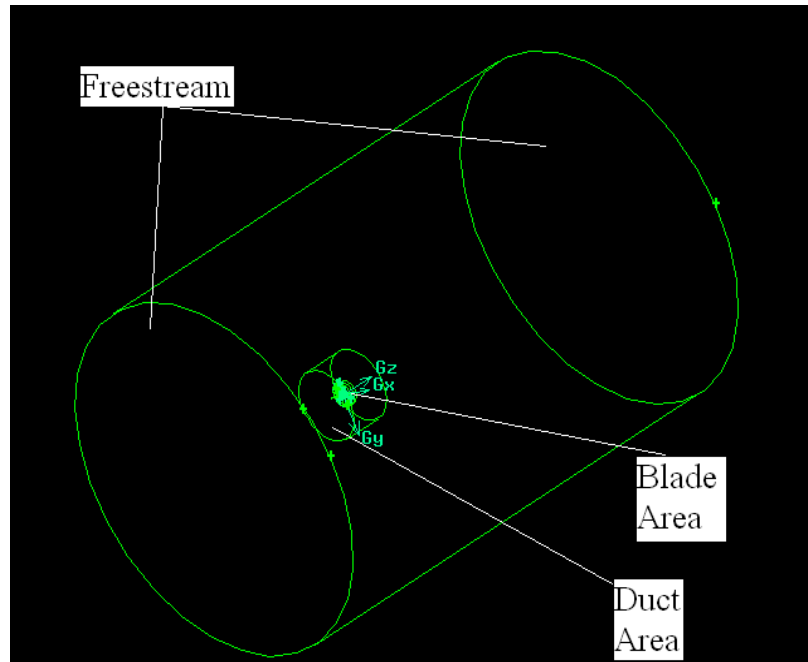


Figure A.2: Wireframe of Domain

The blade area itself is only a small disc (figure A.3)

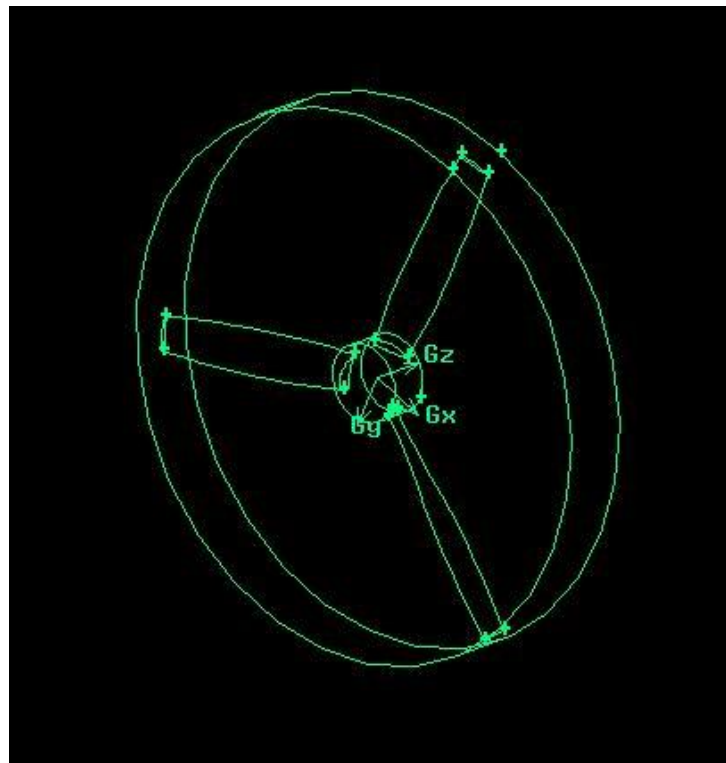


Figure A.3: Inner Region of Domain

The subdivision between the free stream and the duct area was for the purpose of meshing. All relevant CFD parameters were identical for the duct area and freestream but the meshing was different. The freestream is fairly coarse while the duct area is meshed slightly finer and the blade itself is meshed very fine. This was important for capturing the near field flow features while not consuming too much memory. A tetrahedral unstructured mesh was used. The fluid in the freestream and duct area is stationary while the blade area is in a rotating reference frame. The freestream area extends 10 rotor diameters upstream and radially outward from the rotor and 20 rotor diameters downstream. The duct flow extends 4 rotor radii in each direction.

In order to get the motion of the blade area right, the small domain in figure A.3 was disconnected from the rest of the domain then edges were interfaced with the coinciding edges of the outer domain. A simple example of how to create a disconnected domain inside a larger one is shown with two cylinders.

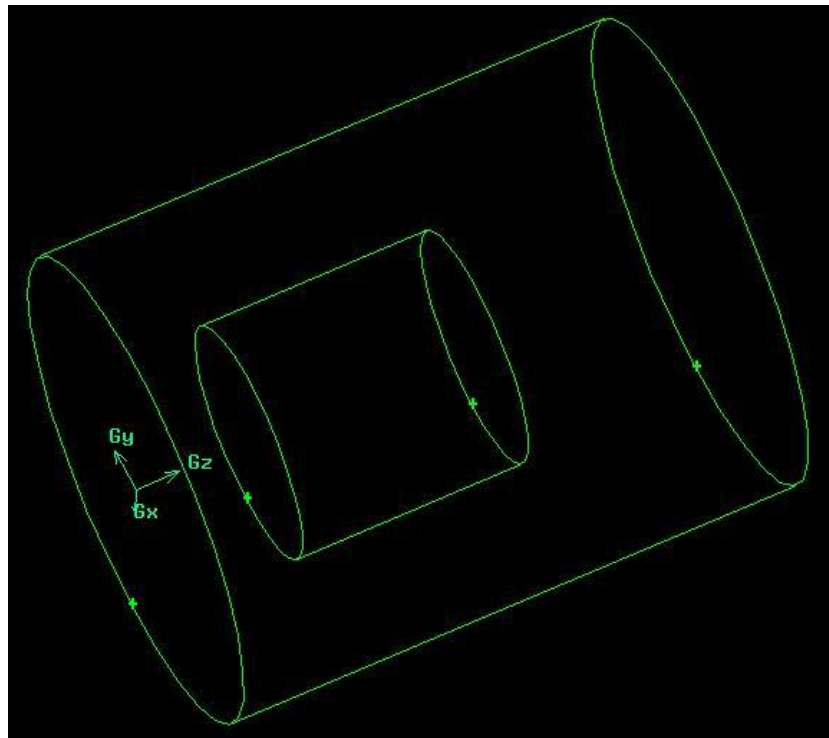


Figure A.4: Outer Region and Duct Area

The Gambit geometry option (figure A.5) to split the outer volume with the inner volume's faces was used.

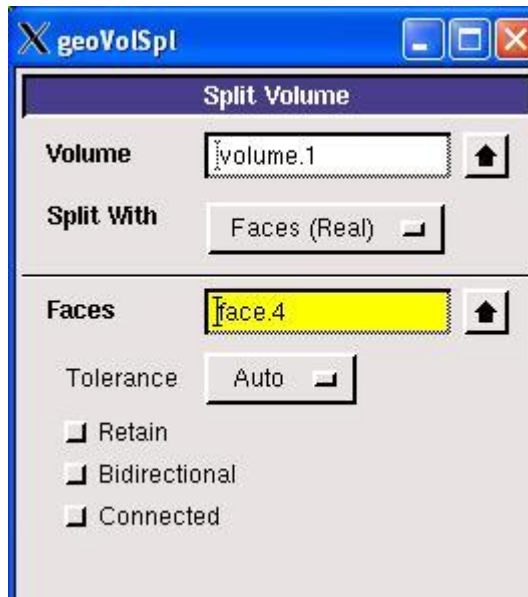


Figure A.5: Split Volume Window

It is important to ensure that the “connected option is unchecked.” This will create two domains disconnected but with coincidental faces.

With these zones in place, the domain could easily be meshed using different densities. Figure A.6 contains a slice of the entire domain mesh. To make the difference in the mesh density between the duct area and rotor area more clear, figure A.7 is a zoomed in look at the area near the rotor and duct.

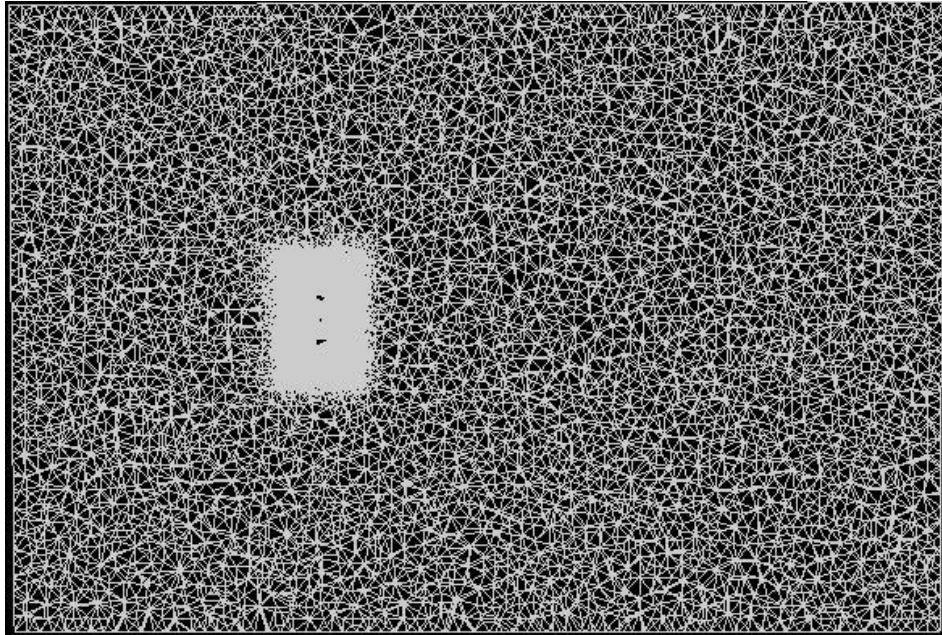


Figure A6: Domain Mesh

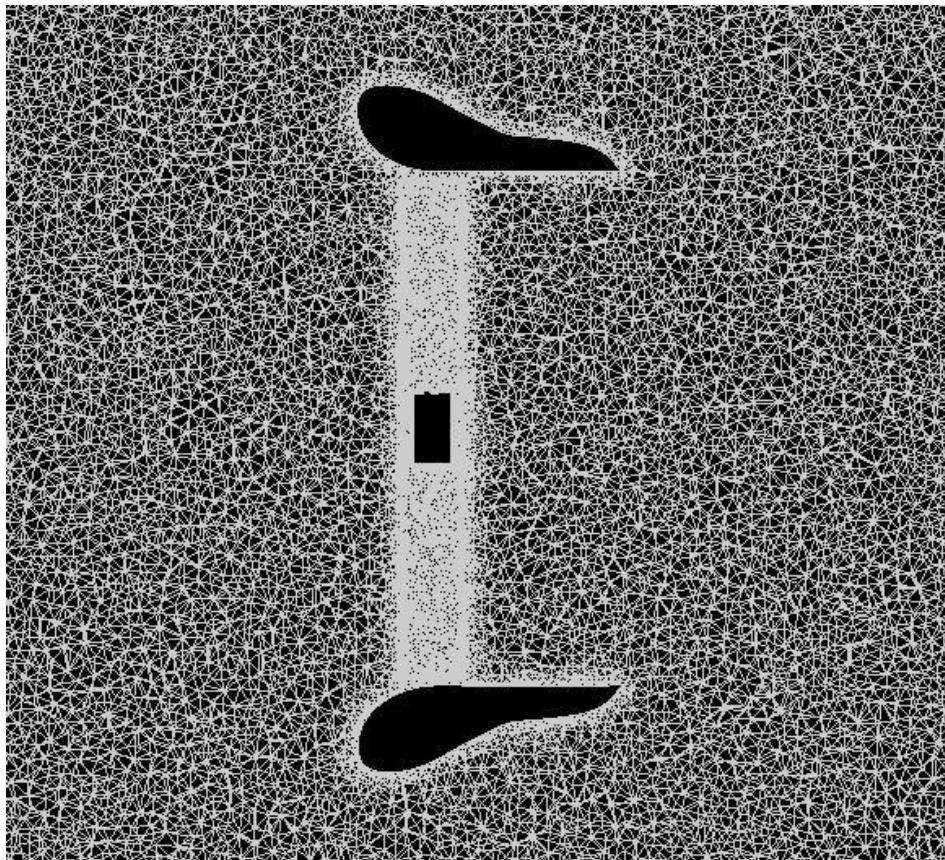


Figure A.7: Duct Area Mesh

A breakdown of the mesh for each zone is in table A2.

Ducted			Open		
Volumes	Nodes	Cells	Volumes	Nodes	Cells
Outer	185232	1225350	Outer	238074	1224664
Duct Area	1102538	6160439	Inner Area	913033	5313371
Rotor Area	536452	2593435	Rotor Area	536452	2593435
Surfaces	Nodes	Faces	Surfaces	Nodes	Faces
Rotor	77005	154006	Rotor	77005	154006
Duct	78830	131556	Interface	126840	250708
Interface	126840	250708			
Total Nodes			Total Nodes		
1824222			1634551		

Table A.2: Mesh Details

In order to create the grid of this size, the faces of each zone were meshed first then the volumes were meshed by using the Gambit default size function. The size function automatically stretches the mesh if the walls have differing mesh densities [7]. The outer domain and duct area, and blade area walls all had constant mesh density (figure A.8). The mesh spacing for each was;

Outer Domain = 0.1

Duct Area = 0.007

Rotor Area = 0.001

Hub Walls = 0.001

Note that Gambit does not store units but rather just the numbers themselves. The actual units tied to those numbers are declared when the grid is loaded into Fluent. The unit declaration is under Grid -> Scale Grid and set the option “grid defined in” correctly (Figure A.9). The rotor surface itself was more complicated to mesh since it was desired to have the tip of the rotor blades more finely mesh than the hub (Figure A.10).

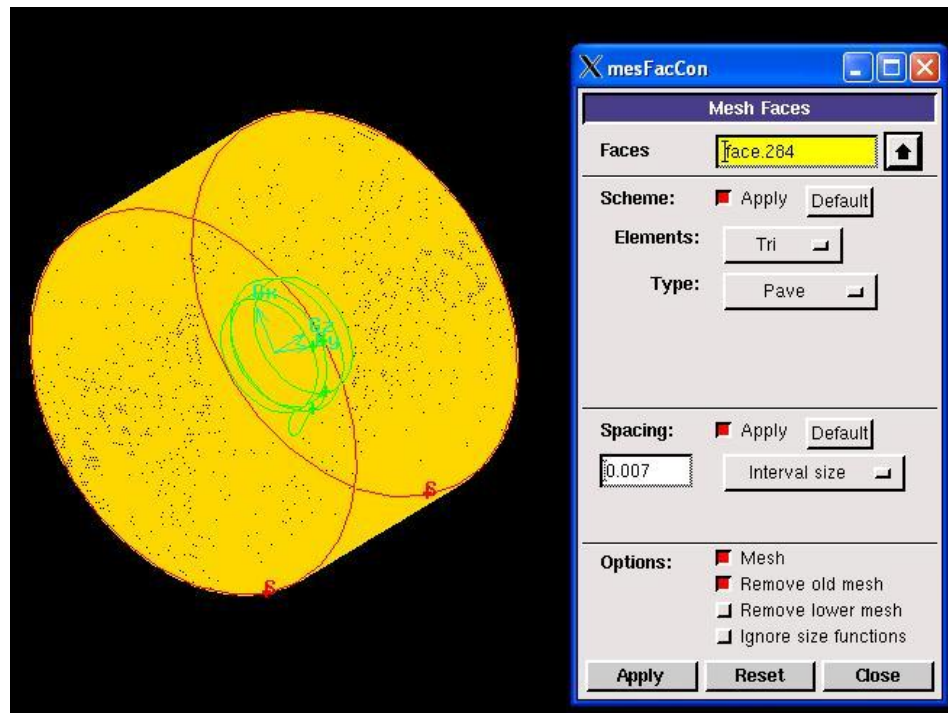


Figure A.8: Wall Meshing Options

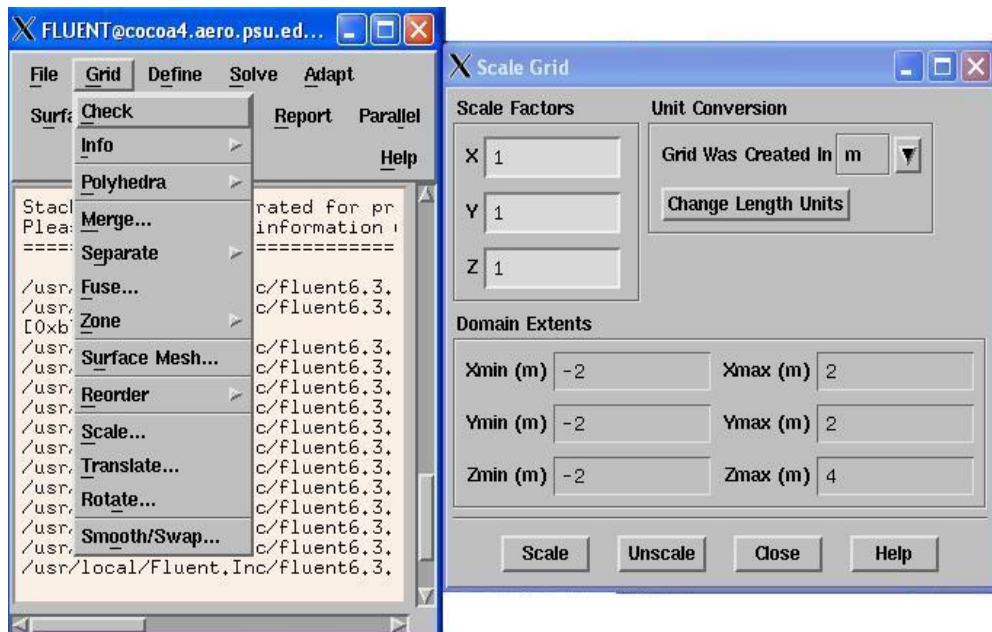


Figure A.9: Defining Grid Units.

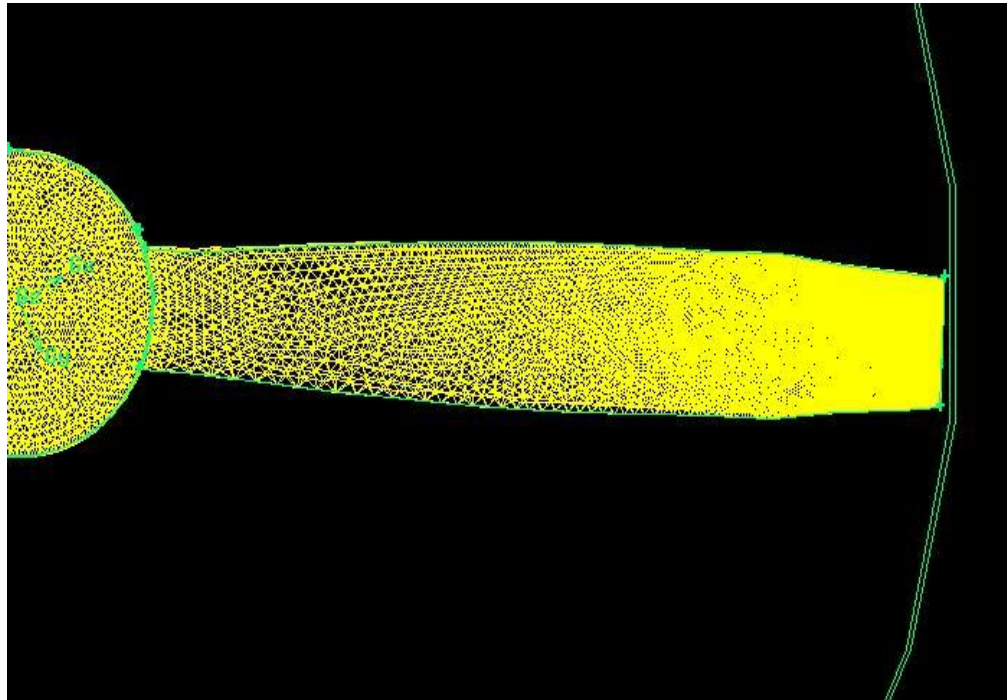


Figure A.10: Mesh Distribution Along Rotor Blade Span

To mesh the rotor blade, the edges were meshed first. The root of the rotor was meshed with 20 points around the coord (figure A.11). The leading edges (figure A.12) used a spacing of 0.0004 spacing and a ratio of 0.98. The ratio option in the meshing is what stretches the grid. The trailing edges (figure A.13) had a spacing 0.001 but was not stretched because of issues when meshing the volume. The tip (figure A.14) was meshed using 102 points around the coord with a ratio of 1.02. Note that some iterations had to be done in terms of spacing. The main problem encountered was the volume mesh containing very highly skewed cells if the stretching of the grid became too rapid.

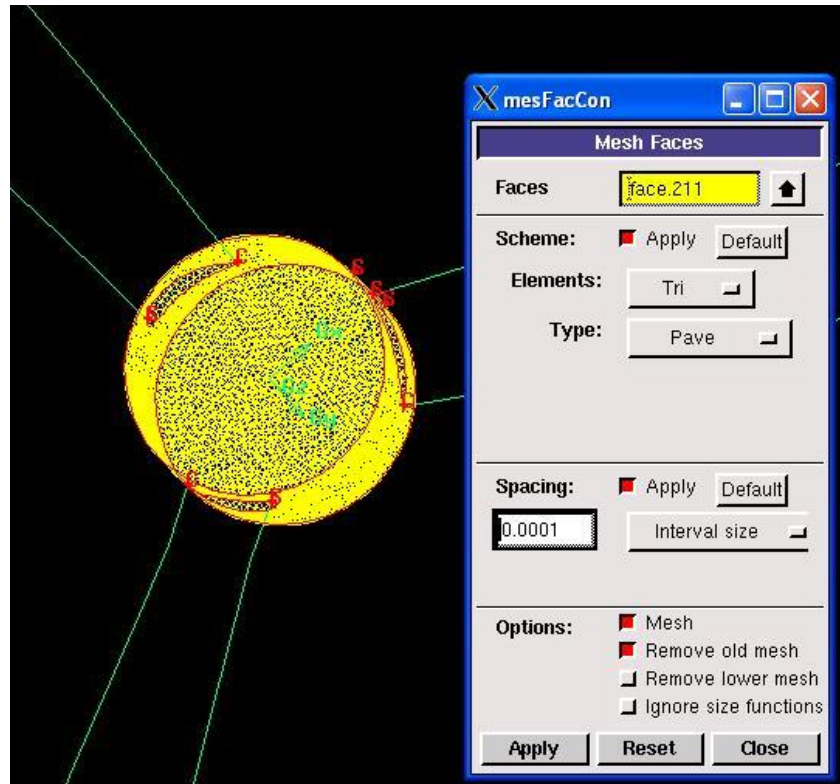


Figure A.11: Hub Mesh

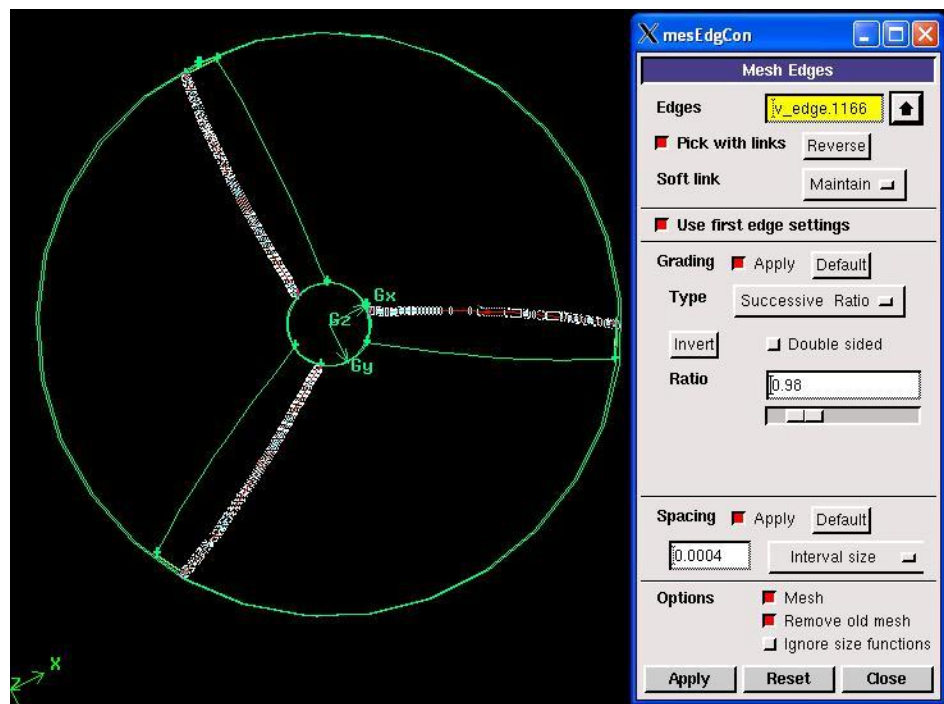


Figure A.12: Leading Edge Mesh

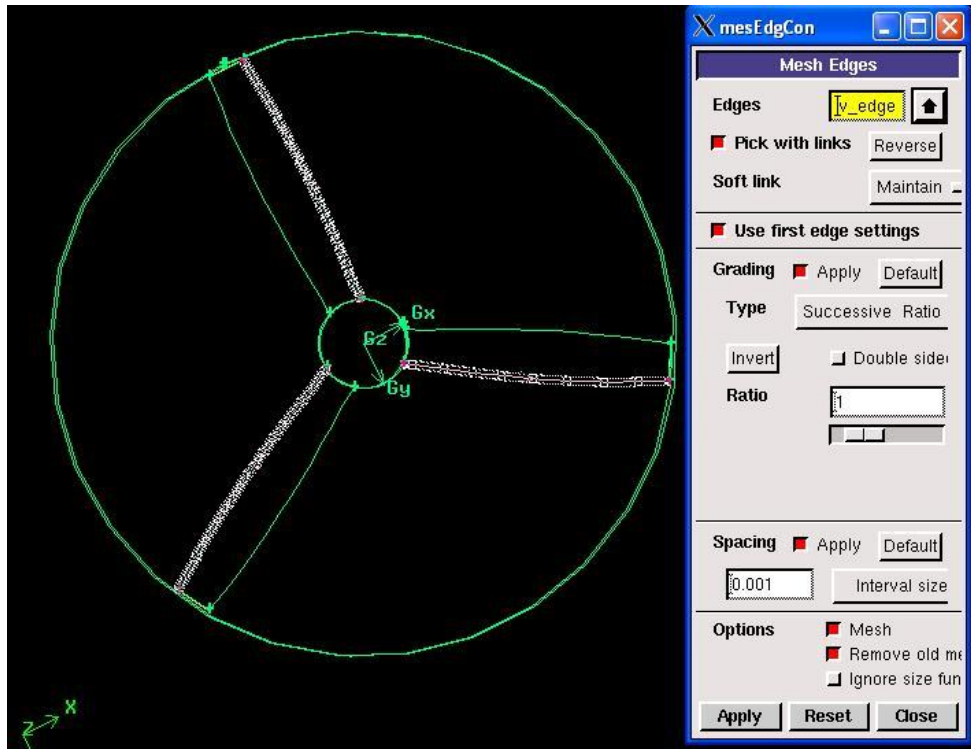


Figure A.13: Trailing Edge Mesh

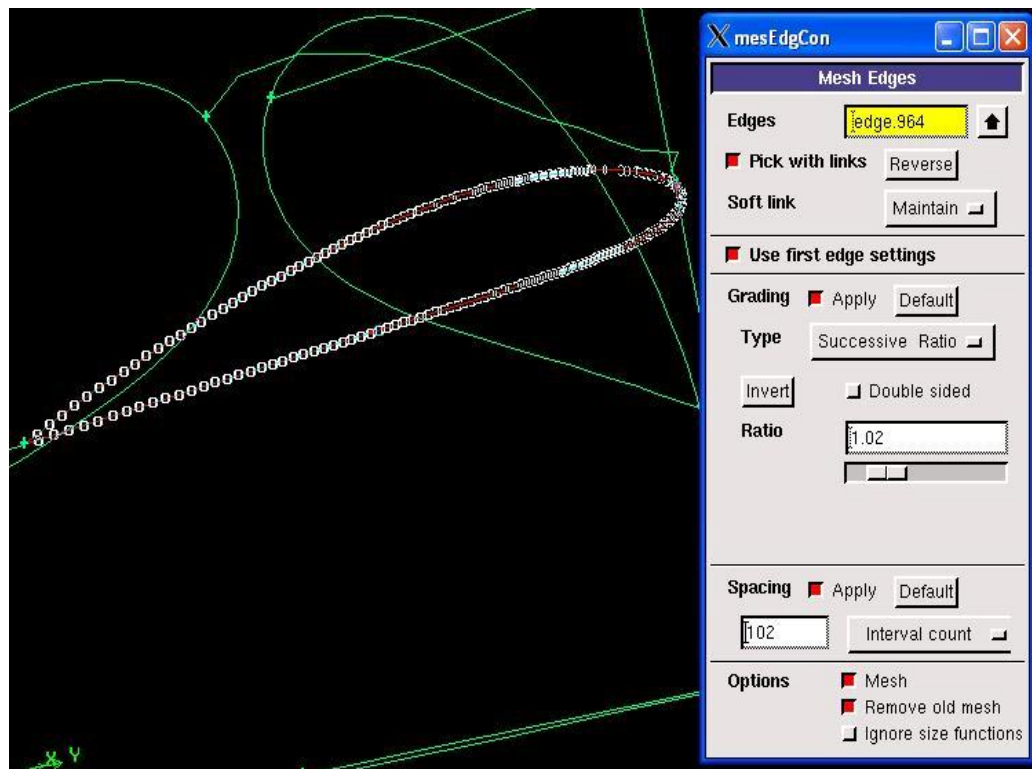


Figure A.14: Tip Mesh

Appendix B

Converter

This section is intended to provide the reader with insight for converting Fluent output to WOPWOP input.

FieldView-unstructured files were chosen as the output from Fluent because they are much smaller files than Fluent case and data files and are well documented. The files can be exported using the script commands;

```
/file/export/fieldview-unstruct
```

```
<output file name>
```

```
pressure
```

```
<any additional variables needed by the user (1 per line)>
```

```
no (this command is to tell Fluent that you don't want anymore variables)
```

Fluent outputs a two files, `outputfile.fvuns` and `outputfile.fvuns.fvreg`. Only `outputfile.fvuns` is needed for conversion. Note that all characters in the file are of length 80 and that all non-integer numbers are single precision. The opening headers of the file are as followed.

```
66051 (integer "magic number")
```

```
FIELDVIEW (character)
```

```
3 0 (two individual integer representing the version number)
```

```
Integer identifier
```

```
Integer identifier
```

```
Solution time
```

```
Field variable 2
```

```
Field variable 3
```

```
Field variable 4
```

```
Number of grids (Integer. If the domain is subdivided into more than one flow section, that is represented here)
```

Number of boundaries (Integer. This is the total number of surfaces defines such as ducts, rotors, inlets, outlets etc.)

The next section identifies what the zones are. Each zone also has 2 integer flags which describe the clockness. This section will look something like;

1 1

Duct

1 1

Inlet

1 1

Rotor

Etc.

It is very important to record the order of the surfaces as the grid and data for those surfaces are written in the same order. The next section reads what variables are in the file. Again, it is important to record the order because the data is output in the same order. The section itself is fairly simple;

Number of variables (integer)

Variable name 1 (character)

Variable name 2 (character)

Etc.

Number of surface variables (integer)

Surface variable name 1 (character)

Surface variable name 2 (character)

Etc.

This is followed by the information for each grid;

1001 (Integer, header for the grid)

Number of nodes (Integer, the number of nodes in the current grid)

X (The next part of the file is all the xvalues, then y values, then z values)

Y

Z

The next part of the file contains information about the grid connectivity. The information is grouped by surface so all the connectivity for one surface is written, then another surface is written. Each has 3 integer headers describing it.

1002 (integer that indicates that it is a surface)

Integer (this number is simply the surface number and will match zones. For example, if the rotor is written first then the inlet, a value of one corresponds to the rotor and 2 indicates the inlet.

Nfaces (the number of faces on this surface)

The next section is a face by face list of the nodes that make up each face. In the case of triangular faces, Fluent outputs 4 nodes per face with the 4th being 0 (in the case of triangular surface meshes). For this case, the next section will look like this,

1 2 3 0 2 3 4 0 3 4 5 0 etc.

Next comes the grid type;

1003 (integer that indicates the grid type will be read next)

NTet (number of tetrahedrons in the grid)

Nhex (number of hexahedrons in the grid)

Npris (number of prisims in the grid)

NPyr (number of Pyramids in the grid)

<need to refresh grid identifiers>

The grid variables are then written. The section starts with a header, then writes each variable individually for all points in the domain. The case the author used looked like this.

1004

Pressure

Xvelocities

Yvelocities

Zvelocities

Note that using the interface method in appendix A, Fluent will write out 2 grids (one for each domain). To read the second grid, the steps for each grid are repeated. The grid by grid structor will look like;

Fluent Headers

Grid 1 header

Grid 1 grid

Grid 1 connectivity

Grid 1 variables

Grid 2 header

Grid 2 grid

Grid 2 connectivity

Grid 2 variables

Once all the information about the grids have been read, the converter then extracts desired face to be converted, calculated the normal vector for each node, and writes it in PSU-WOPWOP format.

Perhaps the most difficult problem to solve was translating the connectivity of the grid into PSU-WWOPWOP. This is because certain points that are in the FieldView file will not be put into PSU-WOPWOP. For example, if the converter was trying to write a face into PSU-WOPWOP that contained node number 1,2, and 4 and suppose node 3 was not used by the face, PSU-WOPWOP would look for node 4 and not be able to find it because only 3 nodes have been written.

The solution to this problem was a two part process. First, a list of all the nodes used by the desired surface had to be obtained and second, the nodes had to be renumbered.

To solve the first problem, the connectivity information for the surface in question was condensed into one array. This was done by reading in the nodes used by each face on the surface in question into a one dimensional array. That array was then sorted to eliminate any repeated value. Sorting out the repeated values took a significant amount of run time. From this list of nodes, the grid to be read into PSU-WOPWOP was formed.

The variable used for reading in all the X coordinates from Fluent was “x(i)”. The following loop was used to form an array for all of the x coordinated for wopwop.

```
Do i=1, size(grid)
Xcoord = x(grid(i))
End do
```

Where “grid” is the list of nodes.

The second part of the problem, which was to renumber the connectivity proved a bit trickier. In the following explanation, node_id refers to the Fluent connectivity and wwnode_id refers to the connectivity to be read into PSU-WOPWOP. This process was done on a face by face basis.

To start, the nodes used by the first face on the surface was read. For example, it was nodes, 1, 2, 5. Each node would be renumbered individually. The code goes something like;

```
Node_id = 1
i=1
Do while (node_id .ne. grid(i))
    i=i+1
end do
wwnode_id(1) = i
```

This tracks which index in “grid” is equal to the node_id. For example, Fluent if writes out 5 nodes (nodes 1, 2, 3, 4, and 5). Suppose nodes 3 and 4 are on a surface that will not be used by PSU- WOPWOP so only nodes 1, 2, and 5 are being used. If node 5 is not renumbered, then PSU-WOPWOP will be looking for node 5 and not be able to find it because it is looking for node 5 when only 3 nodes are input. The loop above would renumber node 5 to node 3.

At this point in the code, the following arrays are needed for PSU-WOPWOP.

Grid: The points used by the surface in question

Pressure: The pressure output from Fluent.

X, Y, Z data: The grid information

Normal Vectors: Calculated by using the crossing two vectors on each face of the surface.

Connectivity: The connectivity renumbered for PSU-WOPWOP

For the grid patch file, the format of the output will look like this

Header (refer to PSU-WOPWOP manual)

Connectivity

All x locations

All y locations

All z locations

All x components of normal vectors

All y components of normal vectors

All z components of normal vectors

The loading patch file format is much simpler and looks like this

Header

Pressure data